Volume 18, Number 1, 2024

Technical University of Cluj-Napoca
North University Centre of Baia Mare
Faculty of Engineering
Electrical, Electronic and Computer Engineering Department

Volume 18, Number 1, 2024

Carpathian Journal of Electrical Engineering

Carpathian Journal of Electrical Engineering

UTPRESS PUBLISHER

ISSN 1843 - 7583

TECHNICAL UNIVERSITY
OF CLUJ-NAPOCA

NORTH UNIVERSITY CENTRE OF BAIA MARE
FACULTY of ENGINEERING

ELECTRICAL, ELECTRONIC AND
COMPUTER ENGINEERING DEPARTMENT

Carpathian Journal of Electrical Engineering

Volume 18, Number 1, 2024

ISSN 1843 – 7583
http://cee.cunbm.utcluj.ro/cjee/

CONTENTS

Received: June 2024, Accepted: September 2024, Published: December 2024
Digital Object Identifier: *https://doi.org/10.34302/CJEE/TKYD3692*

ENHANCED MULTI-OBJECTIVE GREY WOLF OPTIMIZATION USING ADAPTIVE DIVERSITY TUNING AND LEVY FLIGHTS

Peter **ASIGRI**, Emmanuel Asuming **FRIMPONG,** Emmanuel Kwaku **ANTO**, Daniel **KWEGYIR,** Francis Boafo **EFFAH**
Department of Electrical and Electronic Engineering, Kwame Nkrumah University of Science and Technology, Kumasi, Ghana
pasigri@knust.edu.gh, eafrimpong.soe@knust.edu.gh, kwakuantoh@yahoo.com, daniel.kwegyir@knust.edu.gh, fbeffah.coe@knust.edu.gh

Keywords: Multi-objective Optimization, Grey Wolf Optimizer, Adaptive Population Diversity, Levy Flight

Abstract: *This study proposes an enhanced Multi-Objective Grey Wolf Optimizer (MOGWO) using adaptive population diversity tuning and levy flight theories (EMOGWO-ADTLF). It addresses the issues of parameter tunning by balancing exploration and exploitation. Using MATLAB and Python library Pymoo, the study implemented and evaluated the performance of EMOGWO-ADTLF using multi-objective test problems. The results were compared to high-performing algorithms like MOGWO, Non-Dominated Sorting Grey Wolf Optimizer (NSGWO), Dynamic Chaos MOGWO (DCMOGWO), Multi-Objective Mayfly Algorithm (MMA), Multi-Objective Antlion Algorithm (MOALO) and Multi-Objective Dragonfly Algorithm (MODA). In this work, inverted generational distance (IGD) and hypervolume (HV) were the metrics used to measure the performance of algorithms. The metrics measure the diversity, coverage, and spread of solutions. The results obtained showed the potency of EMOGWO-ADTLF in approximating the Pareto fronts. It ranks first in overall average scores in IGD and HV, with total rank scores of 17 and 18, respectively.*

1. INTRODUCTION

Multi-objective optimization has become important in solving problems that involve conflicting objectives in the era of computational intelligence [1,2]. In multi-objective optimization, the goal is always to find a set of solutions, each with a different trademark among the objectives. This is unlike single-objective optimization, which gives a single solution [1]. Multi-objective optimizers have been applied in real-world applications. They are found in engineering designs [2,3], environmental management, and financial planning. For example, one can optimize between service quality and energy use in cloud manufacturing [2]. In power systems engineering, there can be a trade-off between technical and economic effectiveness [3–7]. Also in industrial engineering, multi-objective optimizers help to balance conflicting objectives like cost efficiency and process quality [8].

The advantage of multi-objective optimization is its ability to give diverse options for decision-making. This diversity is crucial because it helps us make better decisions, especially when focusing on just one solution could lead to poor and suboptimal results [1,9]. Multi-objective optimizers are of different kinds. Nature-inspired type is widely used due to its ability to navigate complex solutions effectively. One of these algorithms is MOGWO. MOGWO is an optimizer that solves complex multi-objective problems and is easy to implement [1]. This algorithm has successfully been used in many engineering studies including multi-objective power flow studies [10], multi-robot exploration [11], wind speed forecasting [12] and optimal sizing of microgrids [13]. It has also been used to solve problems such as energy planning for smart homes [14] and reactive power dispatch [15] and transportation location routing [16]. Despite the numerous applications of MOGWO, it still has some deficiencies, just like other metaheuristic algorithms.

Common deficiencies of the MOGWO algorithm include limited performance and scalability, especially when the problem has many objectives [1,17]. The challenge of parameter tuning in Grey Wolf Optimizer (GWO) algorithms also exists [18]. The MOGWO algorithm depends on two parameters to balance between exploration and exploitation in solving multi-objective problems, and the choice of these parameters often affects the quality of the solution [19]. Another common issue with MOGWO is local optima entrapment, especially in cases where there is a need to find global optimum from many local optima [2,20–22].

Some improvements have been made to enhance the performance of the MOGWO algorithm. Yang et al. [23] proposed an improved MOGWO using the ranked-order-value rule for dynamic archive maintenance and solution representation. This algorithm performed better in coverage, spread, and convergence than MOGWO and Multi-Objective Particle Swarm Optimizer (MOPSO). Using a backward learning strategy, Yang et al [2] improved MOGWO to address diversity and local optimum issues. Tian et al. [20] improved MOGWO using multiple techniques. The strategy involved clustering non-dominated solutions, cluster density head wolves' selection, and mutation operator for improved exploration. The results showed an enhanced distribution and diversity compared to the MOGWO algorithm. Another work by Gu [21] introduced an improved MOGWO (DCMOGWO) using dynamic chaos search techniques to solve local optima issues and search precision. DMOGWO outperformed

MOGWO and other nature-inspired algorithms in benchmarked problems. Tlili et al. [17] developed an improved MOGWO (IMOGWO) to help deal with many objectives. In a comparative study with MOGWO and other optimizers, IMOGWO provided better convergence and exploration. Al-Tashi et al. [24] proposed a binary variant of MOGWO (BMOGWO-S) to enhance feature selection in classification. BMOGW-S showed effective classification and feature reduction error rates compared with multi-objective optimizers using the UCI dataset. Other variants of MOGWO that offer enhanced performance include NSGWO [25], Levy-based MOGWO (LMOGWO) [26], improved MOGWO based on individual diversity (IMOGWO) [27], Advanced MOGWO (MOAGWO) [28] and Hybrid MOGWO (HMOGWO) [29].

The aforementioned variants of MOGWO have advanced its performance. However, fundamental defects like avoiding local optima, enhanced parameter tuning, maintaining diversity, and improving convergence still need attention. Though some variants introduced techniques and mechanisms for enhanced parameter tuning, the issue of tuning parameters to balance between exploration and exploitation has not been comprehensively tackled. There is still the need for intuitive and efficient approaches to parameter tuning.

This study proposes an Enhanced MOGWO using adaptive diversity tuning and levy flight (EMOGWO ADTLF) theories to enhance parameter tuning. This enhancement adjusts the control parameters dynamically to balance between exploration and exploitation. This ensures better exploration by reaching the global optimal solutions and reducing local optima entrapment. It also provides better convergence of the obtained Pareto solution and robustness in handling complex and different optimization tasks.

The rest of the paper is structured into sections: Section 2 explains the MOGWO. Section 3 presents the proposed EMOGWO-ADTLF using the population diversity tuning technique and levy flight theories. Section 4 highlights the benchmark functions used for testing and test parameters. Section 5 presents the results of implementing the enhanced MOGWO and its comparison with others. Conclusions drawn are provided in section 6.

2. MULTI-OBJECTIVE GREY WOLF OPTIMIZER

2.1. MOGWO Algorithm

MOGWO is a nature-inspired algorithm based on the hunting behavior of grey wolves [1]. This algorithm advances the GWO, which can only solve a single objective problem [30].

The GWO employs simulated social leadership and encircling behavior to discover optimal solutions. With regard to social leadership, the decreasing order of dominance is designated as alpha (α), beta (β), delta (δ) and omega (ω) wolves. This hierarchy influences the decision-making process in the search space [1,30].

The encircling mechanism observed in grey wolves during hunting is modeled using (1) and (2).

$$\vec{D} = \left|\vec{C} \, . \vec{X}_p(t) - \vec{X}(t)\right| \tag{1}$$

$$\vec{X}(t + 1) = \vec{X}_p(t) - \vec{A} \cdot \vec{D} \tag{2}$$

$\vec{X}_p$ is the location vector of the prey, while $\vec{X}$ is the position vector of a wolf, and t indicates the current iteration. The vectors $\vec{A}$ and $\vec{C}$ represent coefficients.
The calculation of vectors $\vec{A}$ and $\vec{C}$ are given in (3) and (4).

$$\vec{A} = 2\,\vec{a} \cdot \vec{r}_1 - \vec{a} \tag{3}$$

$$\vec{C} = 2 \cdot \vec{r}_2 \tag{4}$$

Here, $\vec{a}$ (convergence factor) linearly decreases from 2 to 0 during the iterations. $\vec{r}_1$ and $\vec{r}_2$ are random vectors within the [0, 1] range.

The GWO preserves the top three solutions obtained thus far and compels other search agents, including the ω, to adjust their locations relative to these solutions. Equations (5) to (11) are iteratively applied to each search agent throughout the search process, simulating the hunting behavior and identifying promising areas within the search region [30].

$$\vec{D}_\alpha = \left|\vec{C}_1 \cdot \vec{X}_\alpha - \vec{X}\right| \tag{5}$$

$$\vec{D}_\beta = \left|\vec{C}_2 \cdot \vec{X}_\beta - \vec{X}\right| \tag{6}$$

$$\vec{D}_\delta = \left|\vec{C}_3 \cdot \vec{X}_\delta - \vec{X}\right| \tag{7}$$

$$\vec{X}_1 = \left|\vec{X}_\alpha - \vec{A}_1 \cdot (\vec{D}_\alpha)\right| \tag{8}$$

$$\vec{X}_2 = \left|\vec{X}_\beta - \vec{A}_2 \cdot (\vec{D}_\beta)\right| \tag{9}$$

$$\vec{X}_3 = \left|\vec{X}_\delta - \vec{A}_3 \cdot (\vec{D}_\delta)\right| \tag{10}$$

$$\vec{X}(t + 1) = \frac{\vec{X}_1 + \vec{X}_2 + \vec{X}_3}{3} \tag{11}$$

The GWO optimization process begins by randomly generating solutions as the initial population. Through the optimization, the three best solutions obtained thus far are saved and designated as α, β, and δ) solutions. The position updating equations (5) to (11) are activated for each wolf (search agents excluding alpha, beta, and delta). Simultaneously, parameters $\vec{A}$ and $\vec{a}$ experience a linear decrease over the iteration. Consequently, search agents move away from the prey when $\vec{A}$>1 and move close to the prey when $\vec{A}$<1. Ultimately, the position and score of the α solution are recorded as the best solutions achieved during optimization once the iterations have ended [30].

To turn the GWO into a multi-objective optimizer (MOGWO), two features are added. The first component is the archive, and the second is the leader selection strategy. The archive stores the non-dominated solutions. The leader selection strategy helps obtain the α, β, and δ solutions and make them leaders. In the archive, an archive controller manages, saves, and retrieves Pareto solutions during iterations. A specific rule governs the entry of new solutions into the archive. If an archive member dominates any new solution, entry is not allowed. New solutions can enter the archive if it dominates one or more members. In this case, the dominated solutions are deleted. New solutions are also allowed entry if there is no dominance between them and stored archive solutions. The MOGWO algorithm has a grid mechanism that helps to rearrange the objective space when an archive gets full. The mechanism deletes solutions from the most crowded areas and stores the new solutions in the least overcrowded zones. This ensures better distribution of solutions [1].

GWO algorithm uses the parameter $'\boldsymbol{a}'$ to decide the search radius. This value controls the exploration-exploitation trade-off. The parameter ranges from 0 to 2, decreasing linearly during the iteration. This decrease assists the algorithm by reducing parameter tuning. However, some defects may affect the algorithm performance depending on the problem [19]. The challenges include:

- Excessive early exploration: If the initial value of $'\boldsymbol{a}'$ is too high, the algorithm will likely over-explore without looking for optimal regions. This may delay convergence.
- Premature Exploitation: If $'\boldsymbol{a}'$ decreases rapidly, it could cause early exploitation. The algorithm gets trapped in local optima and misses better solutions.
- Fine-tuning difficulty: Determining the optimal starting and ending value for linear tuning techniques may require adjustment and experimentation depending on the type of problem.

2.2. Proposed EMOGWO-ADTLF Using Population Diversity Tuning Technique and Levy Flight

In this work, population diversity is employed to improve the performance of MOGWO. Population diversity in metaheuristics refers to the variety and spread of possible solutions within the population evaluated by the algorithm. It measures how different the individuals (solutions) in the population are from each other. High diversity means the solutions are spread across a wide area of the search space, while low diversity indicates that solutions are clustered closely together. Maintaining diversity within the population in algorithms is essential in balancing exploration and exploitation. Population diversity reduces premature convergence, helping to prevent suboptimal performance. Diversity is crucial in dynamic optimization problems where the nature of the problem keeps changing. In multi-objective optimization, diversity helps to search the entire Pareto front to determine the global solution [31].

An adaptive population diversity scheme is introduced into MOGWO to deal with the issues of excessive exploration, early exploitation, and fine-tuning difficulty. The proposed adaptive population diversity scheme dynamically adjusts the parameter '$\boldsymbol{a}$' depending on the problem. The proposed scheme is presented in presented in **algorithm 1**.

Algorithm 1: Proposed adaptive scheme to tune '$\boldsymbol{a}$'

start

1 ***Set*** *diversity threshold*

2 ***For*** *each pair of wolves (i, j), calculate the Euclidean distance between their current positions in the solution space using:*

$$distance_{ij} = \left\| X_i - X_j \right\|$$

X_i and X_j are adjacent search agents (wolves).

3 *For each distance calculated, normalize the distances using:*

$$distances = \frac{distances}{max\, distances}$$

4 *Calculate the average of all normalized distances as a measure of the diversity of the*
wolves using:

$$diversity = \frac{1}{N(X) \times (N(X) - 1)} \sum_{i=i}^{N(X)-1} \sum_{j=i+1}^{N(x)} distances\ (i, j)$$

where N(X) is the number of wolves.

5 *If diversity < diversity threshold*

6 *Adjust a as;* $a = a \times 1.05$ *(exploration)*

7 *If diversity > diversity threshold*

8 *Adjust a as;* $a = a \times 0.95$ *(exploitation)*

9 *Adjust a to stay within bounds as;* $\max[0.1, \min(a, 2)]$

10 ***End***

11 ***End***

The adaptive scheme enhances MOGWO in the following ways.

- It adjusts $'\boldsymbol{a}'$ upward to allow the search agents (wolves) to explore new optimal regions by moving away from their current location when there is high level of similarity within the population.
- It adjusts $'\boldsymbol{a}'$ downwards to allow search agents to focus narrowly on richer regions when solutions are highly scattered. This encourages exploitation and enhances convergence to the optimal solution.

The adaptive technique provides flexible tuning of parameters. It not only improves convergence but also provides robustness. The scheme improves convergence because stagnation and excessive exploration are prevented. The tuning method equips MOGWO with the robustness to effectively deal with complex and diverse problems.

In addition to the adaptive scheme, a Levy flight operator is employed to enhance the algorithm. Levy flight is a random walk with a step size that follows a heavy-tailed probability distribution. This approach is used in optimization algorithms to enable a search strategy that combines local and global exploration efficiently [32]. Using steps of varying lengths, levy flight helps the algorithm explore better by reaching diverse regions and escaping local optima entrapment [33].

To implement the levy-based technique in MOGWO, the levy flight operator is introduced into (4) to modify the parameter $'\boldsymbol{C}'$. In (4), $'\boldsymbol{C}'$ is a critical parameter determining the quality of solution updates in the GWO.
The modified $'\boldsymbol{C}'$ parameter is defined according to (12)

$$\vec{C} = levy\ number\ (dependent\ on\ number\ of\ search\ agents) \tag{12}$$

Levy Flight operator is applied to equation (4) to improve MOGWO as follows.

Step 1: Calculate the step size (Δ) for the levy distribution using (13). This ensures that the step size is appropriate for the problem's dimensionality.

$$\Delta = \frac{1}{\sqrt{D}} \tag{13}$$

where D is the problem's dimension.

Step 2: Generate a random number from the Cauchy distribution as a Cauchy number (f(x)). This work uses the standard probability distribution function (PDF) with x having location parameter 0 and scale parameter 1 defined according to (14).

$$f(x) = \frac{1}{\pi(1+x^2)} \tag{14}$$

Step 3: Calculate the levy number (L) using (15).

$$L = s \times f(x) \tag{15}$$

The flow chart of EMOGWO-ADTLF incorporating adaptive population diversity and levy flight is shown in *fig. 1*.

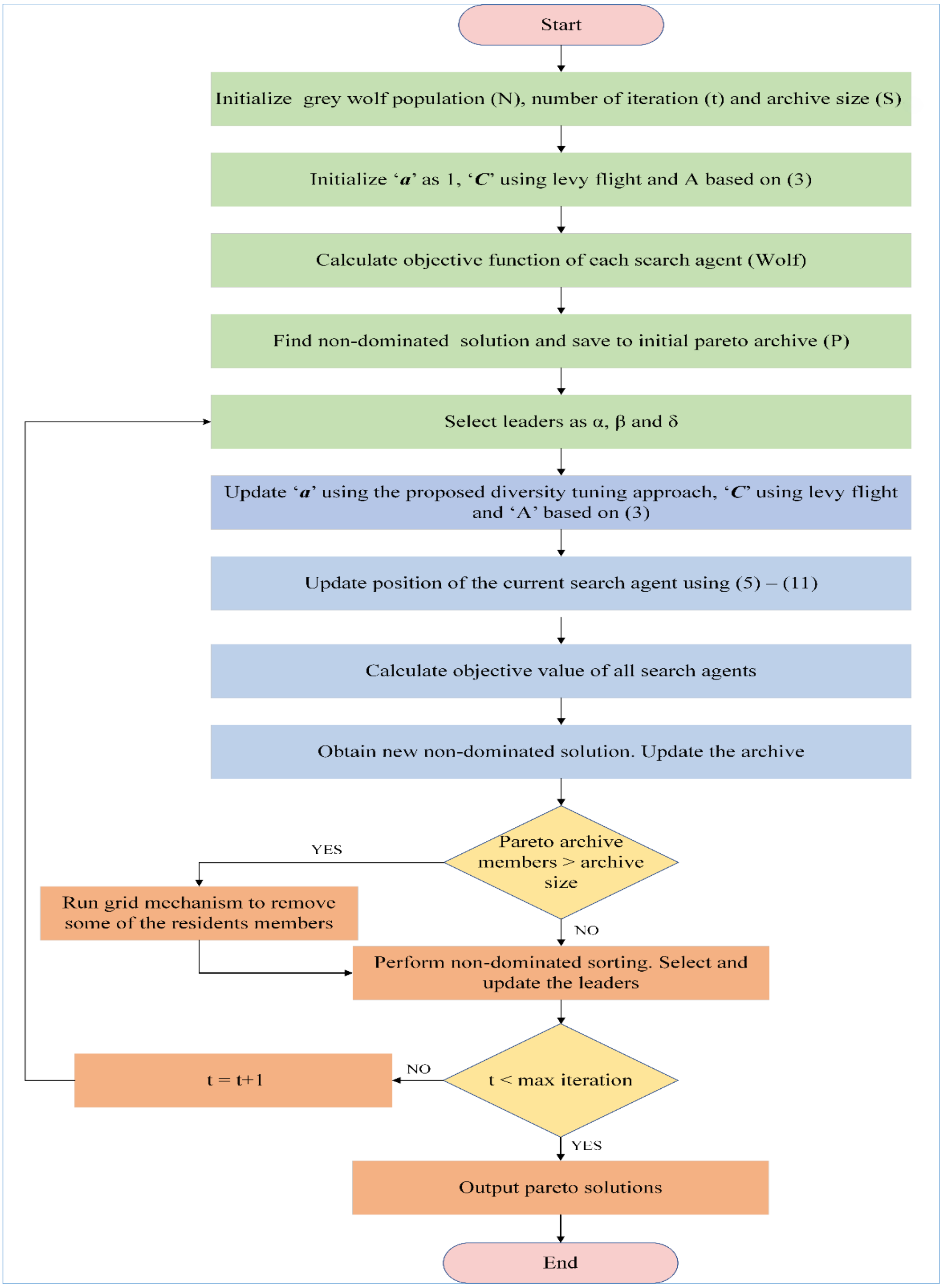

Fig. 1. Flow Chart of EMOGWO-ADTLF

3. BENCHMARK FUNCTIONS USED AND TEST PARAMETERS

3.1. Benchmark Functions

Eight standard multi-objective test functions in the CEC 2009 [34] were used as test beds. Table 1 presents the benchmark problems chosen. These test functions offer diverse multi-objective search spaces with distinct Pareto fronts, including convex, non-convex, discontinuous, and multi-modal scenarios.

In addition, this study also used two benchmark real-world engineering problems. The use of these problems demonstrates the applicability and robustness of multiobjective optimization algorithms in solving complex, real-world engineering tasks that involve multiple conflicting objectives. They include the design of the welded beam and the Disc Brake. The welded beam multi-objective design is a well-known test problem in many studies. This benchmark design has four variables. They include the beam's thickness (h), width (w), depth (d) and length (L). The objective is to reduce the fabrication cost (c) and the end deflection (δ). The main constraints are shear stress, bending stress, and buckling load [35,36]. The detailed equations of this problem are provided in Table 2.

The goals of the multiple-disc brake are to reduce the brake's mass and minimize the stopping time. The variables to be determined in the design are the force (F), the number of friction surfaces (s) as well as inner and outer radius (r and R). The design must adhere to several constraints, including the minimum allowable length between the radii, the maximum allowable length of the brake, as well as limitations related to pressure, temperature, and torque [35,36]. The objectives and constraints of this problem are also shown in Table 2.

Table 1. Test Functions, UF1 – UF8

Function	Mathematical Expression
UF1	$f_1 = x_1 + \frac{2}{\lvert J_1\rvert}\sum_{j\in J_1}\left[x_j - sin\left(6\pi x_1 + \frac{j\pi}{n}\right)\right]^2,$ $f_2 = 1-\sqrt{x} + \frac{2}{\lvert J_2\rvert}\sum_{j\in J_2}\left[x_j - sin\left(6\pi x_1 + \frac{j\pi}{n}\right)\right]^2,$ $J_1 = \{j \mid j\ is\ odd\ and\ 2 \le j \le n\},\ J_2 = \{j \mid j\ is\ even\ and\ 2 \le j \le n\}$ $PF\ f_2 = 1-\sqrt{f_1}, \quad 0 \le f_1 \le 1$
UF2	$f_1 = x_1 + \frac{2}{\lvert J_1\rvert}\sum_{j\in J_1} {y_j}^2\!:\ f_2 = 1-\sqrt{x} + \frac{2}{\lvert J_2\rvert}\sum_{j\in J_1} {y_j}^2,$ $J_1 = \{j \mid j\ is\ odd\ and\ 2 \le j \le n\},\quad J_2 = \{j \mid j\ is\ even\ and\ 2 \le j \le n\}, y_j$ $= \begin{Bmatrix} x_j - \left[0.3{x_1}^2\cos\left(24\pi x_1 + \frac{4j\pi}{n}\right) + 0.6x_1\right]\cos\left(6\pi x_1 + \frac{j\pi}{n}\right)\ if\ j \in J_1 \\ x_j - \left[0.3{x_1}^2\cos\left(24\pi x_1 + \frac{4j\pi}{n}\right) + 0.6x_1\right]\cos\left(6\pi x_1 + \frac{j\pi}{n}\right)\ if\ j \in J_2 \end{Bmatrix}$ $PF\!: f_2 = 1-\sqrt{f_1}, \quad 0 \le f_1 \le 1$

Function	Mathematical Expression
UF3	$f_1 = x_1 + \frac{2}{\lvert J_1\rvert}\left(4\sum_{j\in J_1} {y_j}^2 - 2\prod_{j\in J_1}\cos\left(\frac{20y_j\pi}{\sqrt{j}}\right)+2\right) PF: 0 \le f_1 \le 1.$ $f_2 = \sqrt{x_1} + \frac{2}{\lvert J_1\rvert}\left(4\sum_{j\in J_1} {y_j}^2 - 2\prod_{j\in J_1}\cos\left(\frac{20y_j\pi}{\sqrt{j}}\right)+2\right) PF: f_2 = 1-\sqrt{f_1}.$ $J_1\ and\ J_2 = UF1, \quad y_j = x_j - {x_j}^{0.5\left(1+\frac{3(j-2)}{n-2}\right)}, \quad j = 2,3,\ldots,n$ „
UF4	$f_1 = x_1 + \frac{2}{\lvert J_1\rvert}\sum_{j\in J_1} h(y_j) \quad f_2 = 1 - x_2 + \frac{2}{\lvert J_2\rvert}\sum_{j\in J_2} h(y_j), J_1\ and\ J_2 = UF1,$ $y_j = x_j - \sin\left(6\pi x_1 + \frac{j\pi}{n}\right), \quad j = 2,3,\ldots,n, h(t) = \frac{\lvert t\rvert}{1+e^{2\lvert t\rvert}}$ $PF: f_2 = 1 - f^2, \quad 0 \le f_1 \le 1$
UF5	$f_1 = x_1 + \left(\frac{1}{2N}\right) + \epsilon\ \lvert\sin(2N\pi x_1)\rvert + \frac{2}{\lvert J_1\rvert}\sum_{j\in J_1} h(y_j),$ $f_2 = 1 - x_1 + \left(\frac{1}{2N}\right) + \epsilon\ \lvert\sin(2N\pi x_1)\rvert + \frac{2}{\lvert J_2\rvert}\sum_{j\in J_2} h(y_j),$ $J_1\ and\ J_2 = UF1, \epsilon > 0\ y_j = x_j - \sin\left(6\pi x_1 + \frac{j\pi}{n}\right), \quad j = 2,3,\ldots,n\ , h(t)$ $= 2t^2 - \cos(4\pi t) + 1$ Its PF has $2N+1$ solutions: $\left(\frac{i}{2N}, 1-\frac{i}{2N}\right)$ for $i = 0,1,\ldots,2N$
UF6	$f_1 = x_1 + max\left\{0,2\left(\frac{1}{2N} + \epsilon\right)\sin(2N\pi x_1)\right\} + \frac{2}{\lvert J_1\rvert}\left(4\sum_{j\in J_1} {y_j}^2 -\right.$ $\left.2\prod_{j\in J_1}\cos\left(\frac{20y_j\pi}{\sqrt{j}}\right)+1\right)$ $f_2 = 1 - x_1 + max\left\{0,2\left(\frac{1}{2N} + \epsilon\right)\sin(2N\pi x_1)\right\} + \frac{2}{\lvert J_2\rvert}\left(4\sum_{j\in J_2} {y_j}^2 -\right.$ $\left.2\prod_{j\in J_2}\cos\left(\frac{20y_j\pi}{\sqrt{j}}\right)+1\right)$ $J_1\ and\ J_2 = UF1,\ y_j = x_j - \sin\left(6\pi x_1 + \frac{j\pi}{n}\right), \quad j = 2,3,\ldots,n$ *PF: One isolated* $(0,1)$, *and N disconnected:* $f_2 = 1 - f_1, f_1 \in$ $\bigcup_{i=1}^{N}\left[\frac{2i-1}{2N}, \frac{2i}{2N}\right]. N = 2$
UF7	$f_1 = \sqrt[5]{x_1} + \frac{2}{\lvert J_1\rvert}\sum_{j\in J_1} {y_j}^2 \quad f_2 = 1 - \sqrt[5]{x_1} + \frac{2}{\lvert J_2\rvert}\sum_{j\in J_2} {y_j}^2 \quad 0 \le f_1 \le 1$ $J_1\ and\ J_2 = UF1\ \ y_j = x_j - \sin\left(6\pi x_1 + \frac{j\pi}{n}\right), \quad j = 2,3,\ldots,n, PF: f_2 = 1 - f_1,$
UF8	$f_1 = \cos(0.5x_1\pi)\cos(0.5x_2\pi) + \frac{2}{\lvert J_1\rvert}\sum_{j\in J_1}\left(x_j - 2x_2\sin\left(2\pi x_1 + \frac{j\pi}{n}\right)^2\right)$ $f_2 = \cos(0.5x_1\pi)\sin(0.5x_2\pi) + \frac{2}{\lvert J_2\rvert}\sum_{j\in J_2}\left(x_j - 2x_2\sin\left(2\pi x_1 + \frac{j\pi}{n}\right)^2\right)$ $f_3 = \sin(0.5x_1\pi) + \frac{2}{\lvert J_3\rvert}\sum_{j\in J_3}\left(x_j - 2x_2\sin\left(2\pi x_1 + \frac{j\pi}{n}\right)^2\right)$ $J_1 = \{j \mid 3 \le j \le n, and\ j-1\ is\ a\ mmultiple\ of\ 3\}$ $,J_2 = \{j \mid 3 \le j \le n, and\ j-2\ is\ a\ multiple\ of\ 3\}$ PF is $f_1^2 + f_2^2 + f_3^3 = 1,$ $J_3 = \{j \mid 3 \le j \le n, and\ j\ is\ a\ multiplication\ of\ 3\}$, Its , $0 \le f_1, f_2 f_3 \le 1$

Table 2. Benchmarked Engineering Problems

Problem	Objectives and Constraints
Welded Beam Design	minimise $f_1(\boldsymbol{x}) = 1.10471w^2L + 0.04811dh(14.0 + L)$, $f_2 = \delta$, subject to $g_1(\boldsymbol{x}) = w - h \leq 0, g_2(\boldsymbol{x}) = \delta(\boldsymbol{x}) - 2.5 \times 10^{-1} \leq 0,$ $g_3(\boldsymbol{x}) = \tau(\boldsymbol{x}) - 1.36 \text{ x } 10^4\text{x} \leq 0, g_4(\boldsymbol{x}) = \sigma(\boldsymbol{x}) - 3.0 \text{ x } 10^4 \leq 0,$ $g_5(\boldsymbol{x}) = 0.10471w^2 + 0.04811hd(14 + L) - 5.0 \leq 0, g_6(\boldsymbol{x}) = 1.3 \times 10^{-1} - w \leq 0,$ $g_7(\boldsymbol{x}) = 6{,}000 - P(\boldsymbol{x}) \leq 0, 0.1 \leq L, d \leq 10$ and $1.25 \text{ x } 10^{-1} \leq w, h \leq 2.0$ where $\sigma(\boldsymbol{x}) = \frac{504{,}000}{hd^2}, \quad Q = 6{,}000\left(14 + \frac{L}{2}\right), \mathrm{D} = \frac{1}{2}\sqrt{L^2 + (w+d)^2}$ $J = \sqrt{2}wL\left[\frac{L^2}{6} + \frac{(w+d)^2}{2}\right], \delta = \frac{65{,}856}{30{,}000hd^3}, \quad \beta = \frac{QD}{J}$ $\alpha = \frac{6{,}000}{\sqrt{2}wL}, P = 0.61423 \times 10^6 \frac{dh^3}{6}\left(1 - \frac{d\sqrt{30/48}}{28}\right)$
Brake Disc Design	Minimize $f_1(\boldsymbol{x}) = 4.9 \times 10^{-5}(R^2 - r^2)(s - 1),$ $f_2(\boldsymbol{x}) = \frac{9.82 \times 10^6(R^2 - r^2)}{Fs(R^3 - r^3)}$ subject to $g_1(x) = 20 - (R - r) \leq 0,$ $g_2(x) = 2.5(s + 1) - 30 \leq 0$ $g_3(x) = \frac{F}{3.14(R^2 - r^2)} - 0.4 \leq 0,$ $g_4(\boldsymbol{x}) = \frac{2.22\times10^{-3}F(R^3 - r^3)}{(R^2 - r^2)^2} - 1 \leq 0,$ $g_5(\boldsymbol{x}) = 900 - \frac{2.66 \text{ x } 10^{-2}Fs(R^3 - r^3)}{(R^2 - r^2)} \leq 0.$ $5.5 \text{ x } 10 \leq r \leq 8.0 \text{ x } 10, 7.5 \text{ x } 10 \leq R \leq 1.1 \text{ x } 10^2$ $1.0 \text{ x } 10^3 \leq F \leq 3.0 \text{ x } 10^3, 2 \leq s \leq 20.$

3.2. Performance Metrics

This study uses two performance metrics with abilities to test for convergence, diversity, and spread to measure the performance of the EMOGWO-ADTLF and compare it with other muti-objective algorithms. The metrics include Inverted Generational Distance (IGD) [37] and Hypervolume (HV) [38].

IGD is a measue that determines the diversity and convergence of a multi-objective algorithm. It assesses how close the obtained solutions are to the Pareto front. It also determines how the obtained solution spread over the Pareto solution. The value of IGD obtained is an indication of how well an algorithm maintains its balance. A low IGD value shows an algorithm is well balanced. It shows that the algorithm is neither wandering in non-optimal regions (over-exploration) nor stuck in local optima (over-exploitation) [37]. IGD is mathematically represented as (19).

$$IGD = \frac{\sqrt{\sum_{i=1}^{n} d_i^2}}{n} \tag{19}$$

where n is the count of pareto solutions, d_i indicates the euclidean distance from the ith pareto optimal solution and the nearest obtained solution.

HV is a performance metric that measures the volume of the Pareto front occupied by the obtained solution. It measures diversity, convergence and spread of the solution. It is a widely used metric for benchmarking the performance of multi-objective optimizers. The HV is determined with respect to a reference point. The reference point is a value worse than the any value in the obtained Pareto solutions. A high hypervolume means a better diversity, convergence, and distribution of the obtained solution. Mathematically, HV is given by (20) [38].

$$HV(S, r) = \lambda_m(\cup_{z \in S} \ [z; r]) \tag{20}$$

λ_m is the Lebesgue measure. It is the size of true Pareto front occupied by the solution. m is the number of objectives. $\cup_{z \in S}$ is the union of points z in the set S. r is the reference point.

3.3. Experimental Setups

The study used two experimental setups. The first experiment compared EMOGWO-ADTLF with MOGWO and two high-performing other variants of MOGWO in the literature namely NSGWO [25] and DCMOGWO [21]. This experiment analyzed the graphs of obtained Pareto against true Pareto and determined IGD and HV values. The second experiment also compared EMOGWO-ADTLF to three well-known, efficient, and robust algorithms. They include Multi-Objective Mayfly Algorithm (MMA) [39] , Multi-Objective Ant Lion Optimizer (MOALO) [36] and Multi-Objective Dragonfly Algorithm (MODA) [40] using multi-objective test functions. In the third experiment, MOGWO was again compared with MMA, MOALO and MODA using real-world engineering benchmarked problems. The metrics of comparison were the IGD and HV.

This work used MATLAB 2021 to execute all algorithms to obtain the Pareto solutions. The general parameters of all algorithms were as follows:

- Number of search agents: 100
- Number of iterations: 3000

- Number of runs: 03
- Archive size: 100.

These parameters were selected to guarantee a thorough and efficient evaluation of the multi-objective algorithms. Utilizing 100 search agents strikes a practical balance, offering enough diversity without excessively taxing computational resources. The selected 3000 iterations ensure the search process is detailed enough to discover and refine multiple solutions, accounting for the complexity and multi-objective nature of the problems. An archive size of 100 maintains a balance between storing a diverse set of Pareto-optimal solutions and managing computational resources. Conducting multiple runs provides statistically significant insights into the performance of the algorithms.

Subsequently, there were comparisons of obtained Pareto solutions and true Pareto fronts using the Python library Pymoo. Pymoo is a specialized multi-objective optimization and analysis tool. The desktop computer used for this study was an HP ZB G4 workstation with the processor Intel® Xeon ® Silver 4108 CPU @ 1.80 GHz (16 CPUs) and memory of 64 GB. This specification provided enough computational power and efficiency for the rigorous simulations and computations in this work.

4. RESULTS AND DISCUSSIONS

4.1. Analysis of EMOGWO-ADTLF against MOGWO and its Variants

Fig. 2 presents the plots of the obtained Pareto fronts against the true Pareto fronts for UF1 to UF3. In the UF1 graph, EMOGEO-ADTFL and MOGWO show better convergence and spread than NSGWO and DCMOGWO. EMOGWO-ADT has a better distribution of Pareto solutions than MOGWO. All algorithms show better convergence, diversity, and distribution in UF2 than in UF1. Of the four algorithms, NSGWO shows better coverage. In UF3, the algorithms struggle to approximate the Pareto fronts with EMOGWO-ADTLF having better spread and convergence than the rest.

Fig. 3 shows the graph of test functions UF4. UF5 and UF6. In UF4, EMOGWO-ADTLF and DCMOGWO closely approximate the Pareto fronts and have better spread. NSGWO and MOGWO show good convergence, but poor distribution compared to EMOGWO-ADTLF and DCMOGWO. All the algorithms find it difficult to approximate the Pareto fronts in UF5 and UF6, with only a few non-dominated Pareto solutions. NSGWO appears to have a better convergence and spread than the rest in UF6.

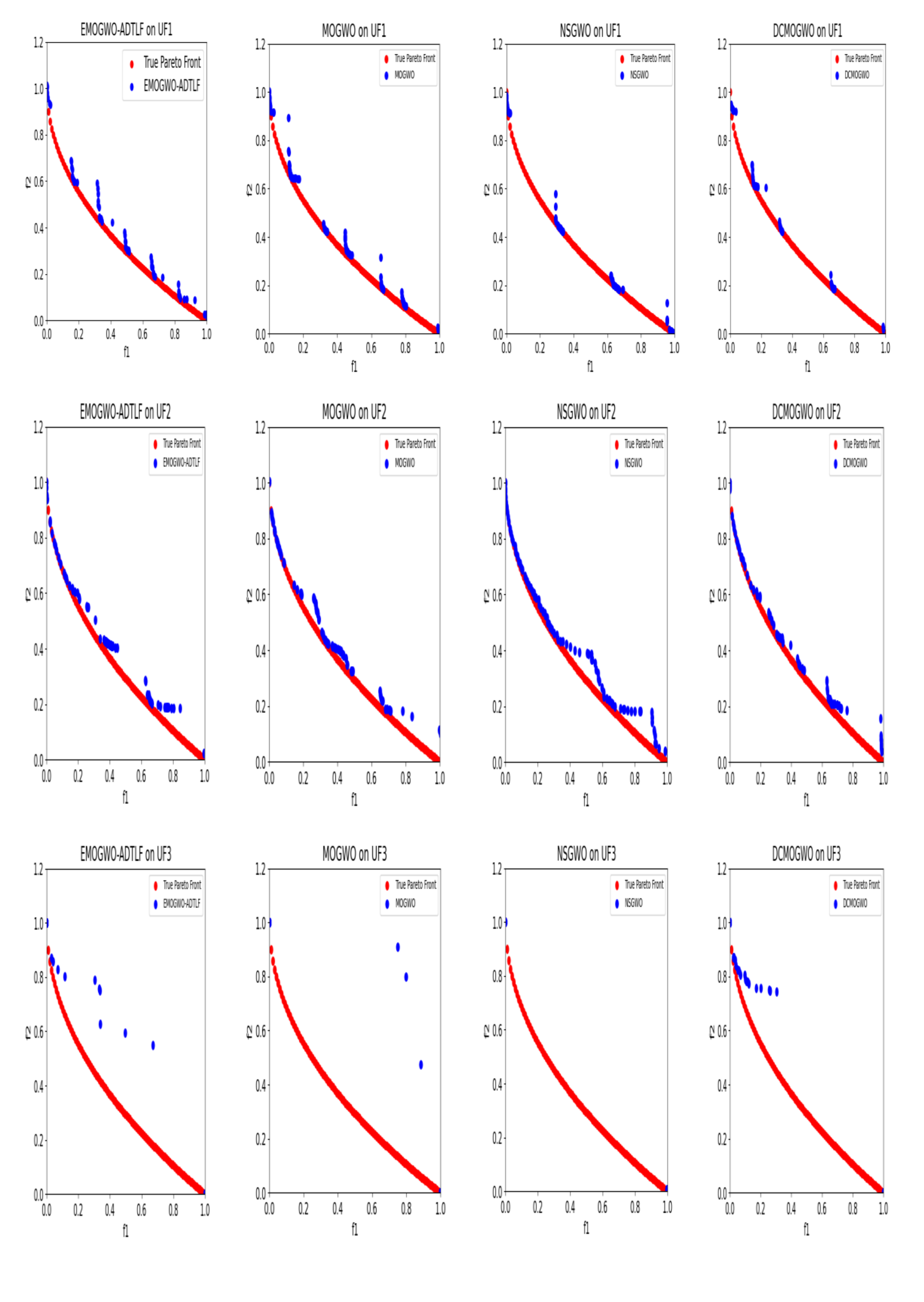

Fig. 2: Graph of test functions UF1, UF2 and UF3

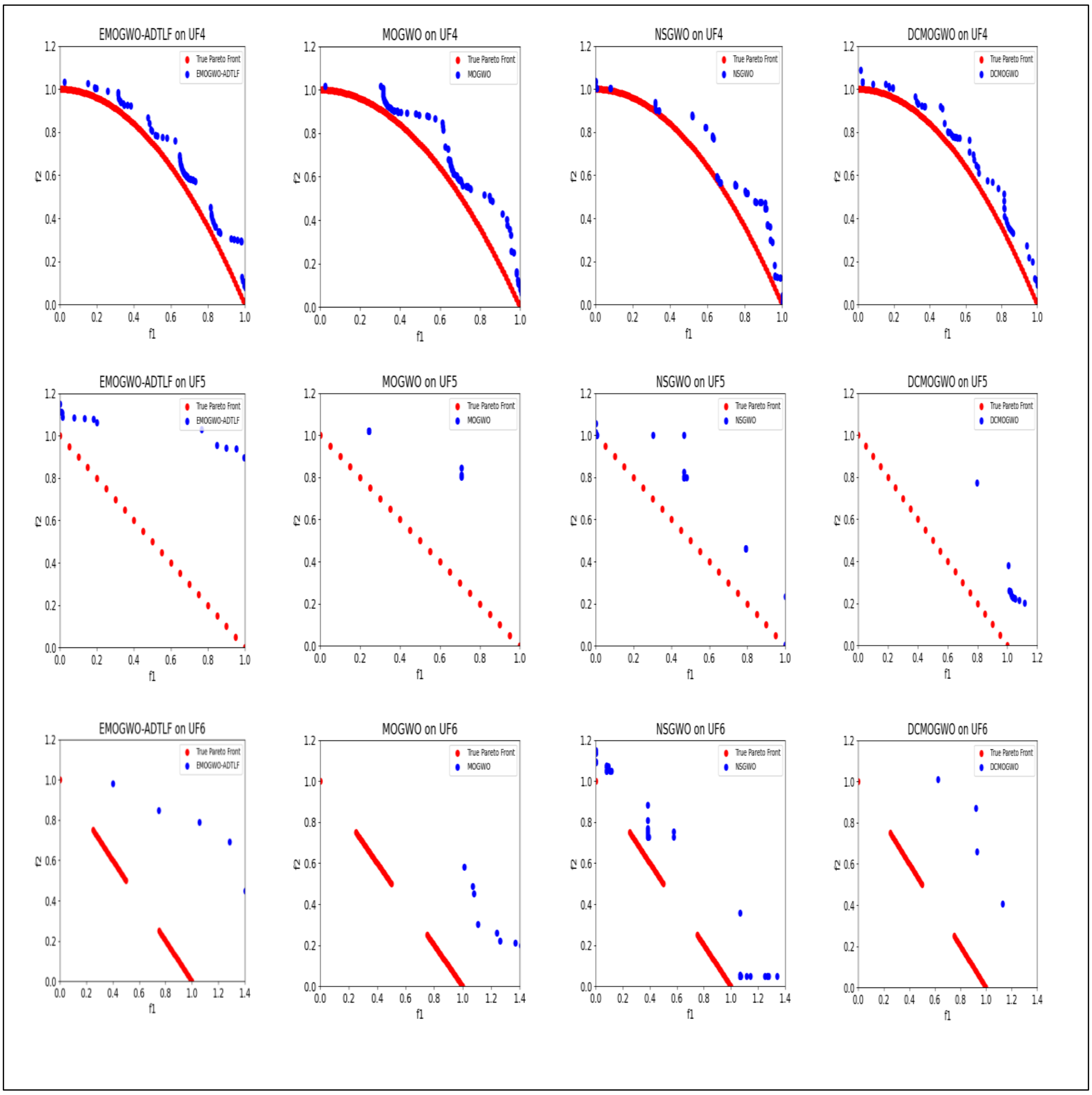

Fig. 3: Graph of test functions UF4, UF5 and UF6

The plots of Pareto solutions for the algorithms are shown in *fig. 4*. For the UF7, EMOGWO-ADTLF shows better convergence, spread and distribution than the rest of the algorithms. MOGWO shows good spread but poor distribution while NSGWO and DCMOGWO struggle with both spread and distribution. In the three-dimension UF8 function, EMOGWO-ADTLF and NSGWO have better spread and distribution but not all the obtained Pareto fronts converge to the Pareto front. MOGWO has good convergence but struggles with spread and coverage. DCMOGWO has poor convergence, spread and distribution.

Overall, EMOGWO-ADTLF shows a consistent close approximation of the Pareto fronts in most of the test functions. NSGWO, MOGWO and DCMOGWO perform variably across the test functions. It shows reasonable approximations but sometimes suffers from spread and distribution. DCMOGWO and MOGWO's performance reduces as the complexity of the functions increases.

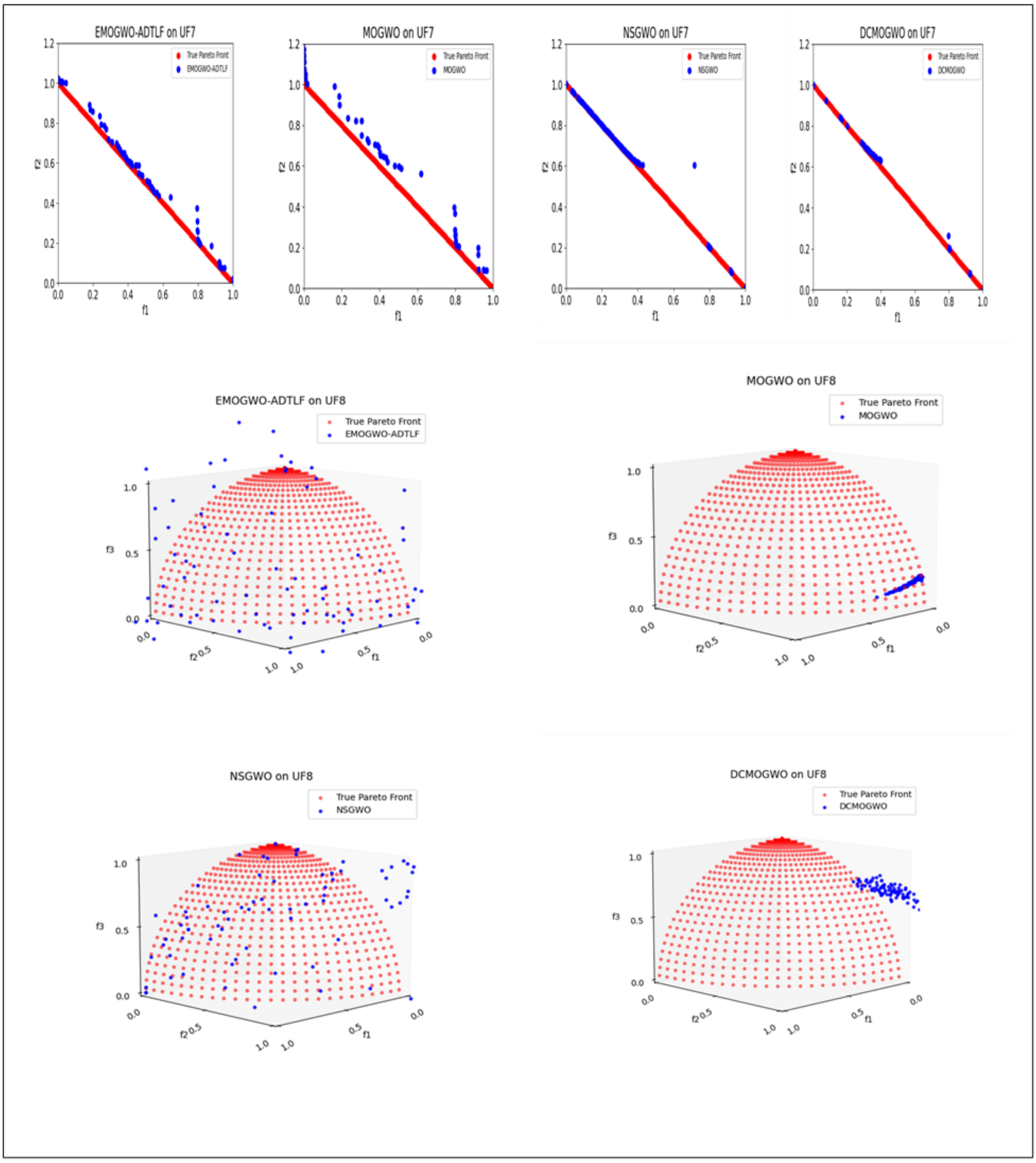

Fig. 4: Graph of test functions UF7 and UF8

4.1.1. Analysis of IGD and HV Values for EMOGWO-ADTLF and MOGWO Variants

The results of IGD values for EMOGWO-ADTLF, MOGWO, NSGWO and DCMOGWO are presented in Table 3. The statistical measures are the average (AVG), median (MDN), standard deviation (SD), best score (BS) and worst score (WS). In UF1, EMOGWO-ADTLF dominates in the performance metrics, obtaining the best values in average, median, best and worst score values. For this function, EMOGWO-ADTLF shows high diversity and convergence. This implies the algorithm can balance exploration and exploitation for this test function. DCMOGWO outperforms NSGWO and MOGWO in terms of average IGD but below EMOGWO-ADTLF. NSGWO has the best standard deviation value. For the UF2 function, EMOGWO-ADTLF has the best possible value, but its best average value is slightly below NSGWO. In UF3, UF4 and UF6 functions, EMOGWO-ADTLF dominates in both average and best scores. This again shows the strength of EMOGWO-ADTLF to provide convergence and diversity in these functions. NSGWO shows strength in closely approximating the Pareto fronts in the UF6 function. It dominates in four of the performance metrics. In UF7, EMOGWO-ADTLF shows its highest strength, dominating in all the performance metrics. It is an indication of the ability of MOGWO-ADTLF to handle complex problems. NSGWO has the lowest average, median, standard deviation, and worst values in UF8. This performance of EMOGWO-ADTLF closely follows NSGWO. Both MOGWO and DCMOGWO struggle to handle this complex problem. For this three-dimensional problem function, NSGWO and EMOGWO-ADTLF have better diversity and convergence.

Across all the functions, EMOGWO-ADTLF frequently performs better than other algorithms in terms of IGD, showing high effectiveness and efficiency. This is proof of convergence and diversity. It demonstrates the ability of EMOGWO-ADTLF to provide a balance between exploration and exploitation as well as closely approximating the Pareto fronts. NSGWO also shows competitive performance especially in complex problems.

Table 4 presents the HV value for EMOGWO-ADTLF, MOGWO, NSGWO and DCMOGWO. EMOGWO-ADTLF has the highest values in terms of average, median and worst values in UF1 and UF2. It also has the highest best value in UF1. This shows that the Pareto solutions of EMOGWO-ADTLF cover the objective space effectively in both functions. MOGWO and DCMOGWO are the second-best performers for UF1 with NSGWO providing competitive performance to EMOGWO-ADTLF in UF2, obtaining the highest best value. The dominance of EMOGWO-ADTLF continues in both UF3 AND UF4, obtaining the highest scores in average, median and best values. DCMOGWO outperforms MOGWO and NSGWO in the two test problems. NSGWO also covers the objective space effectively in UF5 and UF6. It obtains the highest HV values in four of the performance metrics in both functions. In UF7 and UF8, EMOGWO-ADTLF again shows dominant performance in the performance metrics. It also indicates the strength of EMOGWO-ADTLF in handling complex problems more effectively. The performance of EMOGWO-ADTLF in these test functions is followed by NSGWO.MOGWO and DCMOGWO are the worst performing algorithms in UF7 and UF8 respectively.

EMOGWO-ADTLF more often performs better than other algorithms in terms of HV, obtaining the highest or near-highest HV values. It also gives competitive standard deviation values. This shows how effective EMOGWO-ADTLF covers the objective space and is a good algorithm for different optimization problems. NSGWO also performs well in certain functions, but its performance fluctuates depending on the problem being considered.

Table 3. Analysis of IGD Values

FUNCTION	STATISTICS	EMOGWO-ADTLF	MOGWO	NSGWO	DCMOGWO
UF1	AVG	**5.7969E-02**	7.1311E-02	7.9473E-02	6.7857E-02
	MDN	**5.7273E-02**	8.4320E-02	7.6504E-02	6.5035E-02
	SD	1.4157E-02	2.0105E-02	**4.7193E-03**	1.4144E-02
	BS	**4.0989E-02**	4.2911E-02	7.5781E-02	5.2119E-02
	WS	**7.5646E-02**	8.6701E-02	8.6134E-02	8.6418E-02
UF2	AVG	3.3437E-02	4.5888E-02	**3.2598E-02**	4.1171E-02
	MDN	**3.2656E-02**	4.5811E-02	3.2813E-02	4.1180E-02
	SD	1.7721E-03	2.3011E-03	3.1591E-04	**2.9645E-04**
	BS	**3.1764E-02**	4.3109E-02	3.2151E-02	4.0804E-02
	WS	3.5889E-02	4.8744E-02	**3.2829E-02**	4.1530E-02
UF3	AVG	**2.8641E-01**	3.4817E-01	3.8643E-01	3.0021E-01
	MDN	**3.2332E-01**	3.4253E-01	3.8653E-01	**3.2333E-01**
	SD	5.9279E-02	**1.1552E-02**	6.7217E-04	3.3181E-02
	BS	**2.0276E-01**	3.3771E-01	3.8556E-01	2.5329E-01
	WS	3.3313E-01	3.6427E-01	3.8720E-01	**3.2402E-01**
UF4	AVG	**4.9430E-02**	5.8564E-02	6.9335E-02	5.1609E-02
	MDN	**4.9253E-02**	5.3530E-02	6.5971E-02	5.1530E-02
	SD	1.1361E-03	1.0918E-02	7.1741E-03	**9.7808E-04**
	BS	**4.8136E-02**	4.8441E-02	6.2727E-02	5.0453E-02
	WS	**5.0902E-02**	7.3722E-02	7.9306E-02	5.2845E-02
UF5	AVG	**4.7367E-01**	4.7994E-01	1.7046E+00	5.4062E-01
	MDN	5.3407E-01	5.2411E-01	1.7113E+00	**5.2327E-01**
	SD	1.4897E-01	1.1658E-01	**1.0118E-02**	9.8080E-02
	BS	**2.6869E-01**	3.2030E-01	1.6903E+00	4.3011E-01
	WS	6.1826E-01	**5.9541E-01**	1.7122E+00	6.6847E-01
UF6	AVG	6.5347E-01	5.7803E-01	**2.0821E-01**	4.4295E-01
	MDN	6.5014E-01	5.8364E-01	**1.7291E-01**	4.3031E-01
	SD	**4.1635E-02**	7.9377E-02	5.7970E-02	1.0207E-01
	BS	6.0423E-01	4.7813E-01	**1.6178E-01**	3.2474E-01
	WS	7.0605E-01	6.7232E-01	**2.8994E-01**	5.7380E-01
UF7	AVG	**4.2915E-02**	1.4181E-01	5.7573E-02	6.1463E-02
	MDN	**4.7423E-02**	6.8108E-02	5.7461E-02	6.3971E-02
	SD	**9.0520E-03**	1.1060E-01	1.0112E-02	7.8416E-03
	BS	**3.0284E-02**	5.9182E-02	4.5245E-02	5.0854E-02
	WS	**5.1036E-02**	2.9813E-01	7.0013E-02	6.9564E-02
UF8	AVG	1.6637E-01	9.1158E-01	**1.5490E-01**	1.3326E+00
	MDN	1.6880E-01	9.1806E-01	**1.5476E-01**	9.1289E-01
	SD	1.1489E-02	2.6171E-02	**1.3674E-03**	6.4448E-01
	BS	**1.5124E-01**	8.7678E-01	1.5329E-01	8.4183E-01
	WS	1.7906E-01	9.3990E-01	**1.5663E-01**	2.2431E+00

Table 4. Analysis of HV Values

FUNCT-ION	STATI-STICS	EMOGWO-ADTLF	MOGWO	NSGWO	**DCMOGWO**
UF1	AVG	**1.0012E+00**	9.6216E-01	9.6603E-01	9.7232E-01
	MDN	**1.0095E+00**	9.4560E-01	9.6965E-01	9.7123E-01
	SD	2.5703E-02	2.9627E-02	**5.8174E-03**	1.8139E-02
	BS	**1.0278E+00**	1.0038E+00	9.7063E-01	9.9507E-01
	WS	**9.6647E-01**	9.3711E-01	9.5783E-01	9.5068E-01
UF2	AVG	**1.0539E+00**	1.0317E+00	1.0516E+00	5.9579E-01
	MDN	**1.0550E+00**	1.0286E+00	1.0543E+00	5.9458E-01
	SD	1.9074E-03	6.0224E-03	4.9418E-03	**1.7843E-03**
	BS	1.0554E+00	1.0402E+00	**1.0558E+00**	5.9831E-01
	WS	**1.0512E+00**	1.0264E+00	1.0446E+00	5.9448E-01
UF3	AVG	**6.3035E-01**	5.1864E-01	4.4334E-01	6.1075E-01
	MDN	**5.6133E-01**	5.2197E-01	4.4324E-01	5.6512E-01
	SD	1.0299E-01	9.8704E-03	**4.8824E-04**	6.6666E-02
	BS	**7.7593E-01**	5.2871E-01	4.4398E-01	7.0501E-01
	WS	5.5379E-01	5.0523E-01	4.4279E-01	**5.6211E-01**
UF4	AVG	**6.7915E-01**	6.6562E-01	6.6183E-01	6.7300E-01
	MDN	**6.7905E-01**	6.7018E-01	6.6571E-01	6.7250E-01
	SD	2.2381E-03	1.3642E-02	7.6380E-03	**1.2247E-03**
	BS	**6.8195E-01**	6.7958E-01	6.6862E-01	6.7400E-01
	WS	**6.7647E-01**	6.4711E-01	6.5116E-01	6.7100E-01
UF5	AVG	7.6565E-01	8.8663E-01	**1.4245E+00**	6.7332E-01
	MDN	6.3858E-01	8.7735E-01	**1.4244E+00**	7.7173E-01
	SD	3.1557E-01	**1.2209E-01**	1.4060E-01	1.5154E-01
	BS	1.1997E+00	1.0406E+00	**1.5968E+00**	7.8899E-01
	WS	4.5868E-01	7.4196E-01	**1.2524E+00**	4.5925E-01
UF6	AVG	5.0265E-01	5.6163E-01	**1.2720E+00**	7.9419E-01
	MDN	5.1714E-01	5.1641E-01	**1.3061E+00**	7.4149E-01
	SD	**2.4046E-02**	6.8006E-02	6.2818E-02	1.1729E-01
	BS	5.2205E-01	6.5775E-01	**1.3259E+00**	9.5675E-01
	WS	4.6876E-01	5.1073E-01	**1.1839E+00**	6.8433E-01
UF7	AVG	**8.6040E-01**	7.3017E-01	8.4892E-01	8.2923E-01
	MDN	**8.5256E-01**	8.1323E-01	8.4898E-01	8.2506E-01
	SD	1.6666E-02	1.2832E-01	2.4668E-02	**1.1276E-02**
	BS	**8.8357E-01**	8.2836E-01	8.7910E-01	8.4465E-01
	WS	**8.4506E-01**	5.4891E-01	8.1867E-01	8.1799E-01
UF8	AVG	**2.4020E+00**	1.0239E+00	2.2615E+00	4.4310E-01
	MDN	**2.4011E+00**	1.0425E+00	2.2783E+00	2.8703E-01
	SD	**3.2163E-02**	5.6601E-02	4.5080E-02	4.3959E-01
	BS	**2.4419E+00**	1.0820E+00	2.3063E+00	1.0423E+00
	WS	**2.3631E+00**	9.4713E-01	2.1998E+00	0.0000E+00

4.2. Analysis of EMOGWO-ADTLF against Other Multi-Objective Optimizers

Table 5 presents the results of IGD values. EMOGWO-ADTLF dominates other algorithms in UF1 and UF2 functions. It achieves the lowest IGD value in terms of average, median, best and worst values. It also gives the lowest standard deviation value for UF2. In UF3, MODA outperforms all the algorithms, obtaining the best value in terms of average, median, standard deviation and worst scores. MOALO and EMOGWO-ADLLF provide competitive scores with MMA trailing all algorithms. EMOGWO-ADTLF obtains the lowest values in all the statistical metrics in UF4, showing more diversity and convergence in this problem. For the UF5, EMOGWO-ADTLF has the best values in overall best and average values. MOALO provides competitive performance, achieving the lowest median and worst value. MODA has the lowest standard deviation for this function. MOALO is the most dominant algorithm in the UF6 function. It has the best values for four of the metrics, including average values. EMOGWO-ADTLF again has the lowest values for all the performance metrics in UF7 and UF8. This is a clear indication of the ability of EMOGWO-ADTLF to approximate the Pareto fronts and provide a balance between exploitation and exploration in complex problems.

In all the IGD values, EMOGWO-ADTLF emerges as the top performer in most of the functions. It highlights the algorithm’s effectiveness, efficiency, diversity and adaptability in different problems. The other algorithms also show competitiveness in a few test problems. MODA’s overall performance is better than MOALO and MMA.

The analysis of HV values is shown in Table 6. In the UF1 and UF2 functions, EMOGWO-ADTLF has the highest values in average, median, best and worst values. It also has the best standard deviation value. This proves that EMOGWO-ADTLF has the best coverage and spread for these functions. MODA is the second-best performer for UF1 function with MOALO providing competitive performance to EMOGWO-ADTLF in UF2. MODA has dominant performance in the UF3 function, showing its ability to cover the objective space more effectively. The performance of MODA in UF3 is followed by MOALO and EMOGWO-ADTLF. EMOGWO-ADTLF again outperforms all the other algorithms in UF4. The second-best performer for this test function is MODA. In UF5 and UF6, MOALO is the top performer in terms of HV values. It has the best average, median and worst values. Its overall highest average value suggests that it effectively occupies the objective space. The performance of MOALO in test function UF5 is closely followed by EMOGWO-ADTLF. EMOGWO-ADTLF has the highest values in all the statistical metrics for test functions UF7 and UF8. This is an indication of the algorithm’s ability to produce solutions that cover the objective space. The performance is also a proof of the algorithm to perform in complex and high-dimension problems. MODA’s performance in these two test functions is better than MMA and MOALO.

In the HV analysis, EMOGWO-ADTLF obtained the best HV value in most of the test functions. It indicates the effectiveness of EMOGWO-ADTLF. It can produce diverse and quality solutions, with effective distribution in the objective space.

Table 5. Analysis of IGD Values

FUNCT-ION	STATI-STICS	EMOGWO-ADTLF	MMA	MOALO	MODA
UF1	AVG	**5.7969E-02**	5.0362E-01	1.2529E-01	8.0228E-02
	MDN	**5.7273E-02**	3.6851E-01	1.2531E-01	7.6724E-02
	SD	1.4157E-02	2.0709E-01	**5.0827E-03**	5.6834E-03
	BS	**4.0989E-02**	3.4614E-01	1.1906E-01	7.5715E-02
	WS	**7.5646E-02**	7.9621E-01	1.3151E-01	8.8244E-02
UF2	AVG	**3.3437E-02**	4.6596E-01	1.0055E-01	1.3648E-01
	MDN	**3.2656E-02**	4.8933E-01	9.5645E-02	1.5505E-01
	SD	**1.7721E-03**	4.6445E-02	8.2915E-03	5.5666E-02
	BS	**3.1764E-02**	4.0111E-01	9.3785E-02	6.0944E-02
	WS	**3.5889E-02**	5.0743E-01	1.1223E-01	1.9345E-01
UF3	AVG	2.8641E-01	4.9969E-01	2.2076E-01	**1.6356E-01**
	MDN	3.2332E-01	3.6962E-01	2.5563E-01	**1.5164E-01**
	SD	5.9279E-02	2.0679E-01	7.3376E-02	**2.3194E-02**
	BS	2.0276E-01	3.3789E-01	**1.1869E-01**	1.4306E-01
	WS	3.3313E-01	7.9157E-01	2.8797E-01	**1.9599E-01**
UF4	AVG	**4.9430E-02**	4.0835E-01	1.2166E-01	9.0255E-02
	MDN	**4.9253E-02**	4.3332E-01	1.2421E-01	8.5741E-02
	SD	**1.1361E-03**	1.4044E-01	1.3229E-02	9.3001E-03
	BS	**4.8136E-02**	2.2522E-01	1.0433E-01	8.1813E-02
	WS	**5.0902E-02**	5.6650E-01	1.3643E-01	1.0321E-01
UF5	AVG	**4.7367E-01**	6.7863E-01	4.7680E-01	7.0163E-01
	MDN	5.3407E-01	7.8823E-01	**4.4111E-01**	7.1891E-01
	SD	1.4897E-01	1.9160E-01	1.0164E-01	**5.1014E-02**
	BS	**2.6869E-01**	4.0923E-01	3.7405E-01	6.3233E-01
	WS	6.1826E-01	8.3844E-01	**6.1523E-01**	7.5365E-01
UF6	AVG	6.5347E-01	7.6945E-01	**3.7119E-01**	4.7254E-01
	MDN	6.5014E-01	8.5334E-01	**3.5630E-01**	4.3815E-01
	SD	**4.1635E-02**	2.2029E-01	6.3267E-02	4.9282E-02
	BS	6.0423E-01	4.6767E-01	**3.0223E-01**	4.3723E-01
	WS	7.0605E-01	9.8734E-01	**4.5504E-01**	5.4223E-01
UF7	AVG	**4.2915E-02**	4.5262E-01	1.8774E-01	6.8319E-02
	MDN	**4.7423E-02**	4.6748E-01	1.8716E-01	6.3320E-02
	SD	**9.0520E-03**	3.2862E-02	2.1535E-02	1.1269E-02
	BS	**3.0284E-02**	4.0706E-01	1.6166E-01	5.7714E-02
	WS	**5.1036E-02**	4.8333E-01	2.1440E-01	8.3923E-02
UF8	AVG	**1.6637E-01**	6.1608E-01	5.9863E-01	2.8547E-01
	MDN	**1.6880E-01**	6.0978E-01	6.1293E-01	3.1074E-01
	SD	**1.1489E-02**	1.0405E-02	3.6773E-02	3.7108E-02
	BS	**1.5124E-01**	6.0772E-01	5.4818E-01	2.3300E-01
	WS	**1.7906E-01**	6.3075E-01	6.3479E-01	3.1266E-01

Table 6. Analysis of HV Analysis

FUNCT-ION	STATI-STICS	EMOGWO-ADTFL	MMA	MOALO	MODA
UF1	AVG	**1.0012E+00**	5.0912E-01	8.9127E-01	9.5553E-01
	MDN	**1.0095E+00**	5.5278E-01	9.0266E-01	9.6276E-01
	SD	2.5703E-02	1.5508E-01	2.1287E-02	**1.0963E-02**
	BS	**1.0278E+00**	6.7343E-01	9.0971E-01	9.6380E-01
	WS	**9.6647E-01**	3.0116E-01	8.6144E-01	9.4004E-01
UF2	AVG	**1.0539E+00**	6.3847E-01	9.3339E-01	8.8999E-01
	MDN	**1.0550E+00**	6.3588E-01	9.4018E-01	8.7718E-01
	SD	**1.9074E-03**	2.2371E-02	1.5247E-02	8.5429E-02
	BS	**1.0554E+00**	6.6707E-01	9.4771E-01	1.0004E+00
	WS	**1.0512E+00**	6.1246E-01	9.1227E-01	7.9236E-01
UF3	AVG	6.3035E-01	5.1276E-01	7.5304E-01	**8.3905E-01**
	MDN	5.6133E-01	5.5765E-01	6.8235E-01	**8.6249E-01**
	SD	1.0299E-01	1.5291E-01	1.1236E-01	**5.2533E-02**
	BS	7.7593E-01	6.7351E-01	**9.1163E-01**	8.8839E-01
	WS	5.5379E-01	3.0711E-01	6.6512E-01	**7.6628E-01**
UF4	AVG	**6.7915E-01**	2.4300E-01	5.3547E-01	6.0787E-01
	MDN	**6.7905E-01**	1.9718E-01	5.2094E-01	6.1510E-01
	SD	**2.2381E-03**	7.5948E-02	2.6513E-02	1.8308E-02
	BS	**6.8195E-01**	3.5004E-01	5.7267E-01	6.2578E-01
	WS	**6.7647E-01**	1.8178E-01	5.1280E-01	5.8272E-01
UF5	AVG	7.6565E-01	4.3639E-01	**8.0392E-01**	3.4721E-01
	MDN	6.3858E-01	2.7468E-01	**9.0798E-01**	3.5879E-01
	SD	3.1557E-01	2.6200E-01	1.4734E-01	**7.9437E-02**
	BS	**1.1997E+00**	8.0596E-01	9.0822E-01	4.3819E-01
	WS	4.5868E-01	2.2854E-01	**5.9556E-01**	2.4464E-01
UF6	AVG	5.0265E-01	3.9110E-01	**8.4325E-01**	7.4843E-01
	MDN	5.1714E-01	1.4209E-01	**8.5421E-01**	8.4941E-01
	SD	**2.4046E-02**	3.9479E-01	8.2956E-02	1.4449E-01
	BS	5.2205E-01	**9.4837E-01**	9.3892E-01	8.5178E-01
	WS	4.6876E-01	8.2837E-02	**7.3661E-01**	5.4410E-01
UF7	AVG	**8.6040E-01**	4.2255E-01	6.5250E-01	7.9854E-01
	MDN	**8.5256E-01**	4.0710E-01	6.6287E-01	8.0661E-01
	SD	**1.6666E-02**	2.6991E-02	4.7455E-02	2.3511E-02
	BS	**8.8357E-01**	4.6050E-01	7.0474E-01	8.2244E-01
	WS	**8.4506E-01**	4.0005E-01	5.8990E-01	7.6657E-01
UF8	AVG	**2.4020E+00**	1.0252E+00	1.0918E+00	1.6236E+00
	MDN	**2.4011E+00**	1.0421E+00	9.4338E-01	1.5231E+00
	SD	**3.2163E-02**	5.3716E-02	2.1962E-01	3.0756E-01
	BS	**2.4419E+00**	1.0809E+00	1.4023E+00	2.0404E+00
	WS	**2.3631E+00**	9.5263E-01	9.2974E-01	1.3074E+00

4.3. Summary of IGD and HV Values for Test Function UF1 to UF8

In this section, average IGDs and HVs are used to rank all algorithms. The use of average values for ranking provides the overall performance of the algorithms. It is the statistical measure that gives a clear indication of an algorithm's convergence towards the Pareto solutions. It also provides details about the efficiency, spread coverage and diversity of an algorithm. Tables 7 and 8 provide the average IGD and HV values of all the algorithms used in this study.

EMOGWO-ADTLF shows consistently high performance in IGD and HV values. It ranks first in both performance metrics with overall rank scores of 17 and 18 in terms of IGD and HV values respectively. For IGD values, NSGWO and DCMOGWO placed second and third positions with overall rank scores of 26 and 28. MMA is the worst performing algorithm. NSGWO and MOGWO are the second and third best algorithms for the HV values ranking. MMA again is the worst performing algorithm in the HV score ranking with MOALO and DCMOGWO placing fourth.

In general, EMOGWO-ADTLF dominates both IGD and HV values. This shows that EMOGWO-ADLF has the best diversity, convergence and coverage among all the algorithms. The best diversity proves the ability of the algorithm to balance between exploitation and exploration in most of the functions. The variability of the other algorithms across the test function shows that their performances depend on the problem being analysed. The consistently low performance of MMA is a sign that it needs to be improved to be able to correctly approximate the Pareto fronts.

Table 7. Ranking of IGD Values

FUNCT-ION	EMOGWO-ADTLF	MOGWO	NSGWO	DCMOG-WO	MMA	MOALO	MODA
UF1	1	3	4	2	7	6	5
UF2	2	4	1	3	7	5	6
UF3	3	5	6	4	7	2	1
UF4	1	3	4	2	7	6	5
UF5	1	3	7	4	5	2	6
UF6	6	5	1	3	7	2	4
UF7	1	5	2	3	7	6	4
UF8	2	6	1	7	5	4	3
TOTAL	17	34	26	28	52	33	34
TOTAL RANK	**1**	**5**	**2**	**3**	**7**	**4**	**5**

Table 8. Ranking of HV Values

FUNCT-ION	EMOGWO-ADTFL	MOGWO	NSGWO	DCMOG-WO	MMA	MOALO	MODA
UF1	1	2	4	2	7	6	5
UF2	1	3	2	7	6	4	5
UF3	3	5	7	4	6	2	1
UF4	1	3	4	2	7	6	5
UF5	4	2	1	5	6	3	7
UF6	6	5	1	3	7	2	4
UF7	1	5	2	3	7	6	4
UF8	1	6	2	7	5	4	3
TOTAL	18	31	23	33	51	33	34
TOTAL RANK	**1**	**3**	**2**	**4**	**7**	**4**	**6**

4.4. Wilcoxon Signed-Rank Test on Average IGD Values

The Wilcoxon signed-rank test was employed to assess whether the optimization performance of EMOGWO-ADTLF is statistically different from other algorithms. The test was conducted at a significance level of 0.05. The data used for the test were obtained from Tables 3 and 5, and the outcomes are summarized in Table 7. In this table, $R+$ represents the sum of ranks for positive differences, and $R-$ represents the sum of ranks for negative differences. The n/w/l/t column provides the following information: n is the total number of test functions considered, w is the number of functions where EMOGWO-ADTLF outperformed the compared algorithm, t is the number of functions where both algorithms exhibited equivalent performance, and l is the number of functions where EMOGWO-ADTLF underperformed the compared algorithm.

The results of the test are presented in Table 9. The results reveal that the p-value for the comparison between EMOGWO-ADTLF and MMA is 0.00781, below the significance level of 0.05. This indicates that EMOGWO-ADTLF exhibits a statistically significant performance improvement compared to MMA across the test functions. On the other hand, the p-values for the comparisons with MOGWO, NSGWO, DCMOGWO, MOALO, and MODA are above the significance level of 0.05, suggesting that the differences in performance between EMOGWO-ADTLF and these algorithms are not statistically significant. However, an examination of the n/w/l/t column reveals that EMOGWO-ADTLF outperformed MOGWO in 7 out of 8 functions, NSGWO in 5 out of 8 functions, DCMOGWO in 7 out of 8 functions, MOALO in 6 out of 8 functions, and MODA in 6 out of 8 functions. These results demonstrate that while the differences may not be statistically significant, EMOGWO-ADTLF exhibits superior optimization performance compared to these algorithms in most of the test functions.

Table 9. Wilcoxon Signed-Ranked Test of IGD Values

Algorithms	R+	R-	p-value	n/w/l/t	Significant?
EMOGWO-ADTLF vs MOGWO	30	6	0.1094	8/7/1/0	No
EMOGWO-ADTLF vs NSGWO	26	10	0.3125	8/5/3/0	No
EMOGWO-ADTLF vs DCMOGWO	29	7	0.1484	8/7/1/0	No
EMOGWO-ADTLF vs MMA	36	0	0.00781	8/8/0/0	Yes
EMOGWO-ADTLF vs MOALO	29	7	0.25	8/6/2/0	No
EMOGWO-ADTLF vs MODA	23	13	0.5469	8/6/2/0	No

4.5. Analysis of Algorithms Using Real-World Engineering Problems

The test for diversity, convergence, and coverage of EMOGWO-ADTLF is determined in this section. The IGD and HV values are compared with three well known algorithms in Engineering applications namely MMA, MOALO and MODA. For each engineering problem, the Pareto front is determined by combining the obtained solutions from all algorithms into one dataset and performing non-dominated sorting, using Python package DEAP. Tables 10 and 11 present the IGD and HV analysis for the Welded Beam and Disc Brake Engineering Designs respectively.

For the IGD analysis, EMOGWO-ADLLF dominates in both design problems, obtaining the lowest overall average values. EMOGWO-ADTLF also obtains the best values in three statistical metrics for the HV analysis for both problems. EMOGWO-ADTLF shows high diversity, coverage and convergence for these engineering problems. The results suggest that EMOGWO-ADTLF can maintain a balance between exploration and exploitation in real-world constrained Engineering problems. MMA shows an improvement in its performance in the unconstrained test functions. This indicates that MMA can be useful in engineering applications.

Table 10. IGD Values of Engineering Problems

FUNCT-ION	STATI-STICS	EMOGWO-ADTLF	MMA	MODA	MOALO
Welded Beam Design	AVG	**3.7400E-03**	4.1674E-03	4.0994E-03	3.8535E-03
	MDN	**3.7936E-03**	4.3654E-03	4.2613E-03	3.8507E-03
	SD	1.3111E-04	3.2143E-04	4.4301E-04	7.8066E-04
	BS	**3.5594E-03**	3.7140E-03	3.4943E-03	**2.8988E-03**
	WS	**3.8669E-03**	4.4227E-03	4.5426E-03	4.8110E-03

FUNCT-ION	STATI-STICS	EMOGWO-ADTLF	MMA	MODA	MOALO
Disc Brake Design	AVG	**1.8066E-03**	1.8816E-03	2.0188E-03	1.8899E-03
	MDN	**1.7089E-03**	1.9505E-03	1.9902E-03	1.7166E-03
	SD	1.4200E-04	**1.0507E-04**	1.6469E-04	1.1086E-04
	BS	**1.7034E-03**	1.7331E-03	1.8329E-03	1.7087E-03
	WS	2.0074E-03	**1.9611E-03**	2.1032E-03	2.2445E-03

Table 11. HV Values of Engineering Problems

FUNCT-ION	STATI-STICS	EMOGWO-ADTFL	MMA	MODA	MOALO
Welded Beam Design	AVG	**5.7618E-01**	5.6272E-01	4.6346E-01	5.7011E-01
	MDN	**5.7012E-01**	5.6783E-01	4.6209E-01	5.6510E-01
	SD	4.5864E-02	8.5084E-03	**7.7780E-03**	7.8335E-03
	BS	**6.3514E-01**	5.6960E-01	4.7360E-01	5.8117E-01
	WS	5.2329E-01	5.5073E-01	4.5469E-01	**5.6405E-01**
Disc Brake Design	AVG	**4.1770E+01**	4.1309E+00	3.8351E+01	3.0851E+01
	MDN	**4.1531E+01**	4.1305E+00	3.8949E+01	3.0879E+01
	SD	7.5412E-01	**1.6374E-02**	9.1732E-01	8.2573E+00
	BS	**4.2790E+01**	4.1512E+00	3.9049E+01	4.0950E+01
	WS	4.0990E+01	**4.1111E+00**	3.7055E+01	2.0724E+01

5. CONCLUSION

This study has developed an enhanced MOGWO using adaptive population parameter tuning and levy flight theories. It solves issues in multi-objective optimization including parameter tuning. The analysis of IGD and HV values of EMOGWO-ADTLF across different test functions and engineering design problems shows its dominance over existing nature-inspired algorithms. EMOGWO-ADTLF ranks first in both IGD and HV values when compared to MOGWO, NSGWO, DCMOGWO, MMA, MOALO and MODA. This demonstrates the ability of the proposed algorithm to correctly approximate the Pareto fronts and cover the objective space. This indicates that EMOGWO-ADTLF outperforms all other algorithms in terms of diversity, convergence, and coverage. Its superior diversity demonstrates the algorithm's capability to effectively balance exploration and exploitation.

The work shows the potency of adaptive diversity approaches and Levy flight theories in developing robust algorithms for complex real-world problems. It offers a robust tool for solving complex multi-objective problems with improved parameter tuning. Future Studies should concentrate on the scalability of the MOGWO algorithm.

REFERENCES

[1] Mirjalili S, Saremi S, Mirjalili SM, Coelho LDS. *Multi-objective grey wolf optimizer: A novel algorithm for multi-criterion optimization*. Expert Syst Appl 2016; 47:106–19. https://doi.org/10.1016/j.eswa.2015.10.039.

[2] Yang Y, Yang B, Wang S, Jin T, Li S. *An enhanced multi-objective grey wolf optimizer for service composition in cloud manufacturing*. Applied Soft Computing Journal 2020;87. https://doi.org/10.1016/j.asoc.2019.106003.

[3] Huy THB, Kim D, Vo DN. *Multiobjective Optimal Power Flow Using Multiobjective Search Group Algorithm.* IEEE Access 2022; 10:77837–56. https://doi.org/10.1109/ACCESS.2022.3193371.

[4] Avvari RK, Kumar D M V. *A Novel Hybrid Multi-Objective Evolutionary Algorithm for Optimal Power Flow in Wind, PV, and PEV Systems*. Journal of Operation and Automation in Power Engineering 2023; 11:130–43. https://doi.org/10.22098/JOAPE.2023.10371.1746.

[5] Pandya SB, Jiriwala RJ. *Non Dominated Sorting Dragonfly Algorithm For Multi-Objectives Optimal Power Flow*. 2019 Innovations in Power and Advanced Computing Technologies (i-PACT), 2019. https://doi.org/10.1109/i-PACT44901.2019.8960065.

[6] Kahraman HT, Akbel M, Duman S. *Optimization of Optimal Power Flow Problem Using Multi-Objective Manta Ray Foraging Optimizer*. Appl Soft Comput 2022;116. https://doi.org/10.1016/j.asoc.2021.108334.

[7] Vijaya Bhaskar K, Ramesh S, Karunanithi K, Raja SP. *Multi-Objective Optimal Power Flow Solutions Using Improved Multi-Objective Mayfly Algorithm (IMOMA).* Journal of Circuits, Systems and Computers 2023;32. https://doi.org/10.1142/S0218126623502006.

[8] Linnala M, Hämäläinen J. *Multiobjective optimisation in papermaking applications*. vol. 25. 2016.

[9] Pazhaniraja N, Basheer S, Thirugnanasambandam K, Ramalingam R, Rashid M, Kalaivani J. *Multi-objective Boolean grey wolf optimization based decomposition algorithm for high-frequency and high-utility itemset mining*. AIMS Mathematics 2023; 8:18111–40. https://doi.org/10.3934/math.2023920.

[10] Dilip L, Bhesdadiya R, Trivedi I, Jangir P. *Optimal Power Flow Problem Solution Using Multi-objective Grey Wolf Optimizer Algorithm*. Lecture Notes in Networks and Systems, vol. 19, Springer; 2018, p. 191–201. https://doi.org/10.1007/978-981-10-5523-2_18.

[11] Kamalova A, Navruzov S, Qian D, Lee SG. *Multi-robot exploration based on Multi-Objective Grey Wolf Optimizer.* Applied Sciences (Switzerland) 2019;9. https://doi.org/10.3390/app9142931.

[12] Wang C, Zhang S, Xiao L, Fu T. *Wind speed forecasting based on multi-objective grey wolf optimisation algorithm, weighted information criterion, and wind energy conversion system*: A case study in Eastern China. Energy Convers Manag 2021;243.

https://doi.org/10.1016/j.enconman.2021.114402.

[13] Zhu W, Guo J, Zhao G, Zeng B. *Optimal sizing of an island hybrid microgrid based on improved multi-objective grey wolf optimizer*. Processes 2020; 8:1–24. https://doi.org/10.3390/pr8121581.

[14] Makhadmeh SN, Al-Betar MA, Al-Obeidat F, Alomari OA, Abasi AK, Tubishat M, et al. *A multi-objective grey wolf optimizer for energy planning problem in smart home using renewable energy systems*. Sustainable Operations and Computers 2024; 5:88–101. https://doi.org/10.1016/j.susoc.2024.04.001.

[15] Nuaekaew K, Artrit P, Pholdee N, Bureerat S. *Optimal reactive power dispatch problem using a two-archive multi-objective grey wolf optimizer*. Expert Syst Appl 2017; 87:79–89. https://doi.org/10.1016/j.eswa.2017.06.009.

[16] Safari FM, Etebari F, Chobar AP. *Modeling and Optimization of a Tri-objective Transportation-Location-Routing Problem considering route reliability*: using MOGWO, MOPSO, MOWCA, and NSGA-II. Journal of Optimization in Industrial Engineering 2021; 14:99–114. https://doi.org/10.22094/JOIE.2020.1893849.1730.

[17] Tlili S, Mnasri S, Val T. *An improved multi-objective Grey Wolf Optimizer* 2022. https://doi.org/10.21203/rs.3.rs-2267221/v1.

[18] Dada EG, Joseph SB, Oyewola DO, Fadele AA, Chiroma H, Abdulhamid SM. *Application of Grey Wolf Optimization Algorithm: Recent Trends, Issues, and Possible Horizons*. Gazi University Journal of Science 2022; 35:485–504. https://doi.org/10.35378/gujs.820885.

[19] Zhang X qing, Ming Z feng. *An optimized grey wolf optimizer based on a mutation operator and eliminating-reconstructing mechanism and its application*. Frontiers of Information Technology and Electronic Engineering 2017; 18:1705–19. https://doi.org/10.1631/FITEE.1601555.

[20] Tian X, Hu Q, Liu CA. *An improved Multi-objective Grey Wolf Optimization Algorithm Based on Multiple Strategies.* Proceedings - 2022 International Conference on Computer Engineering and Artificial Intelligence, ICCEAI 2022, Institute of Electrical and Electronics Engineers Inc.; 2022, p. 74–8. https://doi.org/10.1109/ICCEAI55464.2022.00024.

[21] Gu W. *An improved multi-objective grey wolf optimization algorithm with dynamic chaos local search mechanism,* 2020, p. 2020–4. https://doi.org/10.1109/ITAIC49862.2020.9338760.

[22] Guo MW, Wang JS, Zhu LF, Guo SS, Xie W. *An Improved Grey Wolf Optimizer Based on Tracking and Seeking Modes to Solve Function Optimization Problems*. IEEE Access 2020; 8:69861–93. https://doi.org/10.1109/ACCESS.2020.2984321.

[23] Yang Z, Liu C, Qian W. *An improved multi-objective grey wolf optimization algorithm for fuzzy blocking flow shop scheduling problem*. 2017 IEEE 2nd Advanced Information Technology, Electronic and Automation Control Conference (IAEAC), IEEE; 2017, p. 661–7. https://doi.org/10.1109/IAEAC.2017.8054099.

[24] Al-Tashi Q, Abdulkadir SJ, Rais HM, Mirjalili S, Alhussian H, Ragab MG, et al. *Binary Multi-Objective Grey Wolf Optimizer for Feature Selection in Classification*. IEEE Access 2020; 8:106247–63. https://doi.org/10.1109/ACCESS.2020.3000040.

[25] Jangir P, Jangir N. *A new Non-Dominated Sorting Grey Wolf Optimizer (NS-GWO) algorithm: Development and application to solve engineering designs and economic constrained emission dispatch problem with integration of wind power*. Eng Appl Artif Intell 2018;72:449–67. https://doi.org/10.1016/j.engappai.2018.04.018.

[26] Fatima A, Javaid N, Butt AA, Sultana T, Hussain W, Bilal M, et al. *An enhanced multi-objective gray wolf optimization for virtualmachine placement in cloud data centers*. Electronics (Switzerland) 2019;8. https://doi.org/10.3390/electronics8020218.

[27] Jiang K, Ni H, Han R, Wang X. *An improved multi-objective grey wolf optimizer for dependent task scheduling in edge computing*. International Journal of Innovative Computing, Information and Control 2019;15:2289–304. https://doi.org/10.24507/ijicic.15.06.2289.

[28] Ahmadi B, Arias NB, Hoogsteen G, Hurink JL. *Multi-objective Advanced Grey Wolf optimization Framework for Smart Charging Scheduling of EVs in Distribution Grids*. 2022 57th International Universities Power Engineering Conference: Big Data and Smart Grids, UPEC 2022 - Proceedings, Institute of Electrical and Electronics Engineers Inc.; 2022. https://doi.org/10.1109/UPEC55022.2022.9917961.

[29] Yang Z, Liu C. *A hybrid multi-objective gray wolf optimization algorithm for a fuzzy blocking flow shop scheduling problem*. Advances in Mechanical Engineering 2018;10. https://doi.org/10.1177/1687814018765535.

[30] Mirjalili S, Mirjalili SM, Lewis A. *Grey Wolf Optimizer. Advances in Engineering Software* 2014; 69:46–61. https://doi.org/10.1016/j.advengsoft.2013.12.007.

[31] Sudholt D. *The benefits of population diversity in evolutionary algorithms: A survey of rigorous runtime analyses*. Natural Computing Series, Springer; 2020, p. 359–404. https://doi.org/10.1007/978-3-030-29414-4_8.

[32] Chawla M, Duhan M. *Levy Flights in Metaheuristics Optimization Algorithms–A Review*. Applied Artificial Intelligence 2018; 32:802–21. https://doi.org/10.1080/08839514.2018.1508807.

[33] Wu L, Wu J, Wang T. *Enhancing grasshopper optimization algorithm (GOA) with levy flight for engineering applications.* Sci Rep 2023;13. https://doi.org/10.1038/s41598-022-27144-4.

[34] Zhang Q, Zhou A, Zhao S, Suganthan PN, Liu W, Tiwari S. *Multiobjective optimization Test Instances for the CEC 2009 Special Session and Competition*. 2009.

[35] Yang XS. *Multiobjective firefly algorithm for continuous optimization*. Eng Comput 2013;29:175–84. https://doi.org/10.1007/s00366-012-0254-1.

[36] Mirjalili S, Jangir P, Saremi S. *Multi-objective ant lion optimizer: a multi-objective optimization algorithm for solving engineering problems*. Applied Intelligence 2017; 46:79–95. https://doi.org/10.1007/s10489-016-0825-8.

[37] Sierra MR, Coello CAC. *Improving PSO-Based Multi-objective Optimization Using Crowding, Mutation and -Dominance*. Springer-Verlag Berlin Heidelberg 2005; LNCS 3410:505–19.

[38] Zitzler E, Künzli S. *Indicator-Based Selection in Multiobjective Search*. 2004.

[39] Zervoudakis K, Tsafarakis S. *A mayfly optimization algorithm*. Comput Ind Eng 2020;145. https://doi.org/10.1016/j.cie.2020.106559.

[40] Mirjalili S. Dragonfly algorithm*: a new meta-heuristic optimization technique for solving single-objective, discrete, and multi-objective problems*. Neural Comput Appl 2016; 27:1053–73. https://doi.org/10.1007/s00521-015-1920-1.

Received: August 2024, Accepted: November 2024, Published: December 2024
Digital Object Identifier: https://doi.org/10.34302/CJEE/PNLK5679

PULSE, BLOOD OXYGEN AND BODY TEMPERATURE MEASUREMENT SYSTEM WITH INTERNET DATA MONITORING. CONSTRUCTION, INSTALLATION, CONFIGURATION SYSTEM PROGRAMMING

Ioana Laura **ALEXANDRESCU**, Ioan Marius **ALEXANDRESCU**
Technical University of Cluj-Napoca, Romania
ioana.laura.alexandrescu@gmail.com, Ioan.alexandrescu@imtech.utcluj.ro

Keywords: **pulse, blood oxygen level, microcontroller, body temperature, pulse, programming, system installation**

Abstract: *The vision of creating this device was to ease the work of the people who would be responsible for the physical recording of the temperature of the people in an enclosure or a specific space, such as a medical office, for example, the pulse and the amount of oxygen in the blood by replacing the human resource with a device that takes all three with the help of sensors and not only that, it sends the data taken by them to some tables in the related database, after which it creates statistical graphs with them. Pulse, blood oxygen and body temperature measurement system with internet data monitoring has in the component sensors MLX90614 for remote body temperature recording, sensor that was connected to ESP32 microcontroller, using I2C communication protocol and MAX30100, which we used to measure pulse and blood oxygen level (SpO2), being connected to another microcontroller, Arduino Uno, also via I2C. What has been measured is displayed on an LCD2004, and the data is transmitted wireless to the local server, in the database created in MySQL.*

1. INTRODUCTION

The solution to help restore day-to-day peace or confidence that we are safe is more thorough monitoring of the health of vulnerable people and more, with constant access to recorded data via the Internet. To put the solution into practice, we created a system to monitor vital functions, such as pulse and blood oxygen level (SpO_2), but also body temperature, with the help of two sensors and other components presented in the paper.

The components needed to make this Pulse, blood oxygen and body temperature measurement system with internet data monitoring are: ESP32, Arduino Uno, Pulse and SpO_2 Sensor, Temperature Sensor, LCD Display 2004, Voltage Level Regulator, Arduino IDE.

2. COMPONENTS USED, CONSTRUCTION AND OPERATION

We used two microcontrollers (ESP32 and Arduino Uno), 3 sensors (MLX90614 for temperature, GY MAX30100 and RCWL 0530 for pulse and oximeter), an LCD display, an I2C interface module and a logic level converter, as well as software, through which the programming of the components, the connections both serial and wireless, the database and tables in it were made.

In the block diagram below, you can see the block diagram of the system (*Fig.1*).

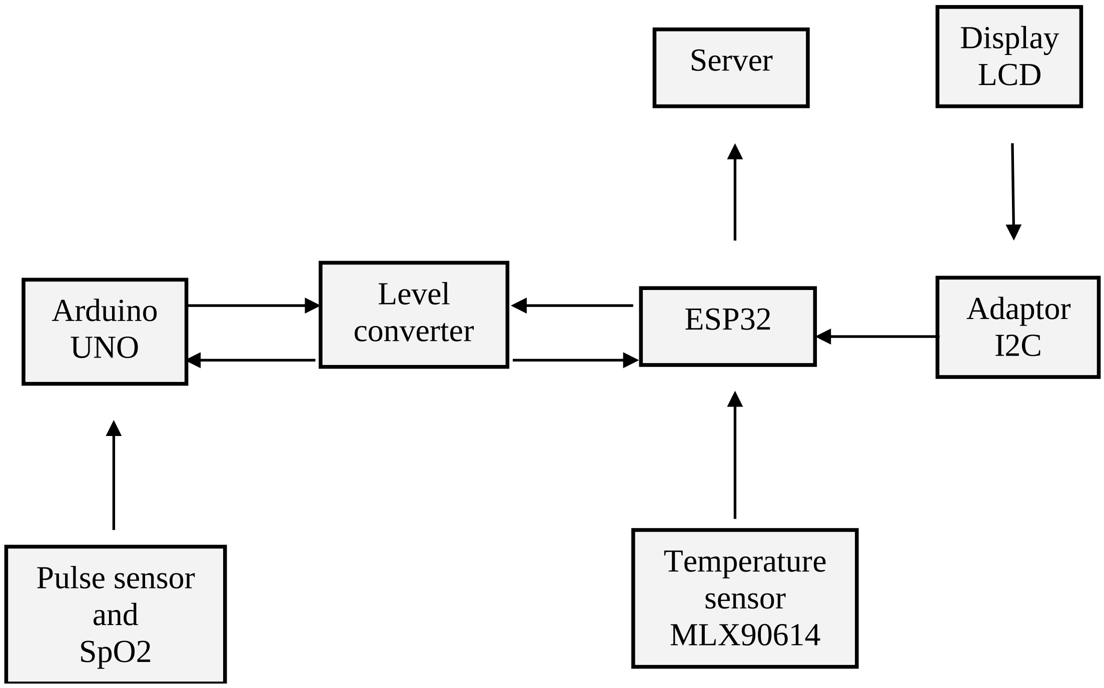

Fig.1 The block diagram

2.1. The ESP32 development board

The ESP32 development board is a microcontroller, system-on-a-chip (SoC) manufactured by Espressif Systems, with an Xtensa LX6 architecture (*Fig. 2*). It is increasingly used in various systems and its popularity has increased in recent years due to its low price, generous capacity, small size, integrating Wi-Fi and Bluetooth (higher versions) wireless communication interfaces. I would call this microcontroller the "brain" of the project because it manages the data received by the sensors, as well as sending them to the database tables, also controlled by the ESP32 board.

2.2. Arduino Uno development board

The Arduino Uno is a microcontroller that uses the ATmega328P microchip and was developed by AVR Arduino.cc. The year of appearance was 2010. The board is equipped with sets of input/output (I/O) pins, digital and analog channels, which can be interfaced with various expansion boards (shields) and other circuits (*Fig.3*).

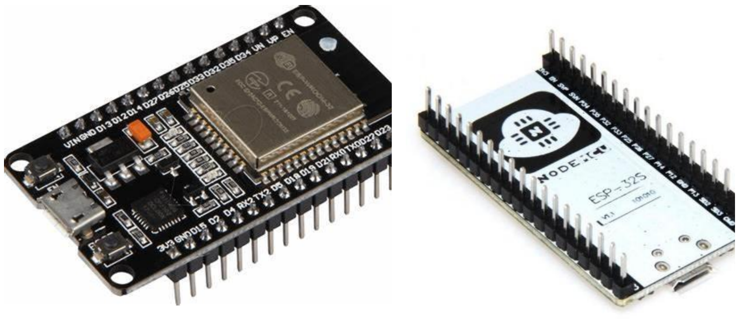

Fig.2 ESP2 microcontroller

Fig. 3 Arduino Uno

2.3. The MLX90614 sensor

The MLX90614 is an infrared thermometer module used to measure temperature without direct contact with the skin. The temperature resolution is approximately 0.02°C (Fig.4). It is configured with 10-bit PWM, which will transmit a temperature rate continuously in the range of -20 - +120°C with increased resolution. The angle from which the measurement perspective is most accurate is 90° at a distance of 1cm.

Fig. 4 MLX90614 Infrared Temperature Sensor

2.4. TheMAX30100 sensor

The MAX30100 optical sensor is intended to monitor heart rate and record blood oxygen (SpO2). Its composition includes: the photodetector, LEDs and optical elements. In order not to be affected by ambient light, the sensor features low-noise electronics (*Fig. 5*).

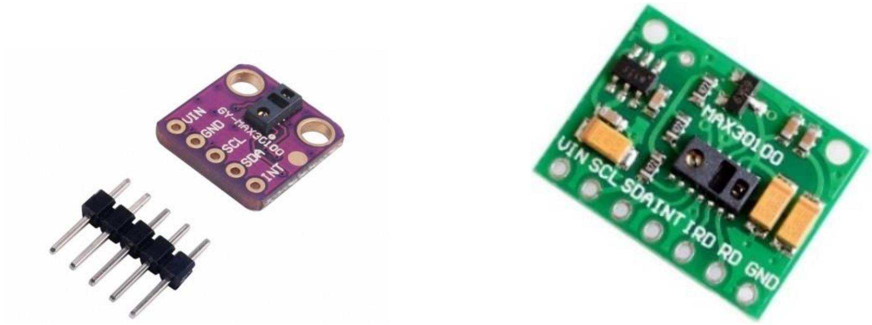

(a) *(b)*

Fig. 5 MAX30100: a-GY MAX30100;b-RCWL 0530

2.5. Display LCD 20-04

This alphanumeric LCD display is used to display symbols, letters and numbers in a total of 80 characters, which can be divided into 4 lines (20 characters/line) (*Fig.6*). It features an HD44780 chip and has a working voltage of 5V. The command can be done in parallel on 4 or 8 bits or through I2C communication, for which I also used an I2C adapter module (for 16x2 or 20x4 LCDs). Also, the display can be placed in less lit areas, the screen having an adjustable brightness by means of a potentiometer also present on the I2C adapter.

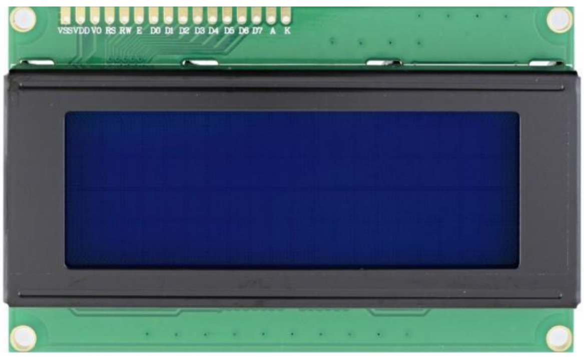

Fig. 6 LCD display

2.6. I2C adapter for LCD

We used this I2C adapter module to reduce the number of pins used by the 20x4 (originally parallel) LCD display on the ESP32, the development board used for the project.

The module attaches directly to the screen, and after that, the only wires we need are SCL and SDA – the clock and data signals, specific to I2C communication. The adapter also features a potentiometer that can be used to adjust the backlight intensity and contrast on the LCD screen (*Fig.7*).

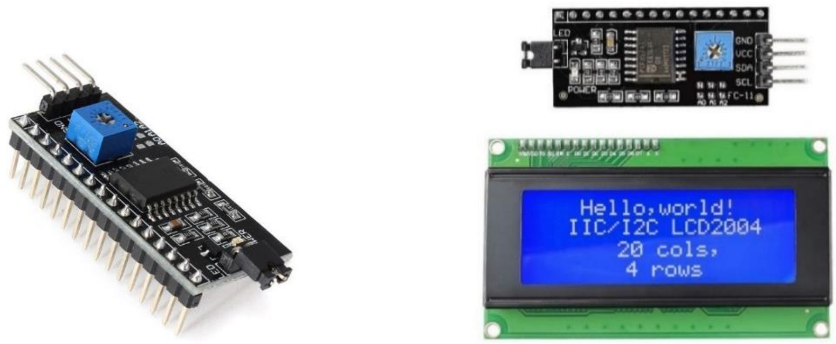

Fig. 7 I2C adapter module

2.7. Logic level converter (level shifter)

The logic level translator module connects components or devices that use different voltages, such as 1.8V, 2.5V, 3.3V or 5V, adjusting the voltage and bringing it to the same level so that they can work together. If we try to make a system with two or more devices that communicate on other voltage levels, such as between development boards, sensors, microcontrollers, other modules, for example Wi-Fi or Bluetooth, this level shifter solves the voltage differences that arise (*Fig.8*).

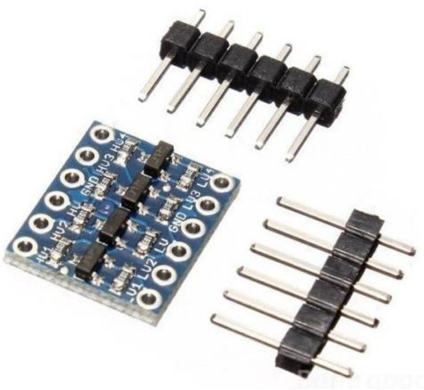

Fig. 8 Logic level converter

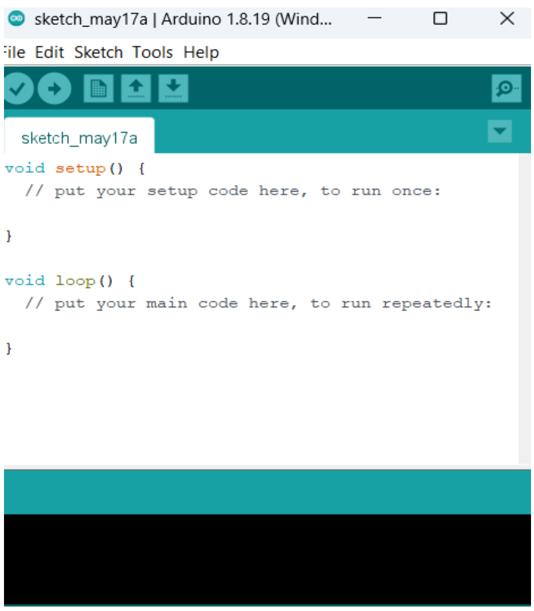

Fig. 9 New Arduino Sketch

2.8. Arduino IDE

Arduino Integrated Development Environment - or Arduino Software (IDE) - is the environment in which the programming of the components and the communication between them was carried out. Uploading programs to the Arduino and ESP32 boards was done via appropriate USB cables. Arduino uses a variant of the C++ programming language. Other methods and special functions from other files have been added to it to make the program easier to use for more users.

2.9. XAMPP, MySQL and phpMyAdmin

XAMPP is a free package and an easily accessible and modifiable web server platform developed by Apache Friends, which mainly contains the Apache HTTP server, the MariaDB database, and readers for script files written in the PHP and Perl programming languages. To run any PHP program, I needed Apache or MYSQL databases, both of which are supported by XAMPP. MySQL is a database management system. I also needed the free phpMyAdmin software tool, also described in the PHP language, intended to deal with the administration of the database created in MySQL online.

2.10 Measurement of blood oxygen level and pulse measurement

When a person touches a pulse oximeter, light from the device passes through the blood in the fingers. The amount of oxygen is calculated analogically according to changes in light absorption from both oxygenated, inspired blood and deoxygenated, expired blood (*Fig.10*). The MAX30100 sensor consists of two LEDs (red and IR) and a photodiode. Both LEDs are used to measure SpO_2. They emit light at different wavelengths, ~640nm for the red LED and ~940nm for the IR LED. At these wavelengths, oxygenated and deoxygenated hemoglobin have very different absorption properties. Oxygenated hemoglobin absorbs more infrared light and reflects red light, while deoxygenated hemoglobin absorbs more red light and reflects infrared light. The reflected light is measured by the photodetector. The MAX30100 sensor reads these different absorption levels to find the blood oxygen concentration (SPO_2). The ratio of IR to red light received by the photodetector gives us the oxygen concentration in the blood. Only the IR LED is needed to measure the heart rate. The heart rate is the ratio of time between two consecutive beats. The altered capillary tissue volume affects the sensor's infrared light, which transmits particles after each heartbeat. In other words, when a finger is placed in front of this sensor, the reflection of the infrared light is changed according to the volume change of the blood inside the capillary vessels.

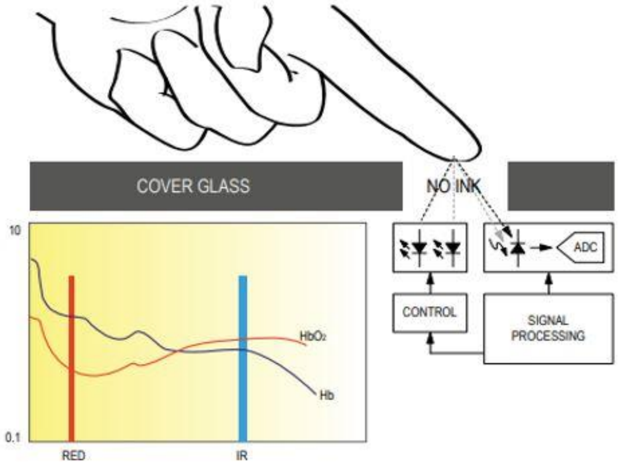

Fig.10 SpO$_2$ measurement

3. INSTALLATION OF THE SYSTEM

3.1. Installing ESP board package in Arduino IDE

To start testing the functionality of the components one by one, and then them programming, we first needed to be able to choose the ESP32 microcontroller from the top left menu bar of the Arduino IDE interface, from the "Tools" - "Board" button.

Step 1: File> Preferences

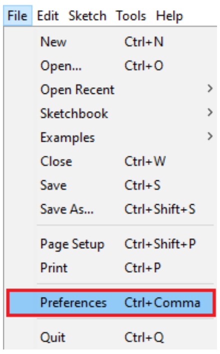

Fig. 11 Installing ESP32 in Arduino IDE step 1

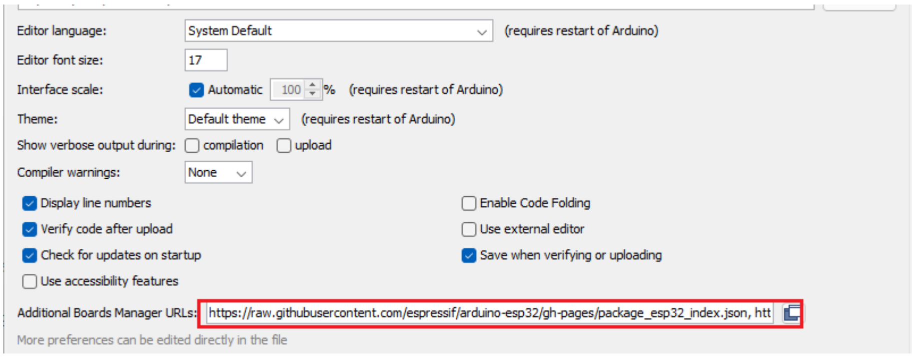

Fig. 12 Installing ESP32 in Arduino IDE step 2

Step 2: We inserted the ESP package link from github in the field shown in *Fig. 12*

Step 3: Tools> Board> Boards Manager

Step 4: We typed in the corresponding field "ESP32", and after the search engine found the package "esp32 by Espressif Systems", we pressed "Install", as can also be observed in *Fig. 14*

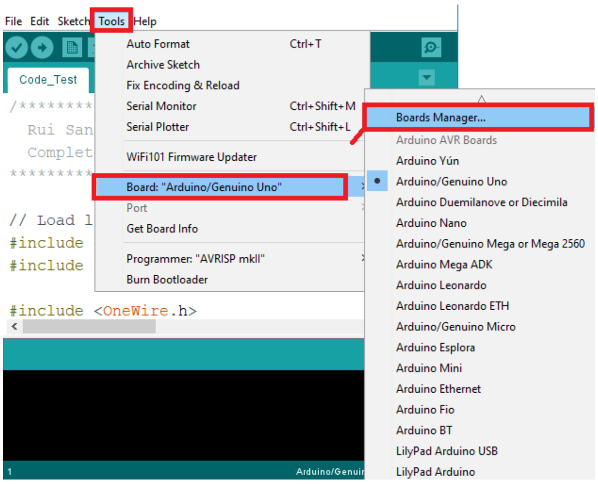

Fig. 13 Installing ESP32 in Arduino IDE step 3

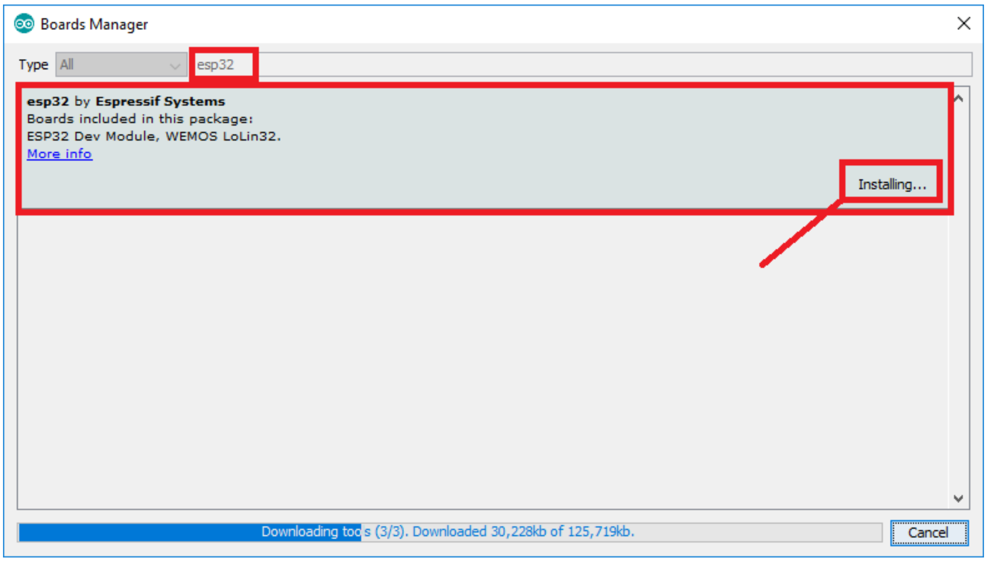

Fig. 14 Installing ESP32 in Arduino IDE step 4

Step 5: Choose the right board and start programming

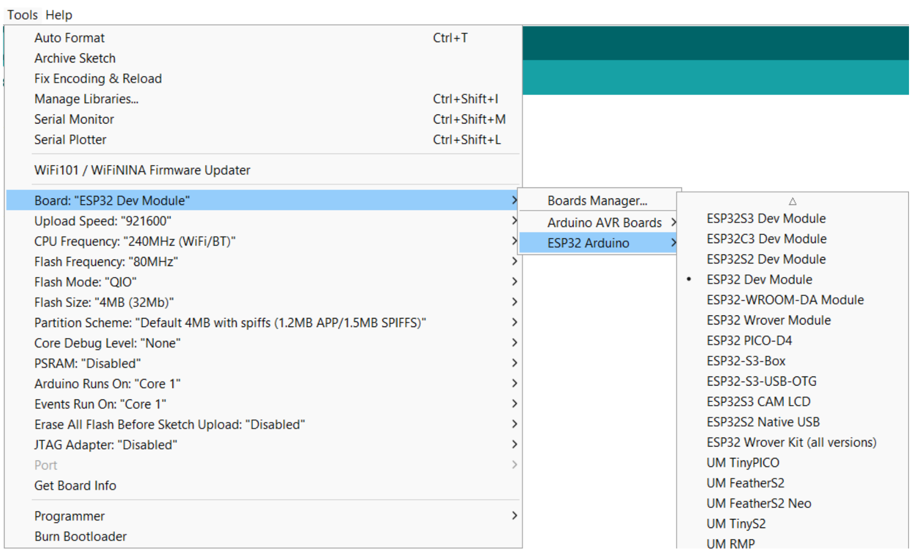

Fig. 15 Installing ESP32 in Arduino IDE step 5

3.2. ESP32 and Arduino Uno Programming

3.2.1 LCD + Adaptor I2C with ESP32

To facilitate the use of the display, which initially uses 16 pins, we opted for the purchase of a special I2C adapter module for this type of display. The LCD component used in the project was the one with 20 characters arranged on 4 lines. Using the module, we reduce the number of pins to 4 and now the display will use I2C communication with the ESP32 board, through the data and clock pins, SDA and SCL, plus the power, Vcc and GND pins. The adapter was soldered to the LCD by tinning in the faculty lab as seen in *Fig. 16*.

Fig. 16 Tinning the I2C adapter to the LCD display

Next came testing them by compiling and deploying a simple program on the ESP32 (*Fig.17*).

Fig. 17 Testing the display with ESP32 via I2C

3.2.2 MLX90614 temperature sensor with ESP32

Next, we connected the MLX90614 temperature sensor to the ESP32. The first time to be able to compile the program, we needed the library belonging to the sensor where the libraries, special functions, definition of registers, pins, and other predefined elements are located (*Fig.18*, *Fig.19*).

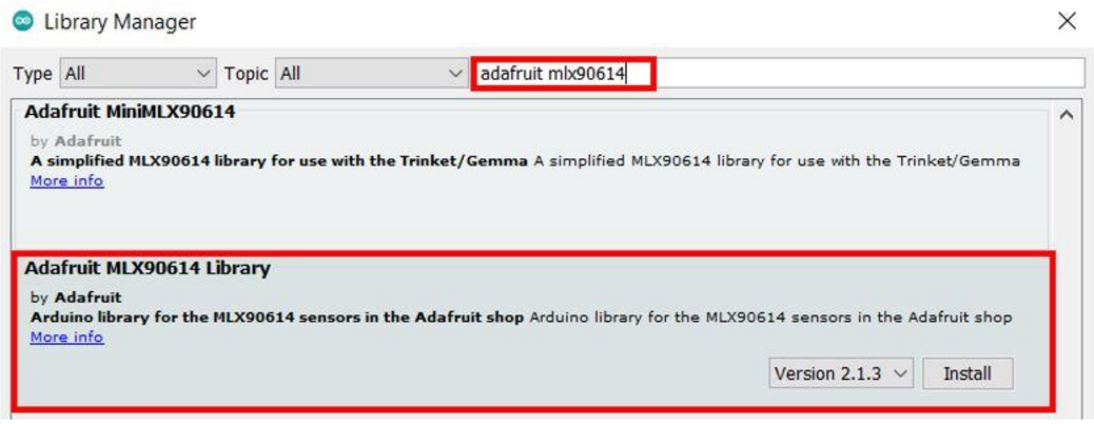

Fig. 18 Installing the MLX90614 Sensor Libraries

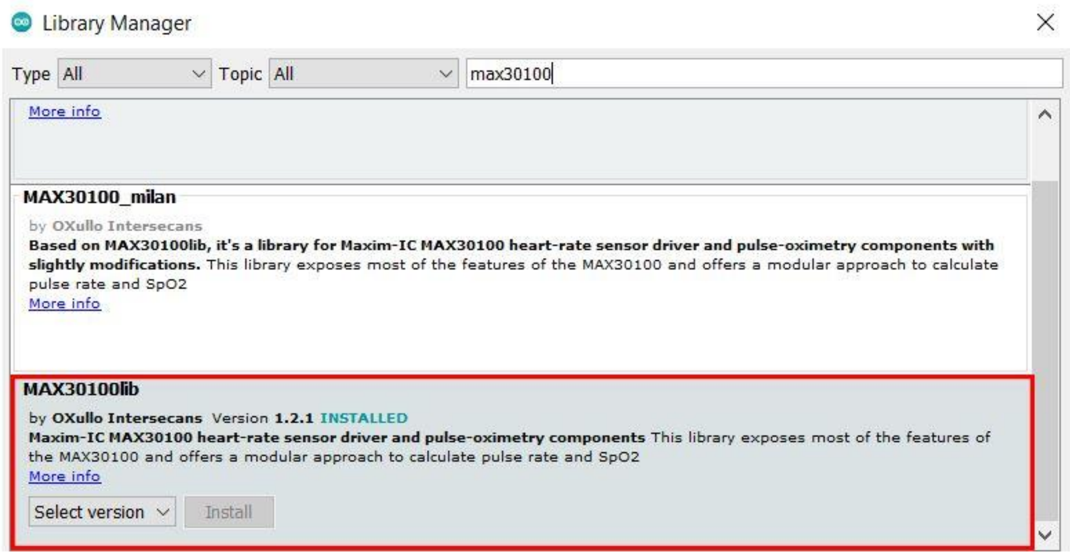

Fig. 19 Installing the MAX30100 Sensor Libraries

4. SYSTEM PROGRAMMING

The serial baud rate was set to 9600 in the setup() function. Then, also in this function, we initialized the temperature (mlx) measured by the sensor through the begin() method, describing the sequence according to the serial connection: as long as it does not exist and if the sensor is not properly connected, the serial monitor will notify us with an error message, and as long as the statement is true the program will wait.

```
    while (!Serial);

    if (!mlx.begin()) {
        Serial.println("Eroare la conectarea senzorului MLX. Verificați firele.");
        while (1);
    };
```

In the loop() function we started the description of the temperature measurement logic. Thus, we defined a variable of type double to save the data retrieved by the sensor through the function readObjectTempC() in degrees Celsius. If the body temperature is greater than 36°C and less than 37.4°C, with a margin of error of about 0.2°C, then the temperature is optimal, a message displayed on both the serial monitor and the LCD screen.

```
double currTemp = mlx.readObjectTempC();
if (currTemp>36) {
    Serial.print("Temperatura = ");
    Serial.print(currTemp);
    Serial.println("°C");
    if (currTemp>36 && currTemp<37.4) {
        Serial.println("Temp optima");
         delay(2000);
        lcd.setCursor(1,0);
        lcd.print(currTemp);
        lcd.setCursor(1,1);
        lcd.print("Temp optima");
```

If the temperature is higher than 37.4°C and lower than 42-43°C, then the displayed message will be the one corresponding to the increased temperature.

```
    } else if (currTemp>37.4 && currTemp<43) {
        Serial.println("Temp crescuta");
         delay(2000);
        lcd.setCursor(1,0);
        lcd.print(currTemp);
        lcd.setCursor(1,1);
        lcd.print("Temp crescuta");
    }
```

If the retrieved temperature is abnormal, lower than 36°C and higher than 43°C, then the displayed message will be an error message and will instruct the person to take another measurement.

```
else if (currTemp<36 || currTemp>43) {
  Serial.println ("Temparatura incorecta. Reincercati.");
```

In the code described for the MAX30100 sensor we did the same for the temperature sensor. For the first time, we have included in the program the libraries where the functions, filters, registers and methods used in measuring pulse and blood oxygen level are defined.

```
#include <MAX30100.h>
#include <MAX30100_BeatDetector.h>
#include <MAX30100_Filters.h>
#include <MAX30100_PulseOximeter.h>
#include <MAX30100_Registers.h>
#include <MAX30100_SpO2Calculator.h>
```

We have defined the object that will call both the pulse function and the SpO2 function. Next, we used a void routine that will be automatically called by the program every time the sensor senses a pulse, and will show us on the serial monitor that it has sensed activity.

```
      PulseOximeter pox;
void onBeatDetected() {
    Serial.println("♥ Beat!");
}
```

In the setup() function we specified as with the previous sensor, if the call to the MAX30100 sensor does not occur properly or does not occur at all, the message displayed by the serial monitor will be an error message and will not proceed further. Otherwise, it will tell us that the sensor initialization was successful.

```
if (!pox.begin()) {
    Serial.println("FAILED");
    for(;;);
} else {
    Serial.println("SUCCESS");
}
```

In the loop() function we specify if the time set since the last measurement has passed and we will start taking the information from the sensor one by one, displaying it on the serial monitor. The initial "pulseOk" and "spo2Ok" state variables will be initialized to 0.

```
if (millis() - tsLastReport > REPORTING_PERIOD_MS) {
    int pulseOk = 0;
    int spo2Ok = 0;
    Serial.print("Puls:");
    Serial.print(pox.getHeartRate());
    Serial.println("bpm");
    Serial.print("SpO2:");
    Serial.print(pox.getSpO2());
    Serial.println("%");
```

For the pulse, we compared the recorded values with the normal range of the human pulse (50, 130). We have divided this range into 3 parts to interpret it: (50, 60), (60, 100) and (100, 130). If the pulse value is between 50 and 60 bpm, the pulse will be low. If it is between 60 and 100, the pulse will be normal. If it is between 100 and 130 the pulse will be high. Finally, after the pulse has been properly measured, the variable "pulseOk" is updated to 1.

```
if (pox.getHeartRate() > 50 && pox.getHeartRate() < 130) {
    if (pox.getHeartRate() < 60) {
        Serial.println("Puls scazut");
    } else if (pox.getHeartRate() < 100) {
        Serial.println("Puls normal");
    } else if (pox.getHeartRate() < 130) {
        Serial.println("Puls ridicat");
    }

    pulseOk = 1;
```

Likewise, for the oxygen level. The recording range was set between the percentages 78% and 101%. If the oxygen level is less than 90%, the SpO_2 will be low. Otherwise, if it is in the range (90, 101), SpO_2 is normal/good. Finally, the variable "spo2Ok" is updated to 1.

```
if (pox.getSpO2() > 75 && pox.getSpO2() < 101) {
    if (pox.getSpO2() < 90) {
        Serial.println("SpO2 scazut");

    } else {
        Serial.println("SpO2 normal");
    }

    spo2Ok = 1;
}
```

After recording the two quantities, the time since the last data acquisition by the sensor is updated with the time since the program started running to make the loop again wait until the next measurement.

```
tsLastReport = millis();
```

If what the sensor recorded is not within the normal measurement parameters, the serial monitor will show us a message specifying the information and suggesting that we try another measurement.

```
} else {
  Serial.println ("SpO2 sau Puls incorect. Reincercati.");
  Serial.println("----------------------------------------
}
```

The pulse sensor ended up being connected to the Arduino Uno as we said above, and the code and data interpretation logic remained the same, depending on the normal parameters set. For the code run by the ESP32 I needed some additional logic in addition to the temperature sensor, as the board also takes in the data recorded by the pulse and oxygen sensors on the Arduino.

As the Arduino and the ESP communicate with each other serially via UART, in the software communication chapter we needed a condition that would change every time the data was successfully retrieved by the ESP from the Arduino. The first time I determined with two variables whether the pulse and the blood oxygen level were correctly recorded in the code of the Arduino board, and if so: I printed on the serial monitor a string of characters: "hrd_", with another character between the two measurements "_", which marks the difference between the two retrieved data, one for pulse and one for oxygen. The following sequence appears on the serial monitor: "hrd_puls_oxygen". After an appropriate measurement, the condition changes to signal this.

```
if (pulseOk && spo2Ok) {
    //Serial.println("Heart read done");
    Serial.print("hrd_");
    Serial.print(pox.getHeartRate());
    Serial.print("_");
    Serial.println(pox.getSpO2());
    cond = 0;
```

For the code on the ESP32, which is also the microcontroller that controls all the data recorded by the sensors, I needed a String variable to read the information from the serial monitor of the Arduino Uno microcontroller (Serial2). After reading what is written on Serial2, to later operate with them, I had to differentiate between the two measurements: pulse and oxygen, because they came on a single line in the form "hrd_puls_oxygen". Through two integer variables "_index" and "_index2", we recorded the position of the first character "_" in the string and the position of the second character "_", respectively. Why do we care about this? Because what is written after the first "_" is the measurement for pulse, which we are interested in, and what is after the second "_" is the measurement for SpO2.

Thus we started to read and record in two distinct variables of type String x and y, the values of the divided string: in x - what is between the two "_" in the big string (measurements corresponding to the pulse) and in y - what is between the the second ”_” and the end of the whole string (measurements corresponding to blood oxygen). After the proper recording of pulse and SpO2 data by the ESP32 has occurred, the condition changes to signal the success of the operations and to move on in the code to the temperature measurement by the sensor connected to the ESP32 itself.

```
while (!cond) {
    String s2ln = Serial2.readStringUntil('\n');
    int _index=s2ln.indexOf('_');
    if(_index==-1)
    {
      Serial.println(s2ln);
    } else
    {
      int _index2=s2ln.indexOf('_', _index+1);
      String x = s2ln.substring(_index + 1, _index2);
      String y = s2ln.substring(_index2 + 1, s2ln.length() - 1);
      cond = 1;
```

The imposed condition works like a switch. While a measurement is being recorded on one of the boards, the other sensor waits until the current one records a correct measurement, then tells it when it's done and can record the second sensor, and vice versa. The display on the LCD of the measurements for temperature, pulse and oxygen takes place after all the data has been received by the ESP, and will present the information to the users with the strict interpretation:

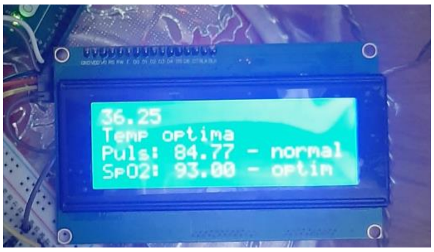

Fig. 20 LCD display of measurements

5. CONCLUSIONS

- The system was designed as a device that measures vital functions and records the data in a table in a database, it works, it uses simple, relatively cheap components, it corresponds to the original idea, the system can be easily used by anyone;
- The system can be used at home by people who want to record data about body temperature, heart rate and blood oxygen concentration, information needed by people at risk, sick or simply curious;
- The system can be used in hospitals, offices or any institutions that want to monitor people entering the premises, to be able to make statistics or to take measures to keep the area safe;
- It has applicability in checking athletes, such as swimmers, people who practice athletics or contact sports, to determine whether they are fit to start training, both in adults and children;
- You can sort the data recorded in the database table by size, or by type, to create advanced statistics in specialized applications.
- For a more accurate measurement and a low margin of error, high quality or more sensitive sensors can be used;
- An application can be created for the phone to be able to access the data from the sensors at any time;
- Power sources can be replaced by batteries or other individual sources.

REFERENCES

[1] S. Oniga, *Microprocesoare şi microcontrolere, note curs*, http://ece.ubm.ro/cursuri/.

[2] M. Margolis, B. Jepson, N. R. Weldin, *Arduino Cookbook*, 3rd Edition, O`Reilly, 2020.

[3] https://microcontrollerslab.com/mlx90614-non-contact-infrared-temperature-sensor-esp32/

[4] https://microcontrollerslab.com/max30100-pulse-oximeter-heart-rate-sensor-esp32/

[5] A. James, *Arduino: The complete guide to Arduino for beginners, including projects, tips, tricks, and programming!*, Ingram Publishing Ltd., 2019.

[6] http://www.esp32learning.com/code/esp32-and-max30100-heart-rate-monitor-sensor.php

[7] E. Lupu, Annamaria Mesaros, A. Suciu, *Microprocessors - Architectures and Applications*, Risoprint Cluj-Napoca, 2003.

Received: June 2024, Accepted: December 2024, Published: December 2024
Digital Object Identifier: https://doi.org/10.34302/CJEE/SQTJ4961

VOLTAGE PROFILE IMPROVEMENT WITH APPLICATION OF DIFFERENTLY OPTIMIZED FACTS CONTROLLERS

Joel R. **SUTTER**, John N. **NDERU** and Ariel M. **MUTEGI**
The School of Electrical, Electronic and Information Engineering (SEEIE), Jomo Kenyatta University of Agriculture and Technology, Nairobi, Kenya
joelruttosutter@gmail.com, adjainderugac@gmail.com, arielmutegi@yahoo.com

Keywords: Algorithm, FACTS, voltage profiles, tuning, constrained optimal power flow, power system parameters, power transients, real and reactive power control

Abstract*: This research work presents a novel individual and Hybrid MGA and IGWO was utilized to develop FACTS-controlled optimization model for improvement of bus voltage profiles. The algorithm simultaneously solved the objective problem and augments device parameters as it searches for the best FACTS location and sizes. Objective function was resolved Security Constrained Optimal Load Flow (SCOLF) with the integration FACTS power electronics controllers for TTC without violating active and reactive power generation confines, voltage boundaries, line flow limits, and FACTS devices operation restrictions and ratings. TCSC controller parameters have been effectively optimized for the research and the work has been successfully carried out on MATLAB platform using IEEE 30-bus test bus systems. Power system procedures and parameters can be augmented using artificial intelligence techniques like ANN, ANFIS, Fuzzy Logic, DEPSO and MGA together with power electronics built versatile and highly adaptable Flexible AC Transmission Systems controllers. FACTS normalize voltage or control the power that is either added into or absorbed from the system. They enhance the overall grid capacity and performance. They also increase the dependability and efficiency of power systems. Apart from alleviating power transients, FACTS provide greater system real and reactive control.*

1. INTRODUCTION

Currently, electrical energy utilities run on constraints of complex interconnectivity and operation limits therefore forcing them to operate within their existing infrastructure at a higher effectiveness. There is an ever growing interest in better operation and usage of the prevailing electricity infrastructure to enable the effective control of load flow, advance network dynamics, and upsurge system dependability by use of these devices. In addition, the devices can also play a pivotal role in augmentation of power grid transmission capability [1]. Extensive variety of algorithms have been advanced for computing TTC, increasing voltage profiles, optimizing via minimization the generation costs and loss lessening. Optimization of network parameters can be executed by methods including but not limited to SQP, DEA, DEPSO, MGA, BGA, ABCA, PSO and transfer based TSCOPF techniques. These ways necessitate the formulation of an objective function for the to get the optimal solution. [2]. Under constantly increased electricity demands, it is becoming more critical to boost the system capability such that more power transfers, maintenance of voltage stability margins and losses are minimized with less network expansion investment. In the place of building new supply substations or lines, proper installation and optimization, with Artificial Intelligence (AI), of transmission as well as generation units can make power networks billet more from source end to load [3]. With application of these optimized devices, the electrical energy can be transmitted over the selected paths with considerable increase in transmission line capability and additionally enhancement for the security of interconnected power network. UPFC, for example, is very adaptable and versatile amongst the FACTS controllers [4]. Augmentation of total transfer capability, optimization via minimization of power losses and enhancement of voltage profiles in strained and overloaded transmission network guarantees that the system is steady and effectual even under stressed circumstances. AI methods can be suitably applied to determine the optimum ratings and values of these devices for simultaneous resolution of diverse power grid problems.

2. CONTEXT

Placement of FACTS is achievable and optimization is critical in realization of the device ultimate capability. In early days, stabilization of electrical grids was realized via equipment like PSS, AVRs and approaches like breaking resistor, discounting of system transmission reactance, use of grouped or bundled conductors, SCC limiters and the most lately placement of FACTS devices. These devices have the capability to alter the three main control parameters, i.e. the bus voltage, reactance of the transmission line, and phase angle between two buses, either concurrently or autonomously. They achieve this via the regulatory control of the in-phase voltage, voltage of the quadrature axis and parallel compensation to better voltage stability, power transmission and shrink system losses of the composite interconnected power grid. To harness the several benefits of these devices, AI techniques can be used to augment the parameters. This way, FACTS devices optimization models for objective functions of more than parameter. This is critical since the devices are very expensive and comparative analysis is required for commercial reasons [4]. Heuristic search methods have been found to be robust and efficient to solve such complex problems and give fairly optimal results. The IGWO augmentation algorithm applied in this work, is susceptible to premature fall into the local optimum and its convergence speeds are quite low. Consequently, so as to increase the global convergence and equivalent speed, this research has utilized MGA to mitigate this phenomenon. IGWO's searching ability is based on two principles: survey and exploitation. Survey refers to the process of exploring new areas or mathematically, the process of looking for a solution as much as possible in a search space to prevent local optimum stagnation. On the other hand, exploitation refers to looking in the same direction in greater depth or mathematically, searching for a solution with high precision. Using the IGWO algorithm to find the global optimum with high efficiency necessitates achieving the proper balance between exploration and exploitation. As compared to other swarm intelligent techniques, IGWO algorithms perform well in finding the global optimum for the high-dimensional problem, but not so well in finding the global optimum for low-dimensional problems. Usually, there is no guarantee that IGWO will identify global minima, it is conceivable that it will stick with local minima and calculate corresponding angles that do not eliminate the third harmonic. To mitigate this issue, a donor vector from MGA technique is used, which adds randomness to the IGWO technique and allows it to escape out of the local optimum and look in a new direction for the global optimum. Since the MGA technique is based on accomplish random initialization, it outdoes finding the global optima, but it has a limitation in that it lacks a parameter that is directly related to algorithm convergence, so the speed of convergence is very slow and provides power oscillation around the global optima. As a result, the flaw in one approach is offset by another method. Therefore, a new algorithm called improved gray wolf optimization and Modified Genetic Algorithm (IGWO-MGA) is proposed in this thesis, which combines the IGWO algorithm with a better convergence factor and the MGA algorithm with a dynamic scaling factor with the help of a MGA crossover operator [5][7][11].

3. PREVIOUS RESULTS

From the previous literature studies, optimum placement various FACTS devices have been research with mainly singular heuristic methods. To realize the peak performances of these devices; the best location, hybrid AI methods need to be introduced and their performances assessed with single ones. The assessment has also deduced that the devices have been utilized jointly and separately to offer voltage over active and real power control and regulation via the voltage injection and absorption properties they possess. The controllers have used to enhance one or two parameters like voltage stability, loss reduction or transient stability and other system parameters. This research has gone a step further. It will further delve into the development of hybrid GA-IGWO FACTS-controlled model for optimization of total capability transfer and observation of voltage profile enhancement and loss reduction. The unique FACTS controlled AI optimization model for TTC enhancement crucial for comparative analysis, system performance and economic reasons. Performances of single AI models also need be compared with the hybrid ones for both optimization of the system parameter as well FACTS devices allocation. Hybrid evolutionary heuristics with different strengths are also presented in this work. This work will create a basis of evaluating their optimization capabilities with other techniques in the foreseeable future.

4. METHOD USED

4.1. Problem formulation

The problem will be formulated to form the maximization the viable TTC while making observation on voltage profiles and system loss reduction. The optimization problem can be augmented instantaneously subject to the numerous equality and inequality limitations. The objectives maximizing TTC and observation of profiles of bus voltages and power loss lessening characteristics. The formulation covered the TTC base case (without FACTS controllers), TTC with UPFC and TTC with TCSC. TTC is the utmost power transfer without any line thermal overload, within violation of voltage bounds voltage unsteadiness or transient probations. It’s the central constituent of the ATC. Its dependent on system base case operating conditions, system operating limits, configuration of the system network, network contingencies among other constraints. TTC can be accomplished using Repeated Power Flow, Continuation Load Flow and Security Constrained Load Flow. The Security Constrained Power Flow has been utilized for this study [5]-[12].

4.2. Base case CPF (without FACTS controllers)

To find TTC, the objective is to optimize through maximization strategy the power transfer between two areas while operating within thermal, voltage and stability confines. A typical TTC problem formulation is presented as illustrated in the following equation:

$$P_r = \sum_{k=1}^{MB_{SNK}} P_{Di} \tag{1}$$

The above is subject to: -

$$P_{Gi} - P_{Di} + V_i V_j V_{ij} \cos\left(\theta_{ij} + \delta_i - \delta_j\right) = 0 \tag{2}$$

$$Q_{Gi} - Q_{Di} + V_i V_j Y_{ij} \sin\left(\theta_{ij} - \delta_i + \delta_j\right) = 0 \tag{3}$$

$$P_{Gi}^{min} \leq P_{Gi} \leq P_{Gi}^{max} \tag{4}$$

$$Q_{Gi}^{min} \leq Q_{Gi} \leq Q_{Gi}^{max} \tag{5}$$

$$S_{ij} \leq S_{ij.max} \tag{6}$$

$$V_i^{min} \leq V_i \leq V_i^{max} \tag{7}$$

where: MB_{SNK} is the number of load buses in the receive end and P_{Di} is the real load at bus i.

The other equations are the power flow restraints and the following equations denote active and reactive power generation bounds, the second last equation stands for the thermal limitations and the last equation denotes the voltage level constraint.

4.3. CPF with TCSC FACTS Controller

The modified TTC function with TCSC FACTS controller, P_r for maximizing the TTC [44] of power transactions between source and sink areas in power system is given as:

$$P_r = \sum_{k=1}^{MB} P_{Di} \tag{8}$$

The equality constraints with TCSC controller are formulated as follows:

$$P_{Gi} - P_{Di} + \sum_{k=1}^{m} P_{Pi}\,(\alpha_{Pk}) + V_j Y_{ij}(X_S)\,cos\big(\theta_{ij}\,(X_s) - \delta_j + \delta_j\big) = 0 \tag{9}$$

$$Q_{Gi} - Q_{Di} + \sum_{k=1}^{m} P_{Pi}\,(\alpha_{Pk}) + V_j Y_{ij}(X_S)\,sin\big(\theta_{ij}\,(X_s) - \delta_j + \delta_j\big) = 0 \tag{10}$$

Given that:

$$P_{Gi}^{min} \leq P_{Gi} \leq P_{Gi}^{max} \tag{11}$$

$$Q_{Gi}^{min} \leq Q_{Gi} \leq Q_{Gi}^{max} \tag{12}$$

$$V_i^{min} \leq V_i \leq V_i^{max} \tag{13}$$

$$T_i^{min} \leq T_i \leq T_i^{max} \tag{14}$$

$$0 \leq X_{si} \leq X_{si}^{max} \tag{15}$$

$$\alpha_{Pi}^{min} \leq \alpha_{Pi} \leq \alpha_{Pi}^{max} \tag{16}$$

$$0 \leq V_{Ui} \leq V_{Ui}^{max} \tag{17}$$

$$-\pi \leq \alpha_{Ui} \leq \pi \tag{18}$$

$$Q_{vi}^{min} \leq Q_{vi} \leq Q_{vi}^{max} \tag{19}$$

where:

P_{Gi} and Q_{Gi} are active and reactive power generation at bus i

P_{Di} and Q_{Di} are active and reactive loads at bus i

$P_{Pi}(\alpha_{Pk})$ and $Q_{Pi}(\alpha_{Pk})$ are the injected real and reactive power of TCSC at bus i

V_i and V_j are voltage magnitude at buses $_i$ and j

$Y_{ij}(X_s)$ and $\theta_{ij}(X_s)$ are the magnitude and angle the ij^{th} component in admittance matrix with TCSC

δ_i and δ_j are the bus i and j voltage angles

P_{Gi}^{min} *and* P_{Gi}^{max} are minimum and maximum bounds of real power generated at bus i

V_i^{min} *and* V_i^{max} are minimum and maximum bounds of real voltage valueat bus i

T_i^{min} *and* T_i^{max} are the minimum and maximum range of tap changing transformer

X_S is the vector reactance of TCSC

M is the sum of all buses

MG is the quantity of generator units

ML is the sum of all branches, and

MB_{SNK} is the total quantity r of load buses in sink/receive end area.

4.4. Proposed Optimization Techniques

i. Modified Genetic Algorithm

MGA is a stochastically biologically inspired technique presented by Storm and Price in 1997. MGA belongs to the family of genetic algorithms (GA). MGA performs just like a GA and it has the following operation: initialization, mutation, crossover, and selection. In MGA, characters are abridged chromosomes which programs the control parameters of the problem. Strengths of an individual characters gives the objective function commonly denoted as fitness that must be augmented in the optimization process. An arbitrary function has the chance yield the primary population size. Soon after the commencement, successive populaces are produced using the MGA process of iteration. This incorporates three rudimentary functional operations: -reproduction, crossover and mutation procedures. Finally, the population steadies since no healthier individual can be created. As the algorithm converges, and majority of the individual characters in the population are nearly undistinguishable hence denotes a sub-optimal results. The outcomes are critical in the determination of the optimization characteristics of the augmentation procedure. For application of MGA in resolution of additional and particular problem, one has to outline the solution illustration and the coding of control parameters. The augmentation problem in question is solved by use of Security Constrained Power Flow (SCOPF) to find the Total Transfer Capability for specified MGA-tuned FACTS devices to define optimal positions and compensation dimensions [13]. The basic operation of MGA is stated as follows: -

a) Initialization operation

The procedure for initialization will choose the primary population while operating within the span of the control parameters with an arbitral number creator. Users can hypothesize the quantity of population in this process.

b) Selection operation

This is a key reproduction procedure where individual chromosomes are derived as per their respective objective function/fitness. This is a simulated procedure that imitates the version of the Darwinian natural selection phenomenon. Initially, the reproduction process begins with selection of chromosomes for pairing. The roulette wheel selection is best suited in this for application at this instance. It is observed that stochastic common samples exhibit superior convergence characteristics.

c) Crossover operation

It's one of the crucial physiognomies of MGA augmentation tenets dissimilar from other optimization algorithms. The operation focal objective is to reconstitute blocks on varied individuals to create a new block of generations as shown in the equations below:

$$x^1 = \mu_1 x + \mu_2 y \tag{20}$$

$$y^1 = \mu_1 y + \mu_2 x \tag{21}$$

$$\mu_1 + \mu_2 = 1, \mu_1 \mu_2 > 0 \tag{22}$$

where *x*, *y* denotes two parents, *x'*, *y'* defines two descendants. μ_1 is gotten by an unchanging random number generator sandwiched between the range (0~l).

d) Mutation operation

This is vital in presentation of artificial divergence in the populace to shun untimely convergence to local optima. A computation operation demonstrated positive result in a numerous study is dynamic or non-even mutation is formulated for fine-tuning intended at attaining a highest degree of precision. For instance, provided with parent *x*, if gene x_k is designated for mutation operation, the resulting gene is chosen with equivalent likelihood from the two selections:

$$x_k^1 = x_k + r(b_k - x_k)\left(1 - \frac{t}{T}\right)^b \tag{23}$$

$$x_k^1 = x_k - r(x_k - a_k)(1 - \frac{t}{T})^{\mathrm{b}} \tag{24}$$

r denotes uniform random number selected between the span of (0,1), t is the prevailing generation number, T is the highest number of generations and b is a variable responsible for the degree of absence of constancy. The extent of mutation lessens as the number of generations upsurges.

e) Replacement of population

There are two population substitution approaches, non-overlapping generations and steady-state substitution. When utilizing non-overlapping generations, a generation was completely swapped by its progeny made via selection, crossover and mutation operation. It is conceivable for the offspring to be inferior than their parentages. Some of the fitter chromosomes may be vanished from the evolutionary process at this stage. The steady-state replacement or constant substitution is applied to go over and circumvent this problem. In this course, a number of offspring are created and these replace the same number of the least fit individuals in the population hence providing better convergence. [14] –[19]

ii. Improved Grey Wolf Optimization (IGWO) Algorithm

IGWO a newfangled swarm intelligence algorithm grounded on the firmly orderly scheme and hunting conduct of grey wolves, which comprises three parts: tracking prey, surrounding prey, attacking prey, and other optimization processes. It's abridged as shown in the diagram below:

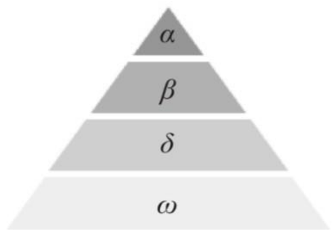

Figure 1: Grey wolf pack ranking

Wolf ranking Hierarchy

These wolves largely animate in clusters, and they follow a social pecking order, as shown in *figure 1*, displayed above. It can be realized from the figure that the α Wolf is the trailblazer of the social group and is mostly in authority for making choices and deciding about actions such as predation as the other wolves submit to the command of the α Wolf. Level 2: β Wolf, submitting and supplementary to the α Wolf, controls all the wolves excluding the α Wolf. Level 3: δ Wolf, submitting the authority of α and β Wolf at the same time, can rule the residual wolf pack. The ω wolves rank is the lowermost class in the pecking order. The universal predation conduct of grey wolves is controlled by α wolves, and the duty of other wolves is to confine the prey.

Surrounding prey

Grey wolves confine their prey as they hunt, hence stifling their movement. The computational model of enclosing the prey is outlined as follows: -

$$D = | C. Xp\,(t) - X\,(t) | \tag{25}$$

where $X(t)$ denotes the location of grey wolves, and Xp signifies the point vector of prey:

$$X\,(t+1) = X_{p\,-}\, A\cdot D \tag{26}$$

where A and C symbolize constant vectors, and the computational formula is shown below:

$$A = 2a\cdot(r_1\text{-}1) \tag{27}$$

$$C=2r\cdot t \tag{28}$$

where t denotes the existing sum of all iterations, and $a = 2\,(1\text{-}t/T_{max})$ denotes that the varying parameter decreases in a linear manner from 2 to 0, $r_1, r_2 \in [0,1]$ throughout the iteration course.

Hunting prey

These wolves also recognize prey and edge it. The hunt procedure is α Wolf commands and leads, β and δ sometimes, they will participate in hunting as well. Hypothesis α, β and δ. The wolf can have a profound comprehension of the probable site of prey, and consequently, during the algorithm process of iteration, keep the finest location of the three wolves in the existing population, and mark them as α, β and δ. Thereafter, in accordance with the position of the three parameters ϖ Wolf individuals are rationalized and updated. The computational model is thus advanced and established.

iii. Hybrid MGA and IGWO Algorithm

IGWO augmentation technique has been efficaciously applied in the areas of job planning, power system analysis, control and protection simulation, economic forecasting, among others. Yet, similar to other approaches, the algorithm is predisposed to falling prematurely into the local optimum and possess convergence speed of very low magnitudes. Hence, in order to increase the global convergence levels and better the convergence speeds, this research work has utilized MGA to mitigate this inadequacy. GWO's searching ability is based on two principles: exploration and exploitation. Exploration refers to the process of exploring new areas or mathematically, the process of looking for a solution as much as possible in a search space to prevent local optimum stagnation. On the other hand, exploitation refers to looking in the same direction in greater depth or mathematically, searching for a solution with high precision. Using the GWO algorithm to find the global optimum with high efficiency necessitates achieving the proper balance between exploration and exploitation. As compared to other swarm intelligent techniques, GWO algorithms perform well in finding the global optimum for the high-dimensional problem, but not so well in finding the global optimum for low-dimensional problems. Normal there is no guarantee that GWO will identify global minima, it is conceivable that it will stick with local minima and calculate corresponding angles that do not eliminate the third harmonic. To mitigate this issue, a donor vector from a MGA like the differential evolution technique is used, which adds randomness to the GWO technique and allows it to escape out of the local optimum and look in a new direction for the global optimum. Since the DE technique is based on accomplish random initialization, it outdoes finding the global optima, but it has a limitation in that it lacks a parameter that is directly related to algorithm convergence, so the speed of convergence is very slow and provides power oscillation around the global optima. As a result, the flaw in one approach is offset by another method. Therefore, a new algorithm called improved gray wolf optimization and differential evolution (IGWO-MGA) is proposed in this thesis, which combines the IGWO algorithm with a better convergence factor and the DE algorithm with a dynamic scaling factor with the help of a DE crossover operator. The initialization of a arbitrary vector of population size “N_p” with dimension “d” under boundary conditions is the first step in the IGWO-MGA method. Where ‘d’ denotes the problem dimension or the number of variables in the problem, and this random vector is referred to as the target vector, which can be described as shown below:

$$|X_i^t| = \left(x_{i,1}^t, x_{i,2}^t, x_{i,3}^t \ldots\ldots\ldots x_{i,d}^t\right) \tag{29}$$

where $i \in \{1,2,\ 3\ldots N_p\}$, and t is the current value of iteration and each individual can be calculated as follows:

$$x_{i,j} = x_{l,b} + rand\ (0,1)*(x_{ub} - x_{lb}) \tag{30}$$

where x_{ub}, x_{lb} are the upper bound and lower bound vectors with d individuals respectively. The same way as in IGWO, the three best results in IGWO-MGA are kept as alpha ($X{\rightarrow}\alpha$), beta ($X{\rightarrow}\beta$), and delta ($X{\rightarrow}\delta$) solutions from the target vector. Succeeding the saving of the results, the target vector is exposed to a mutation in a manner resembling the MGA technique. In the proposed algorithm, donor vector $V{\rightarrow}it$ is created from the target vector $X{\rightarrow}it$ using a DE/best/1 mutation approach with a dynamic scaling factor F', which offers more arbitrariness in the initial stages, preventing the algorithm from dropping into a local optimum, while the value of F' decreases in the final stages, boosting the algorithm's convergence speed. So, the donor vector can be stated as follows:

$$|V_i^t| = \left|X_{alpha}^t\right| + F' * (|X_{R1}| - |X_{R2}|) \tag{31}$$

where X_{alpha}, t is the α solution or best solution as far and X_{R1}, X_{R2} are the randomly selected solution from the target vector and F' can be expressed as follows:

$$F' = \frac{2}{1+e^{(k*(\frac{t}{tmax})}} \tag{32}$$

IGWO's searching ability is primarily determined by the vectors A and C, where C is a randomly generated vector ranging from 0 to 2, the wolves favor exploration if $C \rightarrow > 1$ and exploitation if $C < 1$, and C plays no role in IGWO's convergence speed. Now, the only vector that is important in convergence is A, but the value of A is determined by the convergence factor or a, and the value of a decreases linearly from 2 to 0 over the course of iteration. We need to adjust the convergence factor to enhance the speed of the algorithm as shown in the equation below:

$$F' = \frac{2}{1e^{(k*(\frac{t}{tmax}-\frac{1}{2})}} \tag{33}$$

Using this better convergence factor, the improved placement of the wolves can be calculated on the foundation of the position of the greatest wolves. Let us consider the ith position vector of wolves in the tth iteration as $W_i^t = \left[w_{i,2}^t, w_{i,2}^t \dots w_{i,d}^t\right]$ which can be calculated using equation. The two vectors are combined using a binomial crossover operator to generate a position vector for the next iteration. The new location vector can be defined as follows [20-24]:

$$X_{i,j}^{t+1} = \begin{cases} V_{i,j}^t \; if \; rand(0,1) \leq CR \; OR \; j = \delta \\ X_{i,j}^t \; if \; rand(0,1) > CR \; AND \; j \neq \delta \end{cases} \tag{34}$$

4.5. Research procedure

The objectives of this will be realized as follows:

1. An objective function based (base case, without FACTS) for maximization total transfer capability as the optimization problem will be formulated and solution derived
2. Singular Modified Genetic Algorithm and Improved Grey Wolf Optimization to solve the objective function, separately, via optimal location and sizing of FACTS devices will be developed
3. Hybrid Genetic Algorithm and Improved Grey Wolf Optimizer Algorithm will be developed and used to solve the function for maximizing power transfer capability while observing the voltage profiles and loos reduction
4. Hybrid Improved Grey Wolf Optimizer Algorithm and Genetic Algorithm with FACTS model above will be utilized to carry out simulations and evaluate effectiveness of model on improvement of power transfer capability

5. The results will be assessed and effects of individual FACTS devices compared to each other for the four system parameters under consideration.
6. The proposed test networks will be the standard IEEE 30 bus test system
7. Simulation will be carried out in MATLAB

5. RESULTS AND DISCUSSION

5.1. Results from the optimal power flow (Base case, without optimized FACTS)

5.1.1. Voltage profile curve (Base case, without optimized FACTS)

Figure 2 below shows the voltage profile curve for the base case (Base case, without optimized FACTS). The maximum p.u. value is observed at bus 12 (1.082p.u.) and lowest value is observed at bus 30 (0.995 p.u.).

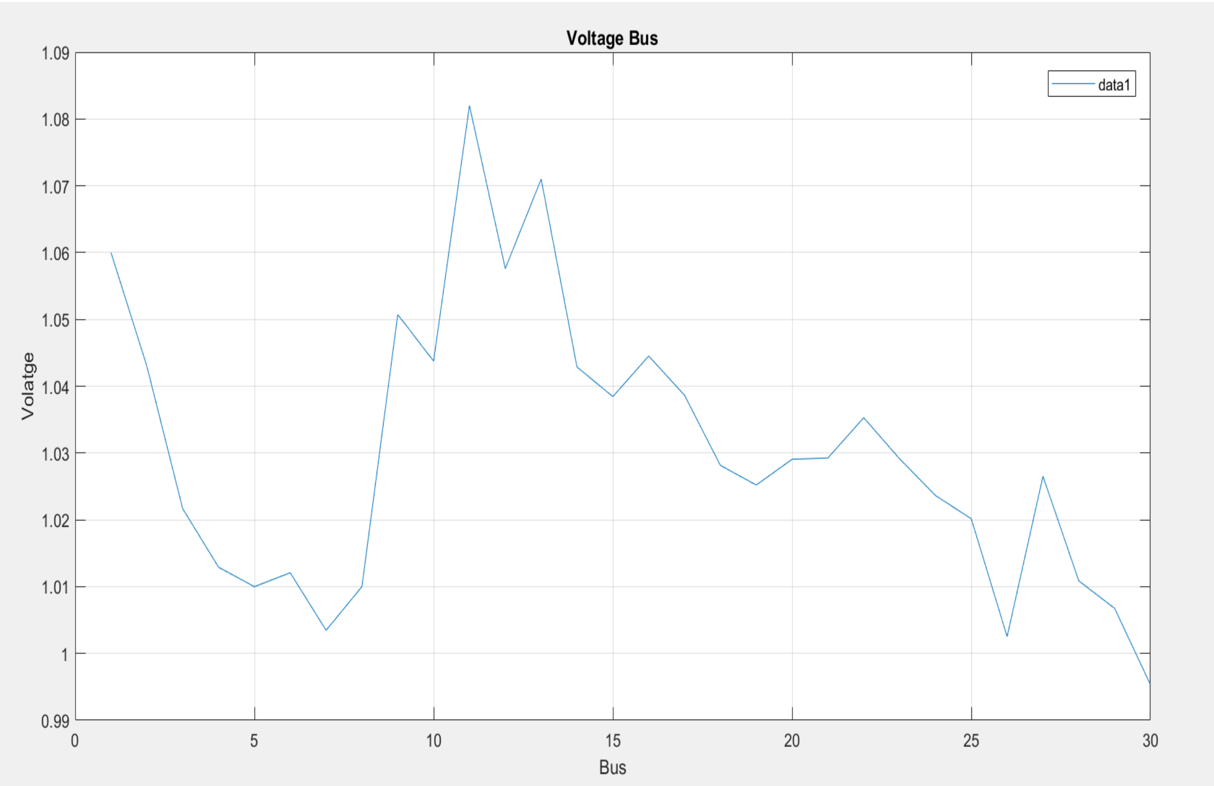

Figure 2: Voltage profile curve (Base case, without optimized FACTS

5.2. OPF with GA-tuned UPFC

5.2.1. Optimization results

The optimized values for GA-tuned UPFC are indicated in the table below:

Table 1. Optimization results

Parameter	Values
Voltage UPFC (PU)	1.01 and 1.03
Angle UPFC (R)	-0.01 and 0.54
Location UPFC (Bus)	Bus 1 and Bus 8

5.2.2. Voltage profile curve with GA-tuned UPFC

Figure 3 below shows the voltage profile curve for the with GA-optimized UPFC FACTS). The maximum p.u. value is observed at bus 12 (1.082p.u.) and lowest value is observed at bus 30 (0.995 p.u.). There is no significant variation of the voltage profiles with application of GA-tuned UPFC FACTS controller as compared to the base case scenario.

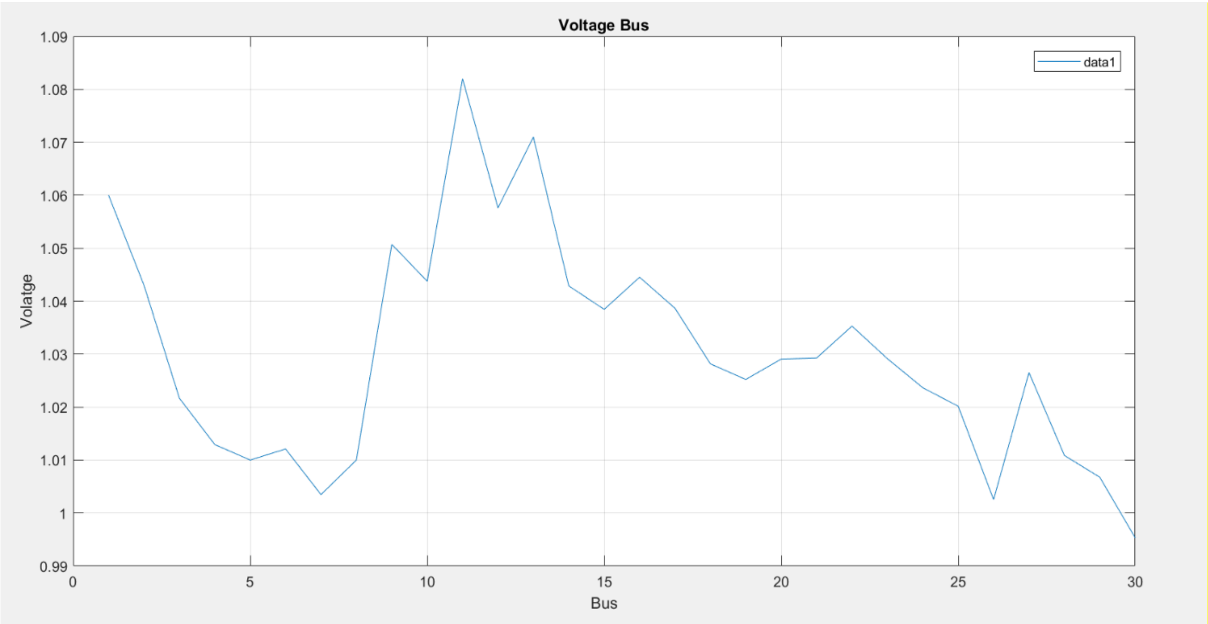

Figure 3: Voltage profile curve with GA-tuned UPFC

5.3. OPF with GA-tuned TCSC

5.3.1. Optimization Results

The optimized values for MGA-tuned TCSC are indicated in the table below:

Table 2. Optimization Results

Parameter	Values
Reactance TCSC (p.u.)	0 and 0.02
Location TCSC (Line)	40 and 4

5.3.2. Voltage profile curve with GA-tuned TCSC

Figure 4 below shows the voltage profile curve for the with MGA-optimized TCSC FACTS controller. The maximum p.u. value is observed at bus 12 (1.081p.u.) and lowest value is observed at bus 30 (0.997 p.u.). There is no significant variation of the voltage profiles with application of GA-tuned UPFC FACTS controller as compared to the base case scenario.

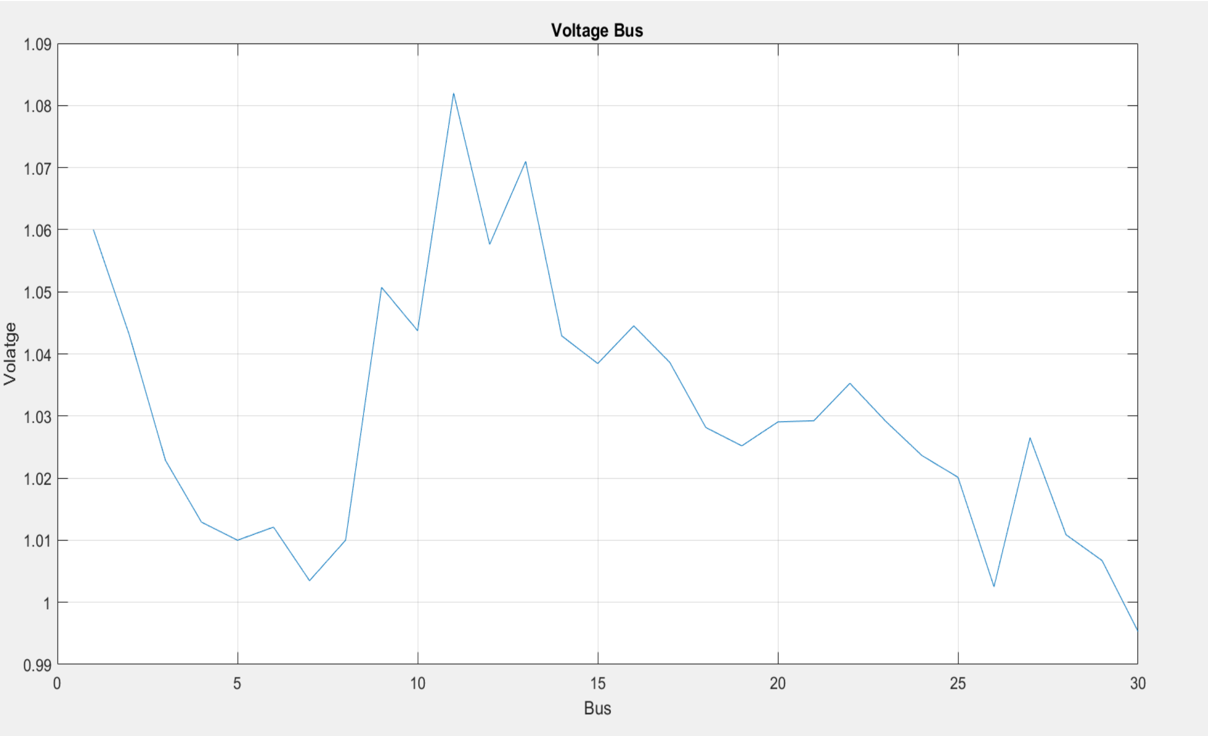

Figure 4: Voltage profile curve for the with GA-optimized TCSC FACTS Device

5.4. OPF with IGWO-tuned UPFC

5.4.1. Optimization results

Table 3 below shows the optimization results for IGWO-tuned UPFC:

Table 3: Optimization results

Parameter	**Values**
Voltage UPFC ()	1.04 1.05
Angle UPFC (R)	-1.08 -0.71
Location UPFC (Bus)	Bus 1 and Bus 8

5.4.2. Voltage profile curve with IGWO-tuned UPFC

Figure 5 below shows the voltage profile curve for the IGWO-optimized UPFC FACTS controller. The maximum p.u. value is observed at bus 12 (1.102p.u.) and lowest value is observed at bus 5 (1.03 p.u.). There is significant variation of the voltage profiles with application of IGWO-tuned UPFC FACTS controller as compared to the base case scenario and GA-tuned UPFC and GA-tuned TCSC FACTS controllers.

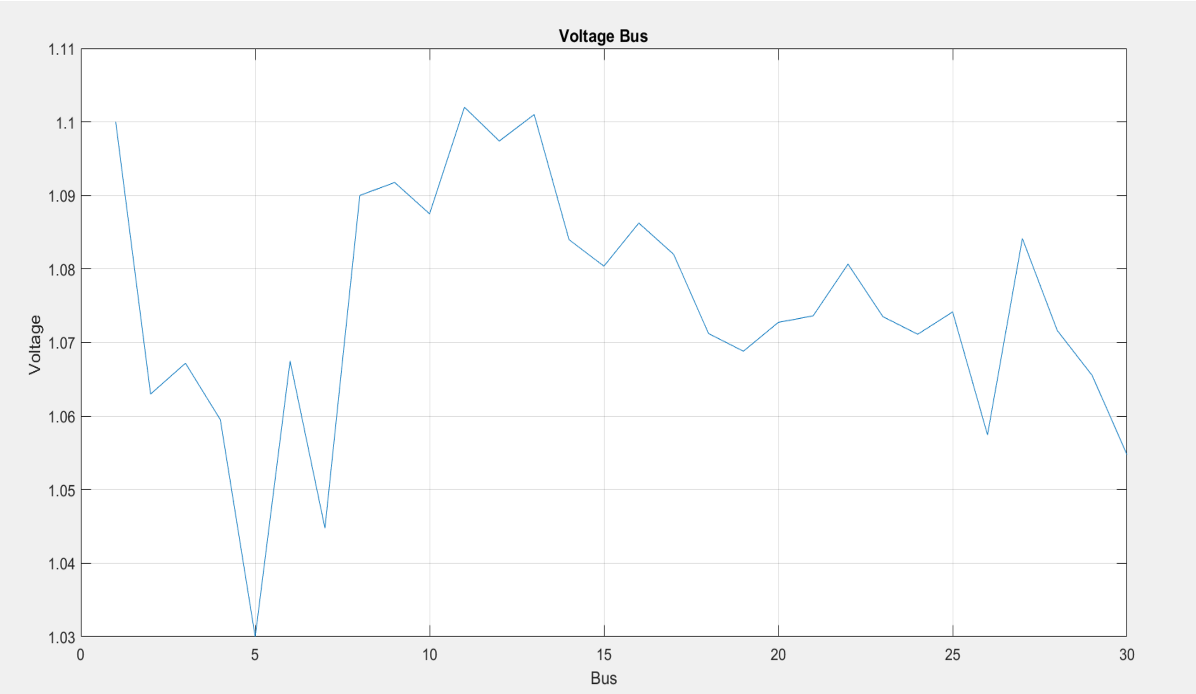

Figure 5: Voltage profile curve with IGWO-tuned UPFC

5.5. OPF with IGWO-tuned TCSC

5.5.1. Optimization results

Table 4 shows the optimization results for IGWO-tuned TCSC

Table 4. Optimization results

Parameter	**Values**
Reactance TCSC (PU) (p.u.)	0.015 and 0.0015
Location TCSC (Line)	Line 2 and Line 4

5.5.2. Voltage profile curve with IGWO-tuned TCSC

Figure 6 below shows the voltage profile curve for the with IGWO-optimized TCSC FACTS controller. The maximum p.u. value is observed at bus 12 (1.082p.u.) and lowest value is observed at bus 30 (0.995p.u.). There is no significant variation of the voltage profiles with application of IGWO-tuned TCSC FACTS controller as compared to the base case scenario and GA-tuned TCSC FACTS controllers but there is significant variation of the voltage profiles with GA-tuned UPFC case.

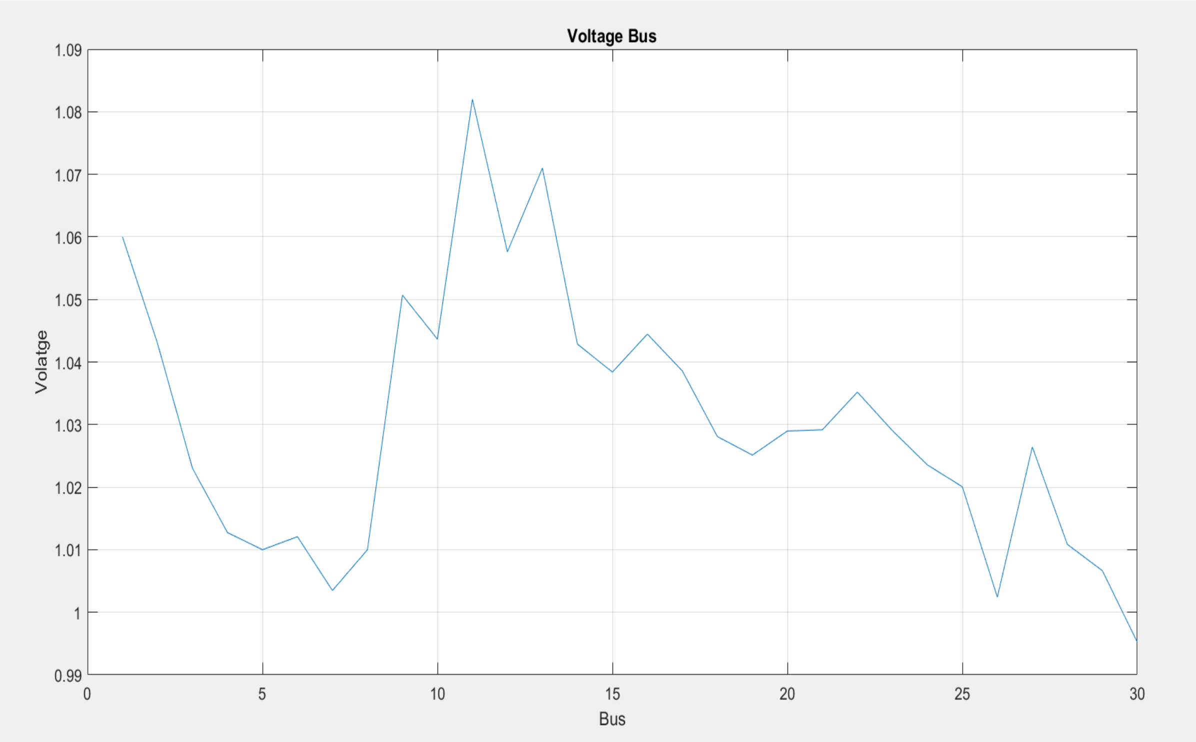

Figure 6: Voltage profile curve with IGWO-tuned TCSC

5.6. OPF with Hybrid MGA and IGWO-tuned UPFC

5.6.1. Optimization results

Table 5 below shows the optimization results for Hybrid MGA and IGWO-tuned UPFC

Table 5. Optimization results

Optimization Results	
Voltage UPFC (p.u.)	1.03 and 1
Angle UPFC ®	-0.51 and -0.65
Location UPFC (Bus)	Bus 30 and Bus 1

5.6.2. Voltage profile curve with Hybrid M and IGWO-tuned UPFC

Figure 7 below shows the voltage profile curve for the with Hybrid MGA and IGWO-optimized UPFC FACTS controller. The maximum p.u. value is observed at bus 12 (1.1302p.u.) and lowest value is observed at bus 5 (1.04 p.u.). There is significant variation and enhancement of the voltage profiles with application of Hybrid GA and IGWO-tuned UPFC FACTS controller as compared to the base case scenario and also as compared MGA-tuned UPFC MGA-tuned TCSC FACTS and IGWO-tuned UPFC controllers.

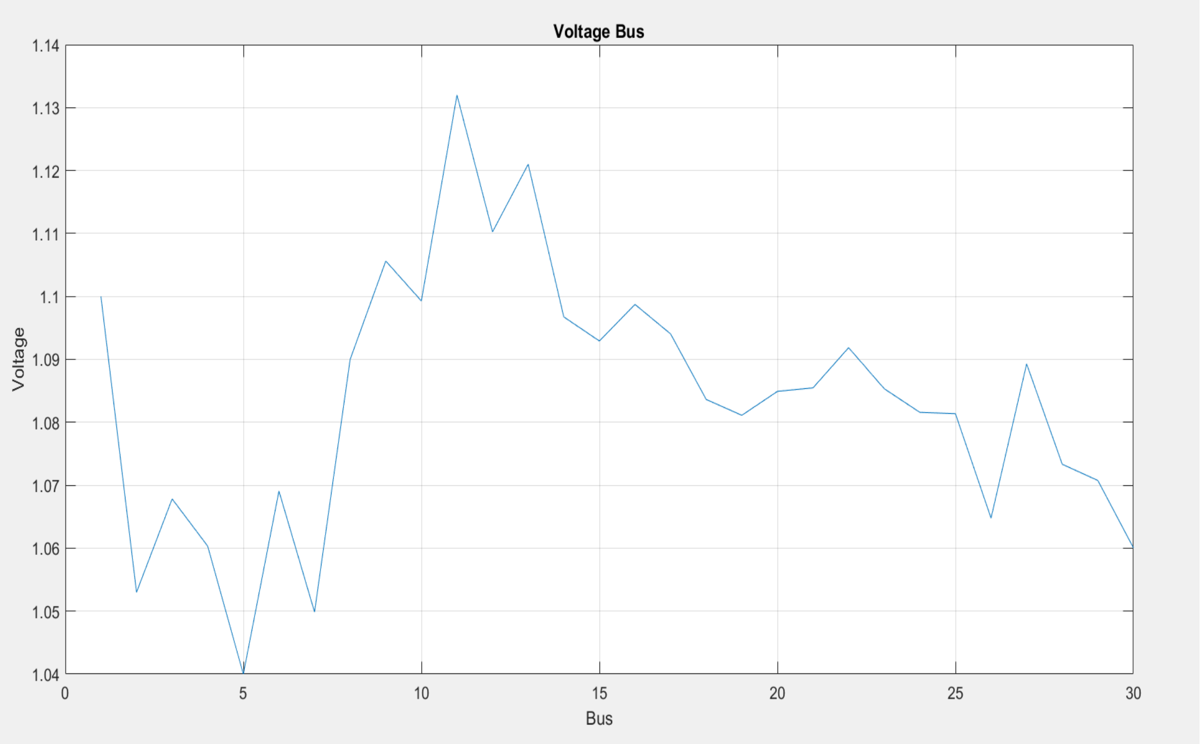

Figure 7: Voltage profile curve with Hybrid MGA and IGWO-tuned UPFC

5.7. OPF with Hybrid GA and IGWO-tuned TCSC

5.7.1. Optimization results

Table 6 below shows the optimization results for Hybrid MGA and IGWO-tuned TCSC

Table 6: Optimization results

Parameter	**Values**
Reactance TCSC (p.u.):	0.02 0.02
Location TCSC (Line):	Line 4 and Line 2

5.7.2. Voltage profile curve with Hybrid MGA and IGWO-tuned TCSC

Figure 8 below shows the voltage profile curve for the Hybrid MGA and IGWO-tuned TCSC FACTS controller. The maximum p.u. value is observed at bus 12 (1.082p.u.) and lowest value is observed at bus 30 (0.995 p.u.). There is no significant variation and enhancement of the voltage profiles with application of Hybrid MGA and IGWO-tuned TCSC FACTS controller as compared to the base case scenario and also as compared to MGA-tuned TCSC FACTS and IGWO-tuned TCSC. There is however significant variation and enhancement of the voltage profiles with MGA-tuned UPFC.

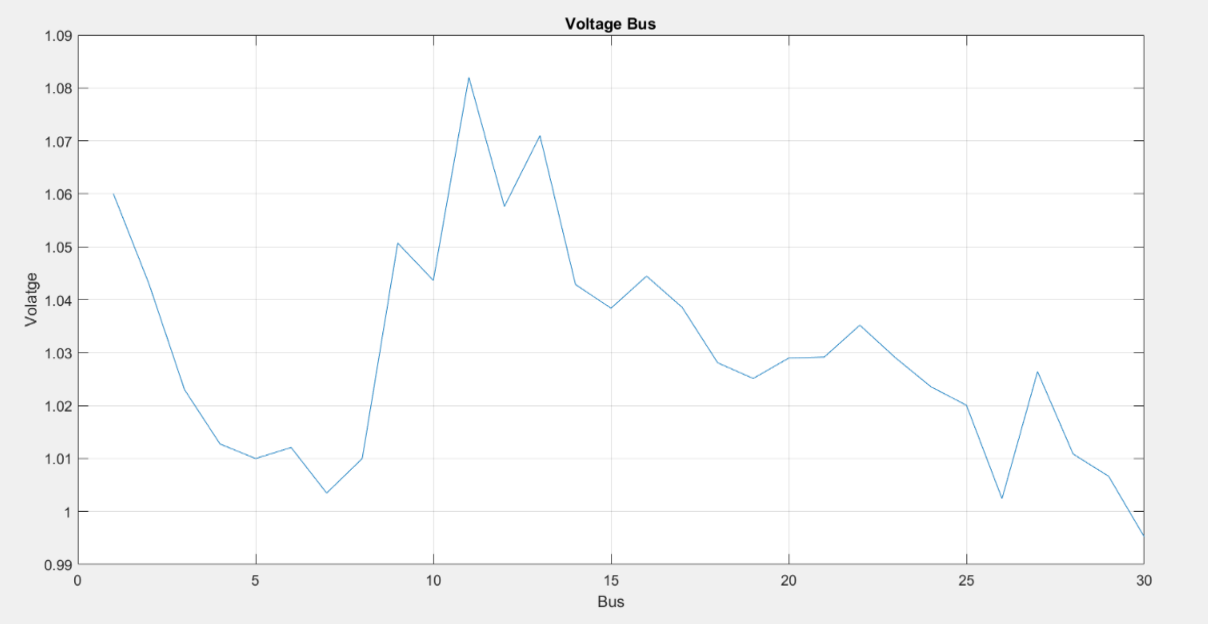

Figure 8: Voltage profile curve with Hybrid GA and IGWO-tuned TCSC

5.8. Bus voltage profiles for different optimization techniques

The voltage profile curve for the base case (Base case, without optimized FACTS). The maximum p.u. value is observed at bus 12 (1.082p.u.) and lowest value is observed at bus 30 (0.995 p.u.). For the voltage profile curve for the with GA-optimized UPFC FACTS), the maximum p.u. value is observed at bus 12 (1.082p.u.) and lowest value is observed at bus 30 (0.995 p.u.). There is no significant variation of the voltage profiles with application of GA-tuned UPFC FACTS controller as compared to the base case scenario. For the voltage profile curve for the with MGA-optimized UPFC FACTS), the maximum p.u. value is observed at bus 12 (1.082p.u.) and lowest value is observed at bus 30 (0.995 p.u.). There is no significant variation of the voltage profiles with application of GA-tuned UPFC FACTS controller as compared to the base case scenario. For the voltage profile curve for the with MGA-optimized TCSC FACTS controller, the maximum p.u. value is observed at bus 12 (1.081p.u.) and lowest value is observed at bus 30 (0.997 p.u.). There is no significant variation of the voltage profiles with application of MGA-tuned UPFC FACTS controller as compared to the base case scenario. For the voltage profile curve for the with IGWO-optimized UPFC FACTS controller, the maximum p.u. value is observed at bus 12 (1.102p.u.) and lowest value is observed at bus 5 (1.03 p.u.). There is significant variation of the voltage profiles with application of IGWO-tuned UPFC FACTS controller as compared to the base case scenario and GA-tuned UPFC and GA-tuned TCSC FACTS controllers. For the voltage profile curve for the with IGWO-optimized TCSC FACTS controller, the maximum p.u. value is observed at bus 12 (1.082p.u.) and lowest value is observed at bus 30 (0.995p.u.). There is no significant variation of the voltage profiles with application of IGWO-tuned TCSC FACTS controller as compared to the base case scenario and GA-tuned TCSC FACTS controllers but there is significant variation of the voltage profiles with MGA-tuned UPFC case. For the voltage profile curve for the with IGWO-optimized UPFC FACTS controller, the maximum p.u. value is observed at bus 12 (1.1302p.u.) and lowest value is observed at bus 5 (1.04 p.u.). There is significant variation and enhancements of the voltage profiles with application of Hybrid MGA and IGWO-tuned UPFC FACTS controller as compared to the base case scenario and also as compared MGA-tuned UPFC GA-tuned TCSC FACTS and IGWO-tuned UPFC controllers. For the voltage profile curve for the with Hybrid MGA and IGWO-tuned TCSC FACTS controller, the maximum p.u. value is observed at bus 12 (1.082p.u.) and lowest value is observed at bus 30 (0.995 p.u.). There is no significant variation and enhancement of the voltage profiles with application of Hybrid MGA and IGWO-tuned TCSC FACTS controller as compared to the base case scenario and also as compared to MGA-tuned TCSC FACTS and IGWO-tuned TCSC. There is however significant variation and enhancements of the voltage profiles with MGA-tuned UPFC.

The figure below shows the bus voltage profiles for different optimization techniques**:**

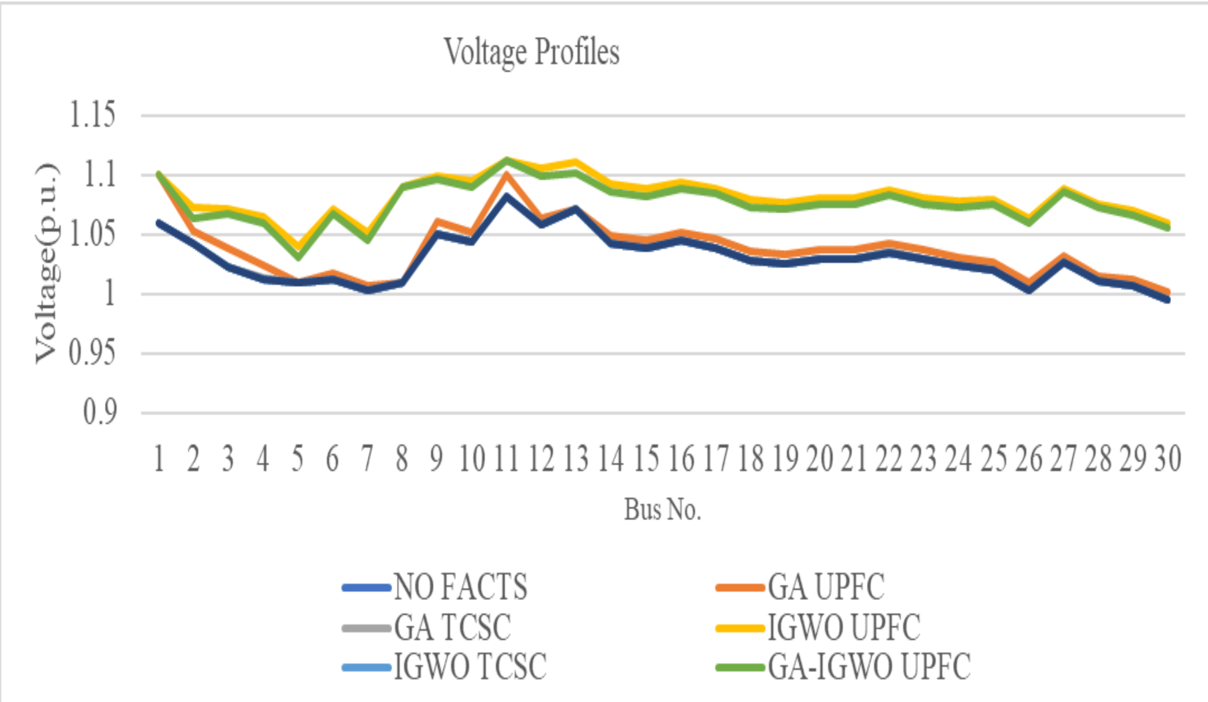

Figure 9: bus voltage profiles for different optimization techniques

6. CONCLUSION

There is no significant variation of the voltage profiles with application of GA-tuned UPFC FACTS controller as compared to the base case scenario. For the bus voltage profile curve for the GA-optimized TCSC FACTS controller, the maximum p.u. value is observed at bus 12 (1.081p.u.) and lowest value is observed at bus 30 (0.997 p.u.). There is no significant variation of the voltage profiles with application of GA-tuned UPFC FACTS controller as compared to the base case scenario. For the voltage profile curve for the with IGWO-optimized UPFC FACTS controller, the maximum p.u. value is observed at bus 12 (1.102p.u.) and lowest value is observed at bus 5 (1.03 p.u.). There is significant variation of the voltage profiles with application of IGWO-tuned UPFC FACTS controller as compared to the base case scenario and GA-tuned UPFC and GA-tuned TCSC FACTS controllers. For the voltage profile curve for the with IGWO-optimized TCSC FACTS controller, the maximum p.u. value is observed at bus 12 (1.082p.u.) and lowest value is observed at bus 30 (0.995p.u.). There is no significant variation of the voltage profiles with application of IGWO-tuned TCSC FACTS controller as compared to the base case scenario and GA-tuned TCSC FACTS controllers but there is significant variation of the voltage profiles with GA-tuned UPFC case. For the voltage profile curve for the with IGWO-optimized UPFC FACTS controller, the maximum p.u. value is observed at bus 12 (1.1302p.u.) and lowest value is observed at bus 5 (1.04 p.u.). There is significant variation and enhancements of the voltage profiles with application of Hybrid GA and IGWO-tuned UPFC FACTS controller as compared to the base case scenario and also as compared MGA-tuned UPFC, GA-tuned TCSC FACTS and IGWO-tuned UPFC controllers. For the voltage profile curve for the with Hybrid GA and IGWO-tuned TCSC FACTS controller, the maximum p.u. value is observed at bus 12 (1.082p.u.) and lowest value is observed at bus 30 (0.995 p.u.). There is no significant variation and enhancements of the voltage profiles with application of Hybrid GA and IGWO-tuned TCSC FACTS controller as compared to the base case scenario and also as compared to GA-tuned TCSC FACTS and IGWO-tuned TCSC. There is however significant variation and enhancements of the voltage profiles with GA-tuned UPFC. From the bus voltage profiles, Hybrid MGA and IGWO with UPFC FACTS controller showed the most significant improvement of bus voltages. It imperative to note that the techniques have brought out the inherent strengths of the FACTS controllers applied. UPFC FACTS controller showed strong performance in voltage profile improvement compared to TCSC FACTS controller. Thus, for systems with voltage profile challenges, IGWO tuned UPFC FACTS controller is preferred to tuned TCSC FACTS controller.

REFERENCES

[1] A. Naganathan and V. Ranganathan, *Improving Voltage Stability of Power System by Optimal Location of FACTS Devices Using Bio-Inspired Algorithms*, Circuits and Systems ISSN: 2153-1293, Volume-, Issue-6, May 2016.

[2] N. Kumar and K. Rosalina, *IPSO Algorithm for Maximization of System Loadability, Voltage Stability and Loss Minimization by Optimal DG Placement*, International Journal of Innovative Research in Electrical, Electronics, Instrumentation and Control Engineering ISSN: 2321, Volume-3, Issue-11, May 2015.

[3] S. Saini and G. Kaur, *Optimal Placement and Sizing of Distributed Generation for Real Power Loss Reduction in Distribution Network*, International Research Journal of Engineering and Technology ISSN: 2454- 2024, Volume 1 Issue 3, June 2016.

[4] M. Chakravorty and S. Patra, *Multi-Objective Teaching Learning Based Optimization Technique for Loss Reduction and Fast Voltage Stability Index Minimization*, International Journal of Recent Technology and Engineering ISSN: ISSN: 2395 -0056, Volume: 04 Issue: 04, April 2017.

[5] B. Bhattacharyya, V. Gupta and S. Kumar, *UPFC with series and shunt FACTS controllers for the economic operation of a power system*, Ain Shams Engineering Journal ISSN: 775-778, May 2014.

[6] E. Acha. R. Fuerte-Esquivel, and H. Ambriz-Perez et al., *FACTS: Modeling and Simulation in Power Networks*, London, U.K.: Wiley, 2004.

[7] K. Venkateswarlu, C. Babu, *Analysis and Enhancement of Transient Stability using Shunt Controlled FACTS Controller*, International Journal of Engineering Sciences Research-IJESR, ISSN: 2230-8504; e-ISSN-2230-8512, Volume 1, Issue 02, May, 2011.

[8] M. Abido, *Power System Stability enhancement using FACTS controllers: a review*, The Arabian Journal for Science and Engineering, Volume 34, Number 1B, April 2009.

[9] N. Mancer, B. Mahdad, K. Srairi and M. Hamed, *Multi Objective for Optimal Reactive Power Flow Using Modified PSO Considering TCSC*, International Journal of Energy Engineering, 2(4): 165-170, 2012.

[10] A. Lopez and L. Alonso, *Modeling and Stability Analysis of Berlin Geothermal Power Plant in El Salvador*, Master's Thesis, University of Iceland Reykjavik, pp. 3-56, April 2013.

[11] C. Rajan, *A Hybrid Genetic Algorithm based on Differential Evolution Approach for Voltage Stability Improvement*, International Journal of Computer Applications (0975 – 8887), Volume 86 – No 16, January 2014.

[12] J. Manohar, A. Jinka and V. Rao, *Optimization of Loss Minimization Using FACTS in Deregulated Power Systems*, Innovative Systems Design and Engineering, ISSN 2222-2871, Volume 3, No 3, 2012.

[13] S. Mirjalili, S. M. Mirjalili, A. Lewis, *Grey Wolf Optimizer*, Advances in Engineering Software, vol. 69, pp.46-61, 2014.

[14] H. Hassan and M Zellagui, *Application of Grey Wolf Optimization Algorithm for Optimal Power Flow of Two-Terminal HVDC Transmission System*, Journal of Power Engineering and Electrical Engineering, Volume 15: No: 2017.

[15] Z. Wang, H. Xie Et al, *Node coverage optimization algorithm for wireless sensor networks based on Improved Grey wolf Optimization Algorithm*, Journal of Algorithms & Computational Technology, Volume 13: pp.1–15,2019.

[16] R. Sireesha, S. R. Coppisetty and M. V. Kumar, *Hybrid optimization to enhance power system reliability using GA, IGWO, and PSO*, Paladyn, Journal of Behavioral Robotics; Volume 14: 20220119, 2023.

[17] F. Ikule, A. Ame-Oko and E. Idoko, *Load flow analysis using Newton-Raphson method, a case study of south-west Nigeria 330 kV network*, International Journal of Advance Research and Innovative Ideas in Education, ISSN(O)-2395-4396, Vol-5 Issue-3, 2019.

[18] Afolabi, O. A Et al., *Analysis of the Load Flow Problem in Power System Planning Studies*. Energy and Power Engineering, vol.7, 509-523, 2015.

[19] S. K. Goswami and S. K. Basu, *Direct solution of distribution systems*, IEE Proc., pt. C, vol. 188, no. 1, pp. 78-88, 1999.

[20] J. Glover and M. Sara, *2nd Power System Analysis and Design*. 3rd Edition, Brooks/Cole, Pacific Grove. 2002.

[21] D. Mander and G. Virdi, *Result Analysis on Load Flow by Using Newton Raphson Method*, International Journal of Advanced Research in Electrical, Electronics and Instrumentation Engineering, vol. 6, no. 7, pp. 5835-5844, 2017.

[22] Y. Han, *Economic dispatching Optimization of power grid based on IGWO Algorithm*, Journal of Physics: Conference Series, 1748 032009: doi:10.1088/1742-6596/1748/3/032009, 2021.

[23] H. W. Reyad, M. Elfar and E. E. El-Araby, *Probabilistic Assessment of Available Transfer Capability Incorporating Load and Wind Power Uncertainties*, IEEE Open Access Journal, Volume 11, April 2023.

[24] M. Nadimi-Shahraki, S. Taghian and S. Mirjalili, *An Improved Grey Wolf Optimizer to solve Engineering Problems*, Expert Systems with Applications, Vol. 166, March 2021.

Received: October 2024, Accepted: December 2024, Published: December 2024
Digital Object Identifier: https://doi.org/10.34302/CJEE/XLCI7386

DESIGN OF A VIRTUAL TEMPERATURE SENSOR WITH DATA DISPLAY IN A WEB INTERFACE

Paul **NISTOR**, Ioan **ORHA**
Electric, Electronic and Computer Engineering Department, Technical University of Cluj-Napoca, Romania
nistorpaul97@gmail.com, ioan.orha@ieec.utcluj.ro

Keywords: sensors, machine learning, web interfaces

Abstract: *The project presents the design and implementation of a virtual temperature sensor with the display of the data provided by it in a web interface. The objective of the whole project is based on the development of a virtual sensor that estimates the temperature with the help of historical but also current data provided by other sensors. The goal of this project is to reduce the cost of temperature monitoring systems by reducing the physical sensors required. It is also aimed at the possibility of implementing these sensors in inaccessible places. Following the use of a machine learning type system, I want to implement a predictive model, which, based on the data provided by the other physical sensors, generates the response of the virtual sensor. Both the data provided by the virtual sensor and the data provided by the physical sensors will be displayed within the web interface. The project aims to develop a sensor network for temperature monitoring in various applications. Also, by implementing this system, I want to obtain a web interface that allows viewing and managing the measured temperature data.*

1. INTRODUCTION

In our century, data monitoring and management has become a matter of major importance in multiple fields. Among them we can list industry, agriculture and the research environment itself. These fields and many others need this data in order to function optimally but also for continuous development [1].

But in many cases the collection of this data would not be possible without the help of sensors. Among them the temperature sensor stands out, it plays a crucial role in the collection of data aimed at ensuring optimal equipment performance, product protection, process optimization and user comfort. Therefore, temperature is a parameter that must be constantly monitored in multiple fields [2].

As a result of this need to measure temperature, several types of sensors with various properties and characteristics have been developed. We can divide these sensors into two categories. The first category being contact sensors, which measure the temperature by direct contact with the object. The second category is non-contact sensors, which measure the temperature through the heat radiation emitted by the object, without making direct contact with it [3].

Although sensors have constantly evolved and developed, installing an adequate number of sensors to obtain a quality measurement can cause various problems. Therefore adding additional sensors is limited by factors such as budget, available space and accessibility. For example, in an industrial facility with an extensive area, adding additional temperature sensors to expand the monitoring network can involve high costs and increased complexity. In research laboratories, where space is often constrained, adding additional sensors may not be the most efficient solution [4].

In order to solve these problems, we found that replacing a set of physical sensors with virtual sensors within a sensor network is an efficient and pragmatic solution. Thus, by means of virtual sensors costs can be reduced, they facilitate the monitoring of places inaccessible to physical sensors, they save space and solving problems in case of failure is easier to solve than in the case of physical sensors.

This project aims to develop a virtual temperature sensor that, with the help of machine learning algorithms, will estimate the temperature based on data received from nearby physical sensors. The project also aims to integrate this virtual sensor within a web interface to facilitate access to the data provided by the sensors in real time. Therefore, the implementation of this system based on virtual sensors, in addition to solving the previously described problems, also improves the quality of measurements by integrating and analyzing data from multiple sources.

2. SYSTEM DESCRIPTION

2.1. Description of Functional Blocks

The presented system consists of two parts, a hardware part and a software part. The hardware part consists of the temperature sensors and the ESP-32 microcontroller. The software part includes storing the data in a database, the machine learning algorithm that predicts the response for the virtual sensor and displaying the data in a web interface. The block diagram of the whole system is shown in *fig. 1*.

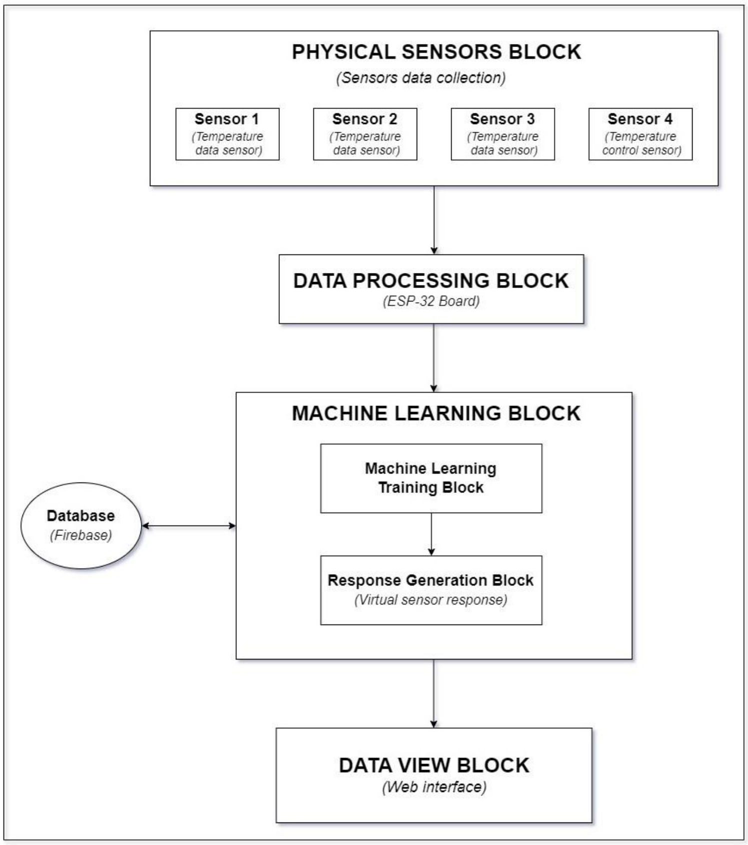

Fig. 1. System structure

The first block encountered in the presented scheme comprises the physical sensors, this block contains four temperature sensors. Although four sensors are shown, only the data from the first three will be used in the machine learning model. The fourth sensor, as the name suggests is a control sensor, it is located in the same location as the virtual sensor and aims to measure the actual temperature in that area. The value provided by this sensor will be used to compare the response generated by machine learning with the actual temperature value. The number of sensors present within this block may vary depending on the needs of the application. For example, in a real application, the control sensor can be removed, and other physical sensors can be added as needed to increase the accuracy of the virtual sensor response.

The second block is represented by the ESP-32 board, it plays a crucial role in the system, because as the name of the block suggests, it deals with data processing. Specifically, this block collects the data from the temperature sensors, filters the noise, normalizes the values, and prepares this data for transmission to the next block.

The next stage within the presented scheme is carried out by the machine learning block, which represents the most important component of the entire system. It contains two essential blocks.

The machine learning training block, in this the data is used to train the machine learning model. In this stage of the system, historical data stored in the database and new data received from sensors via the ESP-32 board are analyzed. The model is built and updated based on this data with the aim of improving itself over time in such a way as to generate the most accurate estimate for the virtual sensor. Essentially, constantly adding new data to the existing data set and retraining the model leads to improved response accuracy.

The response generation block, once the training of the machine learning model is finished, predictions can be made based on the current data, and the obtained value representing the response of the virtual sensor. In this block the virtual sensor value prediction is actually performed.

Within the scheme presented, the database block can also be observed, it represents an important component for the best and most accurate functioning of machine learning. The Firebase database stores all the data generated by the physical sensors but also all the predictions of the virtual sensor. With the help of this block, the system constantly stores new data for continuous training of the machine learning model.

The last block in the scheme is the data visualization block, in this block the data is displayed in a web interface. Through this interface data can be monitored in real time and easily. The processed data from the sensors and the responses generated by the virtual sensor are visualized in the form of a table in this interface.

In conclusion, the presented block diagram describes a well-structured system that combines the hardware part with the software part in order to obtain and visualize the most accurate data, both from the physical sensors and from the virtual sensor.

2.2. Basis of Machine Learning - Polynomial Regression

Polynomial regression is an extension of linear regression, it is used to model more complex relationships between variables, especially when the dependent variable and the independent variables have a non-linear relationship [5].

Within the sensor system, we considered the use of polynomial regression an optimal solution for obtaining the values of the virtual sensor based on the data collected from the other physical sensors. The model underlying machine learning is capable of processing non-linear variations from real data, thus making the chosen model ideal for modeling sensor data that does not have a strictly linear relationship.

The working principle of polynomial regression is to try to minimize the difference between the actual values and the prediction values in the data set. This modeling uses a curve that can have several changes in direction in order to fit the data as well as possible to obtain the most accurate temperature prediction. In *fig. 2* you can see the polynomial regression graph for predicting the temperature.

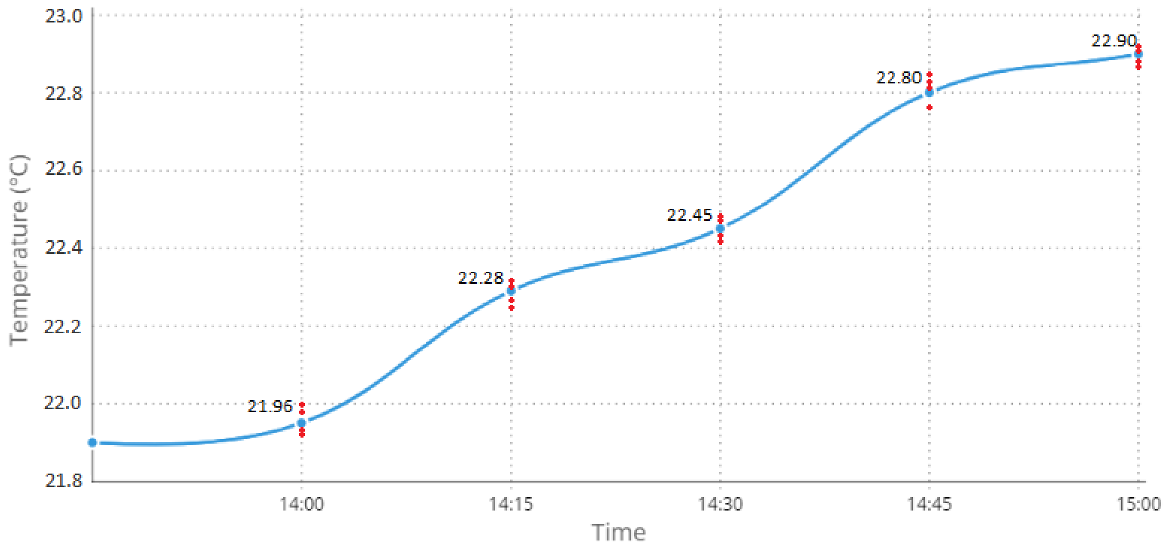

Fig. 2. Polynomial regression graph for temperature prediction

In the graph presented, it can be seen how the polynomial regression curve representing the response of the virtual sensor is generated based on the four values from the physical sensors.

In the previous paragraphs, the operating principle of the model that is the basis of machine learning was presented in a theoretical way. In the following we will present how polynomial regression works in machine learning code.

Within the code, the historical data from the four physical sensors are combined into a two-dimensional matrix, where each row represents the sensor measurements at a particular time. And in order to provide the prediction, the output is calculated as an average of the four sensors, which gives us an approximate value for the temperature of the virtual sensor. The described process represents the training of the machine learning model with the historical data and the code sequence responsible for this step is shown in *fig. 3*.

```
function trainModel() {
    const input = sensor1Data.map((_, index) => [
        sensor1Data[index],
        sensor2Data[index],
        sensor3Data[index],
        sensor4Data[index]
    ]);

    console.log(input);
    const output = sensor1Data.map((_, index) =>
        (sensor1Data[index] + sensor2Data[index] + sensor3Data[index] + sensor4Data[index]) / 4
    );
```

Fig. 3. Syntax code responsible for training of the machine learning model with historical data

After training the polynomial regression with this historical data, a model is generated that is used for real-time predictions.

Although there are other possibilities to implement machine learning, we considered that in this sensor system the use of this solution is optimal from the point of view of complexity and performance. Polynomial regression is simpler than other models used for machine learning, but in terms of performance it contributes significantly to improving virtual sensor temperature prediction by adapting to fluctuations in physical sensor data. This fact makes machine learning much more effective in real environments.

3. EXPERIMENTAL MEASUREMENTS

In this chapter we evaluated the performance of the system in different configurations. Before presenting these measurements, it is important to describe how the system operates. In a simplified way, the system works like this: the data collected from the physical sensors is sent to the machine learning model, which uses the new data together with the historical data retrieved from the database to generate the response of the virtual sensor. Following this operation, the physical sensor and virtual sensor data will be saved in the database and transmitted to the web interface for display. The described process is repeated at a predetermined time interval.

In this chapter we tested the performance and reliability of the virtual sensor through two experiments. During these experiments, we exposed the system to various configurations where we varied the number of physical sensors used and the sensor placement arrangement. In order to obtain the most conclusive results, the two experiments were carried out in similar environments, more precisely in a laboratory room.

We mention that in both experiments to measure the accuracy of the virtual sensor, we placed a physical control sensor, its physical location is exactly where the virtual sensor makes the temperature prediction.

In the following we will present the two configurations in which the system was tested, the various measurements performed and the results obtained.

3.1. Evaluation of Triangle and Square Configurations

In the first experiment we used the triangle configuration, this involves the use of three physical temperature sensors that were placed in the shape of a triangle and a control sensor placed in the middle of the triangle. Based on the data collected from the three sensors, machine learning generated the response of the virtual sensor. And finally, to compare the accuracy of the virtual sensor, its responses were compared with the values measured by the fourth physical sensor, the control sensor, which is located in the same location where the virtual sensor makes the temperature prediction. In Table 1 you can see the data obtained with the triangle configuration.

Table 1. Data table for the triangle configuration

Time	Sensor 1 (°C)	Sensor 2 (°C)	Sensor 3 (°C)	Control Sensor (°C)	Virtual Sensor (°C)	Difference (%)
12:15	20.94	20.71	20.87	20.77	20.92	0.72
12:30	21.15	20.82	20.89	20.81	20.90	0.43
12:45	21.36	20.93	21.05	20.87	21.01	0.67
13:00	21.58	21.05	21.20	21.05	21.15	0.47
13:15	21.79	21.18	21.36	21.45	21.33	0.56
13:30	21.92	21.45	21.54	21.75	21.65	0.47
13:45	22.03	21.68	21.70	21.89	21.97	0.37
14:00	22.27	21.87	21.85	22.11	22.18	0.32
14:15	22.48	22.10	22.01	22.53	22.42	0.48
14:30	22.74	22.40	22.25	22.68	22.53	0.67
14:45	22.85	22.75	22.50	22.75	22.88	0.57
15:00	23.14	23.01	22.75	23.07	22.97	0.44

The presented table contains the data collected from the physical and virtual sensors during the experiment. In the last column we made a comparison where we can see the difference between the generated values and the actual measured value.

In the second experiment, we used the square configuration, using four temperature sensors that we placed in a square shape in the laboratory room. As in the first experiment, the data collected from the sensors was used for the machine learning model that generated the response of the virtual sensor. The value obtained is again compared with the value of the control sensor located in the center of the square. Table 2 shows the data obtained with the square configuration.

Table 2. Data table for the square configuration

Time	Sensor 1 (°C)	Sensor 2 (°C)	Sensor 3 (°C)	Sensor 4 (°C)	Control Sensor (°C)	Virtual Sensor (°C)	Difference (%)
12:45	20.39	20.10	19.90	20.15	20.12	20.19	0.35
13:00	20.51	20.33	20.15	20.43	20.41	20.35	0.29
13:15	20.82	20.60	20.45	20.75	20.67	20.77	0.48
13:30	21.14	20.95	20.80	21.19	21.02	21.07	0.23
13:45	21.25	21.20	21.12	21.37	21.32	21.25	0.33
14:00	21.60	21.55	21.33	21.45	21.56	21.50	0.28
14:15	21.90	21.70	21.62	21.85	21.75	21.85	0.46
14:30	22.27	22.05	21.91	22.15	22.10	22.19	0.36
14:45	22.58	22.40	22.01	22.25	22.35	22.42	0.31
15:00	22.79	22.65	22.31	22.55	22.67	22.58	0.40
15:15	22.84	22.75	22.52	22.83	22.74	22.69	0.22
15:30	23.04	22.85	22.77	23.12	22.88	22.94	0.26

We chose this configuration to see what impact adding a temperature sensor in addition to the previous configuration has on temperature prediction accuracy. We also looked at whether the square geometric position improves the accuracy and reliability of the system.

As can be seen in the last column of each table presented above, the machine learning model was able to generate accurate temperature predictions in both scenarios, but as expected the accuracy was higher in the case of the four-sensor configuration. Therefore, we can conclude that a larger number of physical sensors contribute to improving the performance and obtaining a better temperature prediction. Following the two experiments, it can also be seen that both configurations produced satisfactory results, specifically the triangle configuration had a margin of error of the response between 0.32-0.72%, while the square configuration had a smaller margin of error, between 0.22-0.48%.

Analyzing the two experiments strictly from a performance point of view, it is clear that the four-sensor system is the favorite, however using this configuration in an extended network would generate additional costs due to the fourth sensor. Therefore, if we wish a more economical system, but with slightly reduced accuracy, the configuration with three sensors is ideal. On the other hand, if high efficiency is a priority, the four-sensor system is the optimal choice.

We mention that both configurations improve their accuracy over time, because in the experiments we used a relatively small amount of data to train the machine learning model. However, in a real application, running over an extended period of time, the system can accumulate a very large set of data, which will train the machine learning model and greatly improve its accuracy.

3.2. The Motivation Behind the Chosen Configurations

We would like to point out that the presented system can work in different configurations than those presented. For example, the virtual sensor can work with only two physical temperature sensors, but it can also work with five or more sensors. But based on the experiments we concluded that the use of only two sensors considerably reduces the performance, and the use of several sensors considerably increases the costs. Thus, within the system we opted for the use of the two scenarios, with three and four sensors, because in this way the system has a balance in terms of performance and economy.

The choice of the two geometric configurations, triangle and square respectively, is not random. We considered these arrangements to be optimal for future sensor network developments, as these simple geometries provide us with an efficient solution in terms of how to place and interconnect sensors. For example, the implementation of the system on a larger scale requires a model of placement and organization of sensors because a random placement would complicate the expansion of the network later. Therefore, the geometric shapes presented give us a way of connecting and distributing the sensors very well organized.

Another reason we chose these configurations is that they allow for more accurate spatial monitoring. Triangle and square configurations ensure an even distribution of sensors, effectively covering the entire monitored area. If the physical temperature sensors were randomly placed, some areas might not be monitored correctly, creating an inconsistency in the data collected, which would later negatively influence the virtual sensor. Therefore, the chosen geometric configurations contribute considerably to improving the performance of the machine learning model.

In conclusion, the chosen geometric configurations allowed the effective monitoring of the temperature in the space where the measurements were made, this can also be seen in *fig. 4,* it illustrates the web interface of the system. It displays the data measured by the sensors in real time.

Sensors Table

Date & Hour	Sensor 1 (°C)	Sensor 2 (°C)	Sensor 3 (°C)	Sensor 4 (°C)	Control Sensor (°C)	Virtual Sensor (°C)
2024-09-10 / 12:45	20.39	20.10	19.90	20.15	20.12	20.19
2024-09-10 / 13:00	20.51	20.30	20.15	20.40	20.35	20.41
2024-09-10 / 13:15	20.82	20.60	20.45	20.75	20.67	20.77
2024-09-10 / 13:30	21.14	20.95	20.80	21.00	21.02	21.07
2024-09-10 / 13:45	21.25	21.20	21.10	21.30	21.25	21.32
2024-09-10 / 14:00	21.60	21.55	21.30	21.45	21.50	21.56
2024-09-10 / 14:15	21.90	21.70	21.60	21.85	21.75	21.85
2024-09-10 / 14:30	22.27	22.05	21.90	22.15	22.10	22.19
2024-09-10 / 14:45	22.58	22.40	22.00	22.25	22.35	22.42
2024-09-10 / 15:00	22.79	22.65	22.30	22.55	22.58	22.67
2024-09-10 / 15:15	22.84	22.75	22.50	22.80	22.69	22.74
2024-09-10 / 15:30	23.04	22.85	22.70	23.00	22.88	22.94

Fig. 4. The web interface for monitoring sensors

In the web interface you can see in the first column the time at which the sensor data was collected, the following columns are those dedicated to the physical data sensors. After that, the control sensor column follows and finally in the last column you can see the response of the virtual sensor.

4. CONCLUSION

The presented project demonstrates the efficiency and utility of a virtual temperature sensor that uses data collected from physical sensors to train a machine learning algorithm. This approach represents an innovative solution within existing temperature monitoring systems.

One of the most important aspects of the project is the considerable cost reduction, especially for large temperature monitoring systems. This fact is due to the possibility of replacing some physical sensors with virtual sensors, thus reducing the number of physical sensors needed. Therefore, the use of virtual sensors leads to a significant decrease in the expenses related to the purchase, installation and maintenance of such a system. This aspect being very important in the industry where budget and space are limited.

The presented solution not only significantly reduces the costs associated with such a system, but also gives it increased flexibility. Temperature monitoring systems using virtual sensors are more flexible because they can measure temperature in locations inaccessible to physical sensors.

The use of polynomial regression within machine learning algorithms has proven optimal for temperature prediction, adapting well to non-linear data variations and providing accurate estimates based on data collected from physical sensors.

The developed web interface allows users to access and analyze data collected from sensors in real time. This aspect representing an improvement in the process of monitoring and managing data.

The presented system has high versatility, it can be used in various configurations depending on the need, for applications that require high precision the system can be adapted to a configuration with several sensors. On the other hand, if precision is not a crucial factor and the goal is to obtain an economical system, then a configuration with fewer sensors can be chosen. It should also be noted that continuous training of the machine learning model with historical and new data contributes significantly to increasing the accuracy of the virtual sensor predictions.

In conclusion, the use of a virtual temperature sensor based on machine learning algorithms represents an effective and innovative solution to improve the efficiency of temperature monitoring systems, while optimizing the costs and space required for these types of systems.

In further developments we aimed at using more advanced learning algorithms, changing sensors and improving the web interface in order to expand the scope of the system.

REFERENCES

[1] K. Vyas, S. Shukla, H. Dsouza, J. Chacko, D. D'Souza, V. Narnaware, *A Survey on Environment Monitoring using Sensor Networks*, Asian Journal of Convergence in Technology, Vol. VI, No. III, pp. 95-99, .2020

[2] M. Mansoor, I. Haneef, S. Akhtar, A. D. Luca, F. Udrea, *Silicon diode temperature sensors – A review of applications*, Sensors and Actuators A Physical, Vol. 232, pp. 63-74, May 2015.

[3] R. S. Diarah, C. Osueke, A. Adekunle, S. Adebayo, A. B. Aaron, O. O. Joshua, Types of Temperature Sensors, IntechOpen, October 2023.

[4] A. Brunello, A. Urgolo, F. Pittino, A. Montvay, A. Montanari, *Virtual Sensing and Sensors Selection for Efficient Temperature Monitoring in Indoor Environments*, Sensors, Vol. 21, 2728, April 2021.

[5] E. Ostertagová, *Modelling using polynomial regression*, Procedia Engineering, Vol. 48, pp. 500-506, December 2012.

[6] M. A. Alsheikh, S. Lin, D. Niyato, H. P. Tan, *Machine Learning in Wireless Sensor Networks: Algorithms, Strategies, and Applications*, IEEE Communications Surveys & Tutorials, Vol. 16, No. 4, pp. 1996-2018, May 2014.

[7] P. Ghule, M. Kambli, *Web Based Environment Monitoring System Using IOT,* 3rd International Conference on Trends in Electronics and Informatics, April 2019.

[8] S. Corbellini, E. D Francia, S. Grassini, L. Iannucci, L. Lombardo, M. Parvis, *Cloud based sensor network for environmental monitoring*, Measurement, October 2017.

[9] X. Cai, *The Development and Diverse Applications of Temperature Sensors in Different Temperature Environments*, Applied and Computational Engineering, Vol. 37, No. 1, pp. 141-148, February 2024.

[10] D. Fabiocchi, N. Giulietti, M. Carnevale, H. Giberti, *AI-Driven Virtual Sensors for Real-Time Dynamic Analysis of Mechanisms: A Feasibility Study*, Machines, Vol. 12, No. 4, pp. 257, April 2024.

Received: October 2024, Accepted: December 2024, Published: December 2024
Digital Object Identifier: https://doi.org/10.34302/CJEE/QSEG2220

DATA DRIVEN RULE-BASED PEAK SHAVING ALGORITHM FOR SCHEDULING REFRIGERATORS

Daniel **KWEGYIR**, Francis Boafo **EFFAH,** Daniel **OPOKU**, Emmanuel Asuming **FRIMPONG**
Department of Electrical and Electronic Engineering, Kwame Nkrumah University of Science and Technology, Kumasi, Ghana.
daniel.kwegyir@knust.edu.gh

Keywords: Thermostatically controlled loads, peak shaving, rule-based algorithm, dynamic flexibility

Abstract*: The increasing use of thermostatically controlled loads (TCLs) like refrigerators poses a significant challenge to the grid due to their potential to increase peak demand. This study introduces a novel rule-based peak-shaving algorithm to effectively manage these loads. The algorithm operates in two modes: day-ahead and real-time. In the day-ahead mode, Long Short-Term Memory (LSTM) neural networks are utilized to forecast demand and generation. A Parameter tuned Grey Wolf Optimizer (GWOP) is proposed and employed to determine the optimal generation for the initial timestep of the scheduling period. The GWOP is tuned using a brute-force grid search method to optimize its parameters. In the real-time mode, the algorithm dynamically adjusts refrigerator operations based on real-time mismatch calculations between predicted demand and generation. Dynamic flexibility thresholds are employed to determine the optimal operation of refrigerators during peak and off-peak periods. This approach aims to minimize energy consumption while maintaining thermal comfort. The algorithm's performance was evaluated using real-world data from the Spanish Transmission Service Operators (TSO). The results demonstrate a significant reduction in peak demand and total energy consumption. The algorithm with dynamic flexibility achieved a substantial 18.89% reduction in peak demand and a notable 12.12% decrease in total energy consumption.*

1. INTRODUCTION

As the world undergoes rapid urbanization and industrialization, electricity demand has surged, especially in developing countries where villages and towns are transforming into urban centers. This increased urbanization, coupled with global warming, has significantly raised the usage of thermostatically controlled loads (TCLs) such as refrigerators and air conditioners in households and offices [1] Air conditioners account for 14% to 20% of total energy consumption in buildings [2], while refrigerators consume about 10% [1].

The widespread use of TCLs poses a challenge to network stability, particularly in countries with insufficient power generation capacity [3,4]. This can lead to network stress, load shedding, demand-supply mismatches, and increased electricity costs. For consumers, this instability translates into higher costs of consumption, increased cost of economic activities and reduced comfort. Load shedding disrupts daily activities, while demand-supply mismatches drive up electricity prices as utilities purchase power at higher rates or invest in expensive peaking plants. Despite these potential challenges of wide usage of TCLs, they offer advantages for demand-side management (DSM) due to their thermal storage capabilities. Demand-side management strategies can leverage this flexibility to maintain grid stability, reduce operational costs, and ensure a reliable electricity supply. One effective strategy is peak demand shaving, which involves shifting TCL operations to off-peak periods to reduce stress on the power system during peak hours [5,6].

Peak demand shaving has been achieved using energy storage systems (ESS), DSM, and renewable energy integration [7]. Techniques such as optimal appliance scheduling and rule-based methods have been used, with significant work focused on using ESS and heaters for peak management. A simulation on an established building was conducted by [8] to determine the optimal DSM strategy from a building owner's perspective. The analysis revealed that power peak shaving of over 30% could be achieved without significantly impacting indoor conditions. Authors in [9] employed agent-based intelligence to flatten the thermal load of a group of buildings. The work done in [10] utilized a stable roommate’s algorithm to minimize the sum of the thermal requests for 28 buildings in England. However, these studies did not consider the network dynamics in forming the overall district heating thermal request. Authors in [11] used genetic algorithm optimization to minimize the maximum peak value, achieving a 10% reduction in overall thermal demand with minimal schedule variations. Authors in [12] applied the same algorithm for rescheduling, accounting for more significant modifications and the effects of indoor temperature changes. Authors in [13] presented a field test campaign on two district heating networks using the STORM controller, which reduced peaks by 7.5% – 34%, saving operational costs and reducing CO_2 emissions. Authors in [14] developed an active control strategy using a Model Predictive Control algorithm to maximize cogeneration plant profits by using buildings as storage capacity and selling electricity on the spot market at peak prices. Reinforcement Learning (RL) has been marginally used for directly addressing peak demand issues in district heating, typically applied to electric energy peak-shaving. The work done in [15] used an iterative Q-learning algorithm for energy arbitrage and peak-shaving of thermostatically controlled loads in a district heating system. Work done in [16] addressed thermal load management at the building level to reduce thermal peaks while maintaining user comfort. Demand-side management through multi-agent models to coordinate individual requests and reduce intra-daily fluctuations in thermal demand has also been proposed by [17].

In terms of rule-based approaches for peak shaving, limited research has been done. These mostly involve the use of ESS rather than TCLs. The study in [18] utilized a genetic algorithm (GA) to determine optimal inputs for peak shaving using rule-based method. The proposed optimal rule-based approach was applied to battery scheduling to shape peak. Although the method was effective, the rules employed to develop the proposed rule-based approach were complex and involved a lot of computation. Authors in [19] introduced a real-time battery management algorithm for peak demand shaving for commercial buildings. However, the work did not account for a dynamic demand limit that can be adjusted to meet various peak requirements for commercial buildings. Additionally, studies done in [20–22] evaluated peak shaving control with battery scheduling, considering a fixed demand limit. The fixed limits presented tight tolerance for the algorithms to operate leading to the creation of additional peaks and increased energy consumption. Again, the study carried out in [23] considered a dynamic demand limit for the peak shaving method. However, the method was specifically applied to Malaysian commercial buildings. Authors in [24] considered a battery controller with a fixed demand limit for peak shaving but did not maintain flexibility in day-to-day management.

Although a good amount of work has been done on peak shaving involving TCLs, ESS and renewables, there are some existing gaps. The literature mostly focuses on optimizing thermal loads and minimizing thermal requests without considering the network dynamics and their impact on overall thermal demand. Methods such as those using genetic algorithms (GA) for peak shaving (e.g., [11], and [25]) and the complex rule-based approaches for battery scheduling (e.g., study [18]) involve significant computational complexity which may not be feasible for real-time or resource-constrained environments. Many studies, including those by [14] have applied fixed demand limits or static control strategies. Even though some works (e.g., study [23]) considered dynamic demand limits, they were context-specific (e.g., applied to Malaysian commercial buildings) and did not offer a generalizable approach. This work proposes a simple rule-based peak-shaving algorithm with dynamic flexibility thresholds for scheduling refrigerators in real time. The proposed algorithm employs a two-level approach: day-ahead optimization and intra-day real-time adjustments. The research aligns with Goal 7 of the Sustainable Development Goals (SDGs), which aims to ensure access to affordable, reliable, sustainable, and modern energy for all by 2030 [26].

1.1. Research contributions

The research contributions of the paper are outlined below:

A novel rule-based peak shaving algorithm has been proposed to schedule refrigerators, to reduce peak demand. The rule-based algorithm simplifies decision-making by using predefined rules and dynamically adjustable parameters. This reduces the computational complexity of optimization-based approaches like genetic algorithms or multi-objective optimization problems. The proposed algorithm incorporates dynamic flexibility thresholds that adjust based on the system's real-time conditions. This allows for more flexible and efficient management of peak demand.

A data-driven estimation method using smoothing error is proposed to predict future generation in the rule-based algorithm for decision making. The smoothing error method is a statistical technique that uses historical data to smooth out irregularities and provide a more accurate prediction of future generations. This method is integrated into the rule-based algorithm to enhance its predictive capabilities and reduce the computational intensiveness of existing forecasting algorithms.

A simple discrete thermal model of a refrigerator is proposed to simulate the cooling and warming behaviour of refrigerators to test the proposed rule-based algorithm on a case study dataset.

1.2. Structure of paper

The rest of the paper is organized as follows: Section 2 discusses the proposed rule-based peak-shaving algorithm and its sub-control algorithms. Section 3 describes the proposed refrigerator thermal model for the study. The case study dataset used to validate the algorithm's performance is described in Section 4 in addition to the performance metrics employed to assess the algorithm's effectiveness. Section 5 presents the results and discussion. Conclusions and recommendations for future works are discussed in section 6.

2. DESCRIPTION OF PROPOSED RULE-BASED PEAK SHAVING FRAMEWORK AND ALGORITHM

This section presents the proposed data-driven, rule-based peak-shaving algorithm for refrigerators. The proposed framework within which the proposed rule-based peak shaving algorithm runs is given in *Fig. 2*. The framework is designed to run in day-ahead and real-time modes to reduce computational intensity**.** In the day-ahead, a forecast of demand and generation is done using long short-term memory (LSTM). The forecast output is used to identify possible peak and off-peak periods a day-ahead by analyzing the predicted demand against predicted generation using a simple logical algorithm. Again, to make decisions in real-time and reduce computational complexity, an optimization problem is defined to determine the possible optimum generation that the system operator can supply. This is solved with a proposed parameter tunned grey optimizer. The optimum generation is subsequently updated in real time using a smoothing error method.

The proposed rule-based algorithm then takes decision by comparing current demand with updated generation. If a mismatch is detected beyond a certain threshold, the algorithm adjusts the status of refrigerators by either turning them on or off to align demand with available generation capacity. This process continues until the mismatch falls within an acceptable limit. Details of these processes are discussed in the subsequent subsections.

2.1. Forecasting of Day-Ahead Demand and Generation with Long Short-Term Memory Neural Network.

Accurate forecasting of day-ahead demand and generation is crucial for optimizing grid operations and maintaining system stability especially in demand response programs. In this study, a Long short-term memory (LSTM) neural network is employed to forecast the day-ahead demand (P'_D) and generation (P'_g). This forecast serves as a fundamental input for the proposed rule-based peak shaving algorithm. The output from the forecast is used to forecast and identify the possible peak and off-peak periods a day-ahead within the real-time scheduling horizon. By analysing the forecasted demand in relation to the forecasted generation, the framework effectively pinpoint the periods of highest and lowest demand beyond a certain margin of the generation, which are classified as peak and off-peak, respectively. These classifications are subsequently fed into the peak shaving algorithm which enables the algorithm to make informed decisions regarding the refrigerator scheduling. This pre-emptive approach helps to reduce real-time computational complexities and enhance the overall efficiency of the algorithm's operations.

The LSTM architecture employed in the study is shown in *Fig. 1* [27]. It is modelled and operated with the forget gate, input gate, candidate cell state, cell state and output gate, described with (1) - (6), respectively. The forget gate (f_t) decides the information to remove from the cell state (c_t), the input gate (i_t) decides which values to update in the cell state, and the candidate cell state $(\widetilde{c_t})$ creates a vector of new candidates' values that could be added to the state, cell state updates by combining the old state and the now candidate values and the output gate (o_t) decides what the next hidden state (h_t) should be, based on the cell state.

$$f_t = \sigma(W_f.[h_{t-1}, x_t] + b_f \tag{1}$$

$$i_t = \sigma(W_i.[h_{t-1}, x_t] + b_i) \tag{2}$$

$$\widetilde{c_t} = \tanh\,(W_C.[h_{t-1}, x_t] + b_c) \tag{3}$$

$$c_t = f_t \odot c_{t-1} + i_t \odot \widetilde{c_t} \tag{4}$$

$$o_t = \sigma(W_o.[h_{t-1}, x_t] + b_o) \quad (5)$$

$$h_t = o_t \odot \tanh(c_t) \quad (6)$$

In the LSTM model, x_t is the input data, σ is the sigmoid function, tanh is the tangent function, *W* and *b* are weight and biases applied during training of the LSTM model respectively.

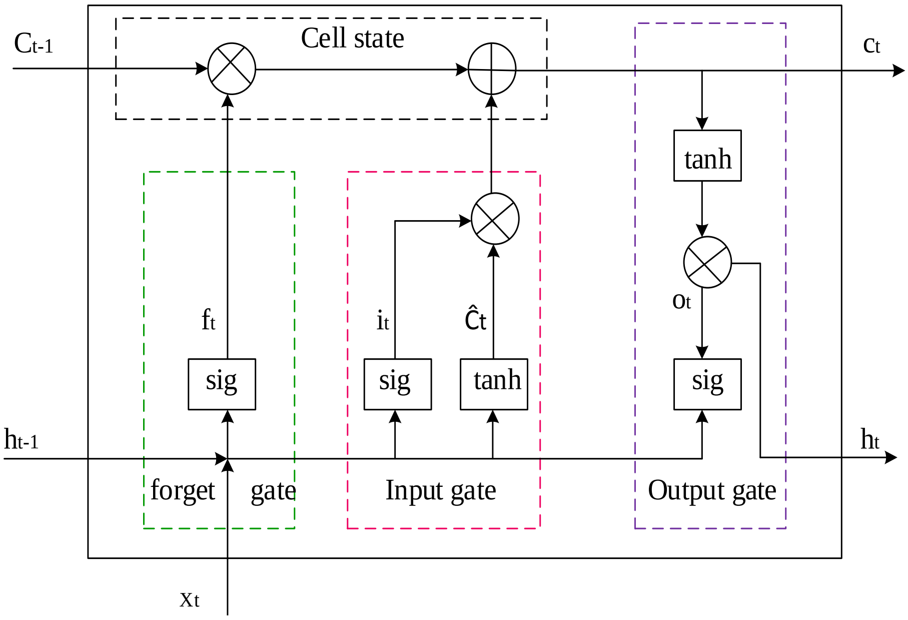

Fig. 1. Architecture of LSTM for forecasting day-ahead demand and generation

Historical time series data $X_t = [x_t^d, x_t^g, x_t^{temp}, x_t^a, x_t^s]$,, including demand (x_t^d), generation (x_t^g), ambient temperature (x_t^{temp}), solar irradiance (x_t^a), and solar power generation (x_t^s), are collected and preprocessed. These variables are critical determinants of demand and generation patterns, providing the LSTM with the necessary context to predict future values accurately. The data is first preprocessed to normalize the values, ensuring that all features contribute equally to the model's learning process. Missing data points are addressed through interpolation, and the dataset is divided into training, validation, and test sets to evaluate the model's performance. During training, the LSTM model is fed sequences of input data spanning multiple time steps, forming an input vector $X_t = [X_t - T + 1, X_t - T + 2, \ldots, X_t]$, or each time t, where T represents the sequence length. The model uses these sequences to predict the target variables—day-ahead demand and generation. The training process involves minimizing mean squared error (MSE) between the predicted demand and generation and their actual values in the training set. The model's parameters (weights and biases) are optimized using backpropagation. The learning rate, batch size, and number of epochs are carefully tuned to ensure convergence without overfitting. *Fig. 2* provides a flowchart for the method developed to forecast demand and generation.

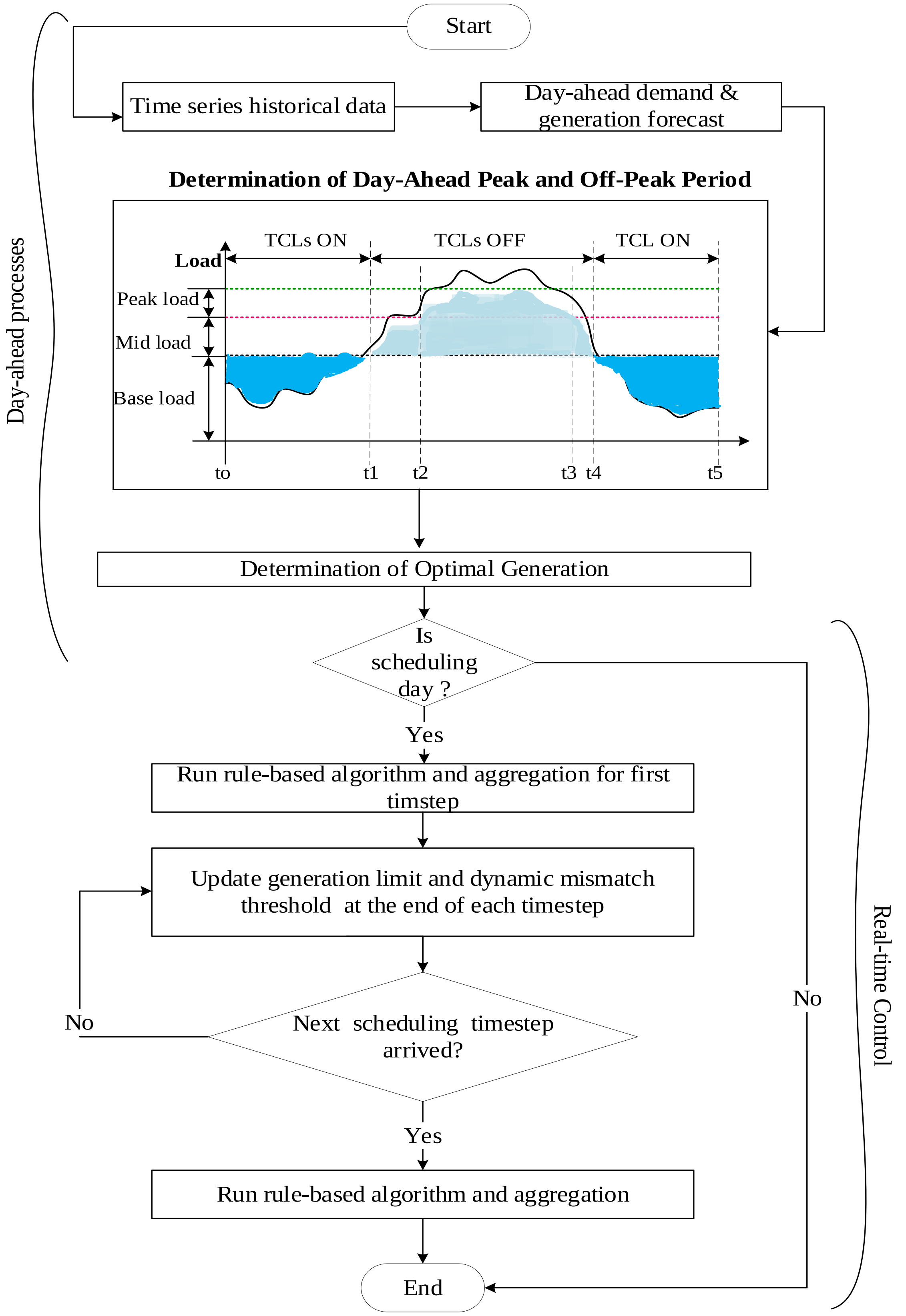

Fig. 2. Proposed data-driven rule-based peak shaving framework

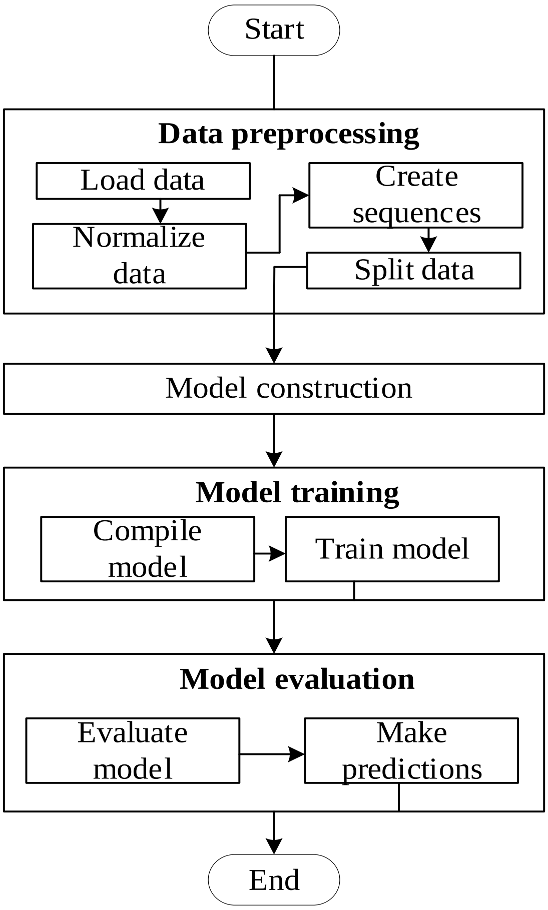

Fig. 3. Flow chart for forecasting demand and generation.

2.2.Determination of Optimal Generation for First Timestep of Scheduling Period

An optimal approach based on historical data is proposed in Algorithm 1 to estimate the potential generation the system operator can produce at the first timestep of the scheduling day (intraday). This enables the proposed rule-based peak-shaving algorithm to make proactive decisions in real-time during the scheduling period without rigorous continuous forecasting at each time step, thereby reducing intensive computation. The optimal generation is denoted as $\left(\mathrm{P}_{\mathrm{G}}^{\mathrm{l}}\right)$. By accurately estimating the first-time step generation day-ahead, the framework schedules the refrigerators at the first timestep using the proposed rule-based peak shaving algorithm before the actual generation data for the first timestep arrives. This initial $\left(\mathrm{P}_{\mathrm{G}}^{\mathrm{l}}\right)$ value is subsequently updated in real-time across the scheduling period using a smoothing error method in Algorithm 3.

To determine the first timestep value of $\left(\mathrm{P}_{\mathrm{G}}^{\mathrm{l}}\right)$ for the scheduling day, an optimization problem is formulated based on historical data on solar power, power demand, and battery discharge data. The objective function of the optimization is formulated in (8), with the optimal generation $\left(\mathrm{P}_{\mathrm{G}}^{\mathrm{l}}\right)$ as the decision variable. To solve for $\left(\mathrm{P}_{\mathrm{G}}^{\mathrm{l}}\right)$, a parameter-tuned grey wolf optimizer (GWOP) based on grid search tunning method is proposed in Algorithm 2. In this work battery discharge data was not considered in the testing since data was not available. The GWOP finds an optimal value of $\left(P_G^l\right)$ that makes the expression in (8) zero.

$$f\left(P_G^l\right) = \sum_{t=1}^{T} P_D(t) - \left(P_G^l(t) + P_{Solar}(t) + E_{disch}(t)\right) \quad (8)$$

In (8), P_D, P_{Solar} and E_{disch} are power demand, solar power, and battery discharge historical data respectively. The optimization problem is constrained by a lower limit $\left(P_G^l\,(lower\,)\right)$ and an upper limit $\left(P_G^l\,(upper)\right)$. The lower limit and upper limit are the minimum and maximum generation that can be supplied by the system operator. The pseudocode for determining the optimal generation $\left(P_G^l\right)$ is given in Algorithm 1.

Algorithm. 1. Determination of day-ahead optimal generation

Step	*Start determination of day-ahead optimal generation at first timestep*
1	*Inputs data: historical demand* (P_D), *historical solar power generation* (P_{solar})
2	*Output: Optimal generated power* (P_G^l)
3	*Solver initialization*
4	*Call objective function based on equation (4.22)*
5	*Set constraints:*
	Lower limit: $P_G^l\ (lower\ )$
	Upper limit: $P_G^l\ (upper)$
6	*Initialize solver and set its parameters*
7	*For* $i = 1$: *number of iterations*
8	*Solve for optimal solution*
9	$i = i + 1$
10	*End For*
11	*Output Optimal solution as* (P_G^l)
12	*End*

2.3. Proposed Parameter Tunned Grey Wolf Optimizer for Determination of Optimal Generation for First Timestep of Scheduling Period

In this paper, a grid search tunning method is employed to tune the classical grey wolf optimizer (GWO) to tune its parameters to enhance the algorithm's performance to solve for the optimal generation limit $\left(P_G^l\right)$. The classical grey wolf is explained below followed by the proposed parameter tuned grey wolf optimizer (GWOP).

2.3.1 Grey Wolf Optimization

The Grey Wolf Optimizer (GWO) [28] is based on the hunting behavior of grey wolves. Grey wolves are social predators that hunt in packs. This hunting behavior enables them to demonstrate a high degree of cooperation and strategy in their hunting behavior. Each wolf in the pack has a specific role. The alpha (best wolf) wolf leads the hunt, while other members follow its lead and assist in different capacities. The alpha (optimal solution) wolf is the dominant leader, responsible for deciding when and where to hunt. The beta wolf assists the alpha, taking on leadership roles when necessary. The beta wolves represent the second-best solution that help guide the search process and provide a search path for the alpha. Delta wolves assist in hunting and protection. They represent the third-best solution in the search space and support the alpha and beta in the optimization process.

2.3.2. Mathematical Modelling of Metaheuristic Processes of GWO

The hunting mechanism of the grey wolves is characterized by a coordinated and strategic approach that involves several phases. The phases have been discussed below.

Tracking, Chasing, and Approaching the Prey

The wolves track and chase prey, using their sense of smell and hearing to locate it. This is an approach to cautiously get as close as possible to the prey without being detected. The wolves (candidate solutions) encircle the prey by updating their positions based on the distance from the alpha, beta, and delta wolves using (10)**.**

$$\vec{D} = \left|\vec{C} \cdot \vec{X}_p(t) - \vec{X}(t)\right| \tag{9}$$

$$\vec{X}(t+1) = \vec{X}_p(t) - \vec{A} \cdot \vec{D} \tag{10}$$

In the update equation, $\vec{X}(t)$ is the position of a grey wolf, $\vec{X}_p(t)$ is the position of the prey and $\vec{A}$ and $\vec{C}$ are coefficients vectors calculated with (11) and (12).

$$\vec{A} = 2\vec{a} \cdot \vec{r}_1 - \vec{a} \tag{11}$$

$$\vec{C} = 2 \cdot \vec{r}_2 \tag{12}$$

Pursuing and Encircling the Prey

Once the prey is close enough, wolves pursue and encircle it, cutting off escape routes and exhausting the prey. The algorithm simulates encircling behavior by having each wolf adjust its position relative to the positions of the alpha, beta, and delta wolves. This is mathematically modelled to ensure the wolves move closer to the optimal solution. The update equation for this phase is given in (16).

$$\vec{X}_1 = \vec{X}_\alpha - \vec{A}_1 \cdot \left|\vec{C}_1 \cdot \vec{X}_\alpha - \vec{X}\right| \tag{13}$$

$$\vec{X}_2 = \vec{X}_\beta - \vec{A}_2 \cdot \left|\vec{C}_2 \cdot \vec{X}_\beta - \vec{X}\right| \tag{14}$$

$$\vec{X}_3 = \vec{X}_\delta - \vec{A}_3 \cdot \left|\vec{C}_3 \cdot \vec{X}_\delta - \vec{X}\right| \tag{15}$$

$$\vec{X}(t+1) = \frac{\vec{X}_1 + \vec{X}_2 + \vec{X}_3}{3} \tag{16}$$

Attacking the Prey

The wolves attack once the prey is exhausted or cornered, ensuring a successful hunt. The algorithm converges on the optimal solution. As iterations proceed, the search space is exploited more intensively, refining the candidate solutions to converge on the best solution.

2.3.3. Proposed Parameter Tunned Grey Wolf Optimizer

The GWO has been applied to successfully solve numerous optimization problems, however, its performance is sensitive to the algorithm's control parameters; alpha (α), beta (β) and delta (δ) which affects the exploration and exploitation abilities of the wolves. The grid search tunning method is employed to systematically tune the GWO to enhance its exploration and exploration to solve for $\left(P_G^l\right)$. The grid search methods employ a brute-force method to tune the hyper-parameters of the GWO. In the tunning method, a finite set of values for alpha (α), beta (β) and delta (δ) are generated. The GWO is then evaluated for every possible combination of these values. The combination that yields the best performance is selected as the optimal set of parameters finding the optimal value.

2.4. Update of Optimal Generation

In the proposed rule-based peak shaving algorithm, the optimal generation for the second timestep to the end of the scheduling period (T) is updated by accounting for the discrepancy between the actual generation at the first timestep and the historical data on the optimal generation over a time window (w). The proposed update approach utilizes a smoothing error technique [29]. To update the optimal generation $\left(P_G^l\right)$ for the next timestep in the intra-day's decision-making, the error between the actual generation $\left(P_G^{actual}\right)$ at the first timestep and the optimal generation a day before $\left(P_G^l(t-24)\right)$ is calculated over a predefined time window size (w) and averaged. The average error is then added to the first timestep optimal generation $\left(P_G^l(t)\right)$ to determine the next timestep's generation limit for the scheduling period. The update of the optimal generation limit $\left(P_G^l\right)$ is done using (17) - (19). The error (e_t) between the actual generation at the beginning of the current day $\left(P_G^{actual}(t)\right)$ and the optimal generation determined the day before $\left(P_G^l(t-24)\right)$ is calculated using (17). Historical data on this error is built over the forecasting period to calculate a smoothing error for real-time updates to the optimal generation limit $\left(P_G^l\right)$.

$$e_t = P_G^{actual}(t) - P_G^l(t-24) \tag{17}$$

The smoothing error over a predefined time window size w, is calculated as an average error using (18).

$$\overline{e_t} = \frac{1}{w}\sum_{i=t-w+1}^{t} e_i \tag{18}$$

The optimal generation limit is then updated by (19). The pseudocode in Algorithm 3 provides the detailed steps for the error calculation and generation $\left(P_G^l\right)$ update.

$$P_G^{updated}(t) = P_G^l(t-24) + \overline{e_t} \tag{19}$$

of $\left(P_G^l\right)$. The proposed tunning algorithm is given in Algorithm 2.

Algorithm. 2. Proposed algorithm for tunning grey wolf optimizer

Step	*Start parameter tunning of grey wolf optimizer (GWOP)*
1	*Inputs:*
2	*Parameter ranges for alpha* $\alpha \in [\alpha_{min}, \alpha_{max}]$ *with step size* $\Delta\alpha$
3	*Parameter ranges for alpha* $\beta \in [\beta_{min}, \beta_{max}]$ *with step size* $\Delta\beta$
4	*Parameter ranges for alpha* $\delta \in [\delta_{min}, \delta_{max}]$ *with step size* $\Delta\delta$
5	*Number of iterations T, population size (P), objective function* $f(x)$
6	*Outputs:* α_{opt}, β_{opt}, δ_{opt} *and* f_{best}
7	*For* $i = 1{:}T$
8	*For alpha* $\alpha \in [\alpha_{min}, \alpha_{min} + \Delta\alpha, \dots, \alpha_{max}]$*:*
9	*For alpha* $\beta \in [\beta_{min}, \beta_{min} + \Delta\beta, \dots, \beta_{max}]$*:*
10	*For alpha* $\delta \in [\delta_{min}, \delta_{min} + \Delta\delta, \dots, \delta_{max}]$*:*
11	*Evaluate GWO with current combinations of* α,β *and* δ
12	*Calculate fitness score* $f_{current}$
13	*End*
14	*End*
15	*End*
16	*If* $f_{current} < f_{best}$
17	*Set* $f_{best} = f_{current}$
18	*Set* $\alpha_{opt} = \alpha$
19	*Set* $\beta_{opt} = \beta$
20	*Set* $\delta_{opt} = \delta$
21	*End if*
22	*End for*
23	*End grid search*

2.5. Identification of Day-Ahead Peak and Off-Peak Periods

In the proposed rule-based peak shaving algorithm, a logical algorithm is proposed in Algorithm 4 to identify peak and off-peak periods within day-ahead forecasted demand data $(\mathrm{P}_{\mathrm{D}}')$ relative to day-ahead forecasted generation $(\mathrm{P}_{\mathrm{g}}')$. In the proposed algorithm, peak periods are identified based on the condition that $\mathrm{P}_{\mathrm{D}}'(\mathrm{t}) > \mathrm{P}_{\mathrm{g}}'(\mathrm{t})$ by a certain margin above the system operator's base load. The base load is taken as the optimal generation $\left(\mathrm{P}_{\mathrm{G}}^{\mathrm{l}}\right)$ across the scheduling period in this work. The algorithm iterates through the dataset at each timestep (t) to identify periods where the demand exceeds generation by the chosen margin. The identified periods are labelled as peak durations and are characterized by their start and end times. This approach allows the algorithm to proactively make decisions in real-time based on the forecasted generation rather than waiting for actual generation data to arrive.

Algorithm. 3. Update of optimal generation in real-time

Step	***Start update of generation limit***
1	*Inputs Data*
2	*Define window size (w)*
	Get day-before optimal generation $\left(P_{G(day-before)}^{l}\right)$
	Get actual generation $\left(P_{G}^{actual}\right)$
3	*Output*
4	*Updated generation limit* $\left(P_{G(updated)}^{l}\right)$
5	*Smooth error calculation based on averaging window approach*
6	*While current timestep < last timestep of data*
7	*When a new timestep's generation data arrives:*
8	*Calculate error with equation (17)*
9	*If length of error history < w:*
10	*Append error to error history*
11	*Else*
12	*Remove oldest error from history*
13	*Append new error to error history*
14	*End If*
15	*Update generation limit with equation (19)*
16	*Increment current timestep by 1*
17	*Output updated generation* $\left(P_{G}^{l}\right)$
18	***End***

Algorithm. 4. Determination of peak and off-peak periods

Step	*Start identification of peak and off-peak durations*
1	*Initialization*
2	*Get forecasted demand data* (P_D')
3	*Get forecasted generation data* (P_g').
4	*Initialize peak durations as an empty list (to store peak durations)*
5	*Set start time to 0 (to track peak starts)*
6	*Loop through demand data*
7	*For* $i = 1$ *to length* (P_D'):
8	*If* $P_D'(i) > P_g'(i)$ *by margin:*
9	*If start time == 0, Set start time to* i*(mark peak start)*
10	*Else if* $P_D'(i) < P_g'(i)$:
11	*If start time!= 0, Calculate peak duration and save it in peak*
12	*durations list, the set start time to 0 (reset peak start)*
13	*End If*
14	*End If*
15	*End for*
16	*Handle end-of-Series Peak*
17	*If start time != 0, calculate final peak duration*
18	*End If*
19	*Output*
20	*Print peak durations as "Start Time, End Time" pairs.*
21	*End*

2.6.Proposed Rule-Based Peak Shaving Algorithm

This section discusses the proposed rule-based peak-shaving algorithm for scheduling refrigerators. The algorithm aims to monitor real-time power demand (P_D) and generation (P_G) data to take decisions to align demand with available generation capacity based on predefined rules. The proposed algorithm is shown in *Fig. 4*. The peak and off-peak period controls are given in Algorithm 5, 6, and 7. The decision-making process of the proposed algorithm primarily involves establishing decision making parameter, peak and off-peak period control. During peak periods, the algorithm prioritizes turning OFF refrigerators to shave the peak demand. Conversely, during off-peak periods, the algorithm turns ON refrigerators to balance the overall demand. The algorithm's dynamic adjustment to real-time conditions is a critical feature. It updates the optimal generation $\left(P_G^1\right)$ and other decision parameters based on the latest data received to ensure the power system's responsiveness to changing network conditions. Details of the controls within the algorithm are discussed below.

2.6.1. Decision Making Table

The control table for decision-making in the algorithm is given in Table 1. The table summarizes the conditions under which the algorithm operates and the corresponding action to be taken to aggregate the refrigerators. The variable P_D is the demand at current timestep and Y is the mismatch threshold. The mismatch threshold determines the acceptable level of power mismatch during peak and off-peak period control. The variable current refrigerator status ($S_{i,t}^{b}$) is the status of the i^{th} refrigerator at time t, where 0 indicates OFF and 1 indicates ON. The variable new refrigerator status ($S_{i,t}^{n}$) is the new status of the i^{th} refrigerator at time t determined by the algorithm`s control logic. Finally, the action description shows the action taken by the algorithm based on the current system conditions.

Table 1. Peak and Off-Peak Decision-Making Conditions

Condition Check	**Control Condition**	**Current Refrigerator Status ($S_{i,t}^{b}$)**	**New Refrigerator Status ($S_{i,t}^{n}$)**	**Action Description**
Peak period && $(P_D') > (P_G^l)$	If mismatch threshold (Y) is exceeded	0 (OFF)	0 (OFF)	Maintain TCL OFF
Peak period && $(P_D') > (P_G^l)$	If mismatch threshold (Y) is exceeded	1(ON)	0 (OFF)	Turn OFF TCL
Peak period && $(P_D') \leq (P_G^l)$	If mismatch threshold (Y) is not exceeded	Any	Any	Maintain status
Off peak period && $(P_D') < (P_G^l)$	If mismatch threshold (Y) is exceeded	1 (ON)	1 (ON)	Maintain TCL ON
Off peak period && $(P_D') < (P_G^l)$	If mismatch threshold (Y) is exceeded	0 (OFF)	1 (ON)	Turn ON TCL
Off peak period && $(P_D') \geq (P_G^l)$	If mismatch threshold (Y) is not exceeded	Any	Any	Maintain status

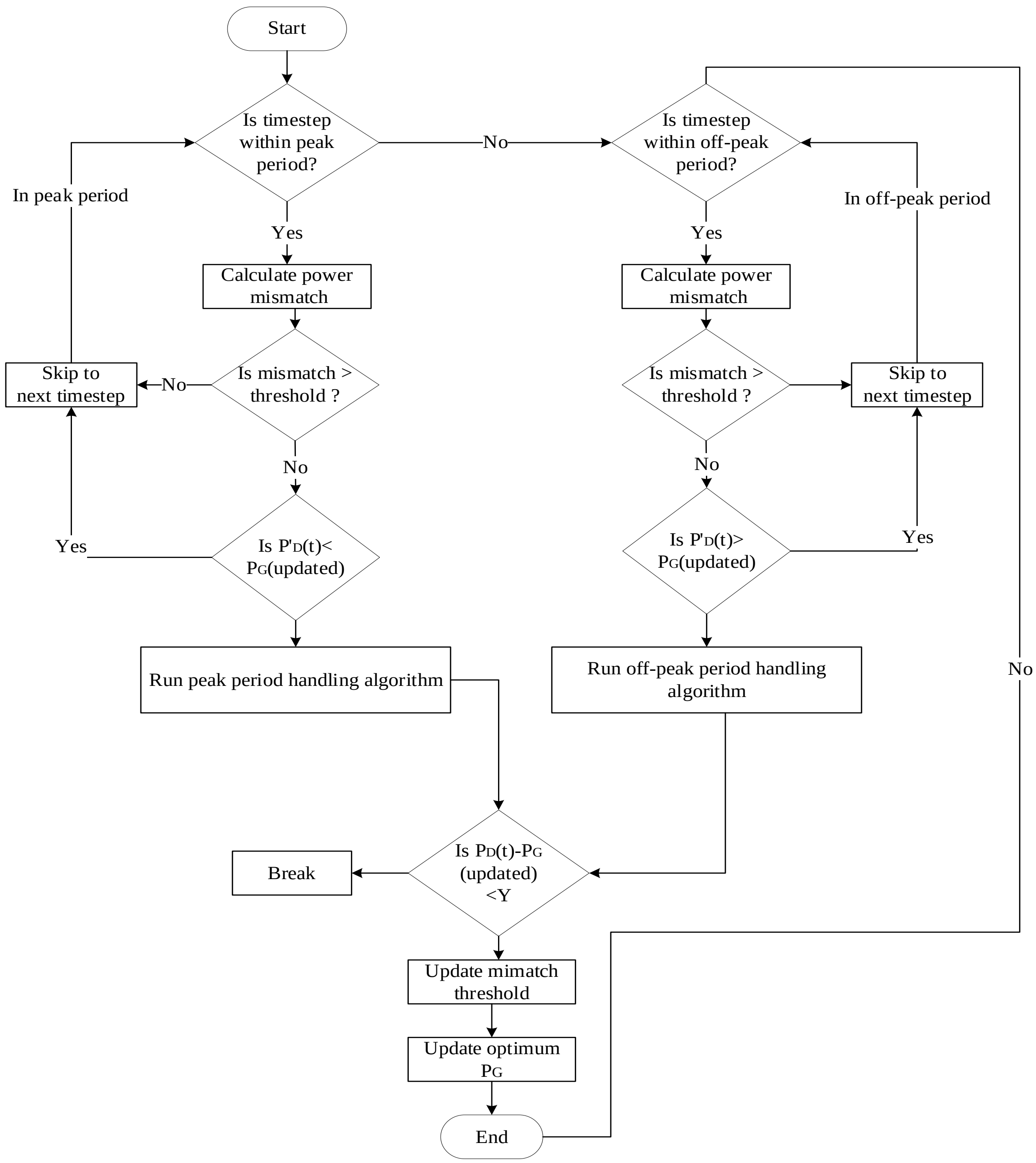

Fig. 4.Proposed rule-based peak shaving algorithm

2.6.2. Algorithm Initialization

The proposed rule-based peak shaving algorithm is initialized as follows:

Step	*Initialize algorithm*
1	*Get real-time demand* $P_D(t)$
2	*Get history of previous optimal generation* $\left(P_G^l\right)$
3	*Run LSTM forecast and output* (P_D') *and* (P_g')*,*
4	*Run Algorithm 1: output optimal generation at first timestep* $\left(P_G^l\right)$

Step	*Initialize algorithm*
5	*Run Algorithm 4 on step 3: output peak and off-peak periods.*
6	*Get critical temperature ($\theta_{critical}$)*
7	*Get current compartment temperatures of all refrigerators: θ_c*

2.6.3. Peak Period Handling

During the peak periods, the algorithm's rules are designed to reduce the demand to stay close to the real time generation (P_G) by turning OFF as many refrigerators as possible. The number of refrigerators to be turned off by the algorithm is limited by the mismatch threshold (Y) . This action helps to shave the peak demand and prevent grid overload. The peak period control and decision-making steps are provided in Algorithm 5.

Algorithm 5. Peak period handling

Step	*Start peak period control and aggregation*
1	*If t is within a peak period:*
2	*Calculate power mismatch*=$\left\|P'_D(t) - P^l_G(t)\right\|$
3	*If $P'_D(t) > P^l_G(t)$,*
4	*If current power mismatch >Y: If no skip to the next timestep.*
5	*Else*
6	*For i=1 to N:* // start aggregation
7	*If $S^b_{i,t}$=0, set new status: $S^n_{i,t}$=$S^b_{i,t}$*
8	*Else set new status: $S^n_{i,t}$=0*
9	*Begin warming of refrigerator i*
10	*Start waiting time for next schedule of refrigerator i*
11	*Update aggregated demand: $P_D(t) = P_D(t) + S^n_{i,t}.P_r$*
12	*If $\left\|P_D(t) - P'_g(t)\right\| < Y$, break* // stop aggregating
13	*Update mismatch threshold Y*
14	*Update $P^l_G(t)$*

2.6.4. Off-Peak Period Handling

During the off-peak periods, the algorithm's rules are designed to turn ON refrigerators to increase the demand by utilizing the excess generation and preventing generation from going to waste. The off-peak period controls and decision-making steps are provided in *Algorithm 6.*

Algorithm 6. Off-peak period handling

Step	*Start off-peak period control and aggregation*
1	*If t is within off-peak period:*

Step	*Start off-peak period control and aggregation*
2	*Calculate power mismatch*= $\left\|P_D'(t) - P_G^l(t)\right\|$
3	*If* $P'_D(t) < P_G^l(t)$
4	*If current power mismatch >Y: If no skip to the next timestep.*
5	*Else*
6	*For i=1 to N: // (start aggregation)*
7	*If* $S_{i,t}^b$*=1, set new status:* $S_{i,t}^n$=$S_{i,t}^b$
8	*Else set new status:* $S_{i,t}^n$*=1*
9	*Begin cooling of refrigerator i*
10	*Start waiting time for next schedule of refrigerator i*
11	*Update aggregated demand:* $P_D(t) = P_D(t) + S_{i,t}^n.P_r$
12	*If* $\left\|P_D(t) - P_g'(t)\right\| < Y$*, break // (stop aggregating)*
13	*Update mismatch threshold Y*
14	*Update* $P_G^l(t)$

2.6.5. Proposed Dynamic Mismatch Threshold

In the proposed rule-based algorithm, a dynamic adjustment is employed based on system conditions to adjust the mismatch threshold. A dynamic adjustor based on sigmoid function is proposed to smoothly adjust the mismatch threshold at each timestep based on the difference between actual generation at the previous timestep ($P_G(t-1)$) and actual demand at the previous timestep ($P_D(t-1)$). The dynamic thresholding method ensures that the algorithm adapts to changing system conditions more effectively to maintain a balance between demand and supply while avoiding the pitfalls of too tight or too loose thresholds. The sigmoid function provides smooth and continuous adjustment to prevent abrupt changes in refrigerator operation that could lead to instability. The dynamic adjustment is formulated in equation (20).

$$Y(t) = Y_{base}(t) + \frac{1}{1+e^{-k\left(P_G(t-1)-P_D(t-1)\right)}} \tag{20}$$

where $Y(t)$ is the mismatch threshold and $Y_{base}(t)$ is the base mismatch selected by the system operator.

3. SIMULATION OF REFRIGERATOR COOLING AND WARMING BEHAVIOUR FOR TESTING PROPOSED RULE-BASED ALGORITHM

The discrete thermal model of a vapor compressor refrigeration system (VCRS) is employed to simulate cooling and warming of refrigerator compartment in the testing phase of the proposed rule-based peak shaving algorithm. The discrete models of the warm-up and cool-down of the refrigerator compartment are given by equation (21) and (22) respectively.

$$\theta_c(t+\Delta t) = \left(1 - \frac{\Delta t}{C_L.R_i}\right).\theta_c(t) + \frac{\Delta t}{C_L.R_i}.\theta_a\,(t) \tag{21}$$

$$\theta_c(t+\Delta t) = \left(1 - \frac{\Delta t}{C_L.R_i}\right).\theta_c(t) + \frac{\Delta t}{C_L.R_i}.\theta_a\,(t) + \frac{\Delta t}{C_L.R_e}.\theta_e(t) \tag{22}$$

where θ_c is the cabinet temperature at time t, C_L is the heat storage capacity of cabinet, θ_a is the ambient temperature at time t, R_i is the thermal resistance of the insulation and θ_e is the evaporator temperature.

The cooling and warming behavior of the refrigerator is achieved with the controls in equation (23) where $\theta_{critical}$ is the set threshold temperature. In the control, when $S = 1$, the refrigerator is turned ON and when $S = 0$ the refrigerator is turned OFF.

$$\theta_c(t+\Delta t) = \begin{cases} \text{Cool}, & \theta_c(t) > \theta_{critical}, S = 1 \\ \text{Warm}, & \theta_c(t) < \theta_{critical}, S = 0 \end{cases} \tag{23}$$

The refrigerator power consumption is modelled according to equation (24). The refrigerator consumes rated power (P_r) when the compressor is ON and 0 when OFF.

$$P_{in}(t) = \begin{cases} 0 & , \ S = 0 \\ P_r & , \ S = 1 \end{cases} \tag{24}$$

The total power drawn by all the refrigerators within a timestep is given by equation (25).

$$P_{total}(t) = \sum_{t=1}^{T}\sum_{i=1}^{N} S_{i,t}P_{in}^{i}(t) \tag{25}$$

Algorithm 7 is used to simulate the thermal behavior of the refrigerators.

Algorithm 7. Simulation of thermal behavior of multiple refrigerators

Step	*Start simulation of thermal behavior of TCLs*	
1	*Inputs*	
2	*Number of refrigerators (N)*	
3	$\theta_c^0 = [1, \dots, M]$	*// initial compartment temperature*
4	$\theta_a^0 = [1, \dots, M]$,	*// initial ambient temperature*
5	$\theta_e^0 = [1, \dots, M]$,	*// initial evaporator temperature*

Step	*Start simulation of thermal behavior of TCLs*
6	Δt *// time step*
7	*Initialize all other parameters:* θ_{ref}, P_r
8	*Simulation duration (T).*
9	*Outputs:*
10	θ_c, *Pin*
11	*Main loop*
12	*For* Δt *=1: T*
13	*For* $i = 1\text{: }M$
14	*If* $\theta_c(t) < (\theta_{ref})$
15	*Turn OFF*
16	*Update compartment temperature using equation (22)*
17	*Update refrigerator power (Pin) using equation (24)*
18	*Else*
19	*Turn ON*
20	*Update compartment temperature using equation (23)*
21	*Update refrigerator power (Pin) using equation (24)*
22	*End if*
23	*End for*
24	*End for*
25	*End algorithm*

4. DESCRIPTION OF CASE STUDY SYSTEM, SIMULATION AND TESTING

The study utilizes a dataset from Spanish Transmission Service Operators (TSO) spanning four years (2015-2018) [30] to test the proposed rule-based peak-shaving algorithm for scheduling refrigerators. The data includes electricity consumption, pricing, generation, and weather information. A unique aspect of this dataset is its granularity, offering hourly records for each variable. This level of detail is essential for accurately modelling and simulating the dynamic behavior of electricity demand and supply, which is critical for the study. The generation data comprises renewable energy sources i.e, solar and conventional energy sources i.e, thermal and geothermal. This mix of generation types allows for rigorous performance testing of the algorithm in a realistic and varied energy landscape.

All generation sources except solar are combined as total generation to determine the optimal generation limit using Algorithm 1. The data mainly consist of hourly demand data. To test the scheduling ability of the algorithm, 30% of the hourly demand at each timestep is simulated as refrigerator demand to be scheduled. In the testing, 1000 refrigerators are simulated to represent the 30% demand at each hour. The unit maximum power consumption when a refrigerator is ON across the 48-hour period is given in *Fig. 5*. The day-ahead demand and generation forecast is done for December 30, 2018, and December 31, 2018. The optimal generation is determined for the first hour of December 30, 2018.

Simulations were conducted on an Intel(R) Core (TM) i7-6600U CPU @ 2.60GHz 2.81 GHz with 20.0 GB (19.9 GB usable) RAM using MATLAB simulation software. The parameters for simulating the rule-based peak shaving algorithm are given in Table 2.

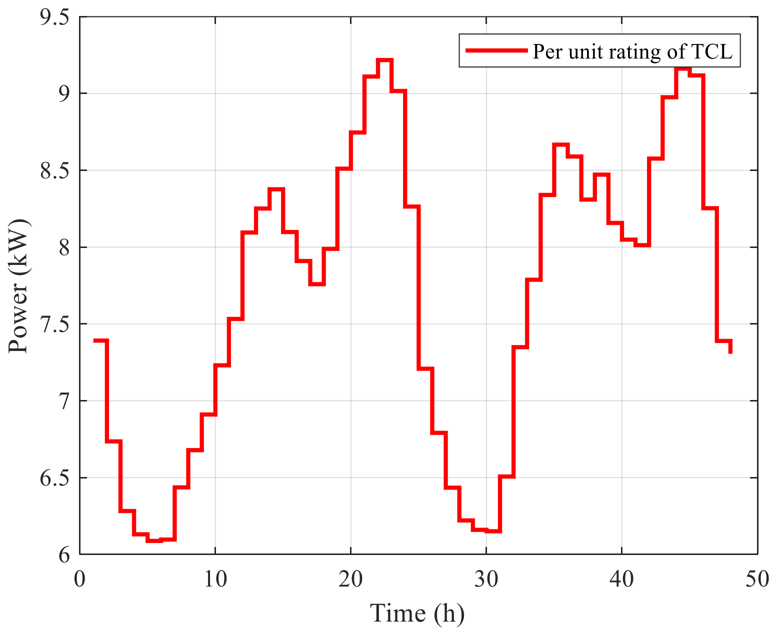

Fig. 5. Per unit rating of TCLs when ON for scheduling

Table 2. Simulation parameters

Parameter	**Value**
P_G^l (lower)	0 MW
P_G^l (upper)	Maximum historical generation
T	48 hours
Refrigerator power rating when ON (P_r)	Based on Figure 4
Mismatch sensitivity levels	0 kW, 500 kW, dynamic mismatch
Population size of PGWO	100
Number of refrigerators	1000
Baseline status	Randomly generated
$\theta_{critical}$	5 °C
C_L	1000 kW/°C
R_i	0.98°C/kW
R_e	0.09°C/kW
Waiting time	20 Minutes
Margin of identifying peak periods	Demand exceeds generation by 5%

Parameter	**Value**
Base load for mismatch	500 kW
θ_e	Randomly simulated around -2℃
θ_a	Real weather data for scheduling period
Initial compartment temperature of refrigerators	Randomly generated
Batch Size	64
Epochs	1000
Learning rate	0.01

4.1. Performance Evaluation Metrics

To assess the performance of the proposed peak-shaving algorithm, the following metrics are considered.

4.1.1. Peak Demand Reduction

Peak demand reduction measures the extent to which the algorithm successfully reduces the highest electricity demand peaks during peak periods. It is calculated as the percentage decrease in peak demand after implementing the algorithm compared to the initial peak demand given by equation (26).

$$\text{Peak Demand Reduction (\%)} = \frac{(\text{Peak Demand Before} - \text{Peak Demand After})}{\text{Peak Demand Before}} \quad (26)$$

4.1.2. Energy Consumption

The energy consumption analysis compares the total energy consumption before and after implementing the peak demand shaving algorithm. It assesses whether the algorithm effectively manages energy usage and leads to overall energy savings. Equation (27) is used to calculate the energy consumption increase or decrease.

$$\text{Energy Consumption Increase (\%)} = \frac{(\text{Total Energy Consumption After} - \text{Total Energy Consumption Before})}{\text{Total Energy Consumption Before}} \quad (27)$$

4.1.3. Demand-Supply Mismatch

Demand-supply mismatch metric quantifies the deviation between electricity demand and supply at any given time. It evaluates how well the algorithm balances demand and supply to minimize mismatches. This is calculated with equation (28) is used to calculate the demand and supply mismatch at each timestep during the scheduling period.

$$\text{Demand} - \text{Supply Mismatch} = |\text{Demand} - \text{Supply}| \tag{28}$$

4.1.4. TCL Status Changes

The TCL status changes metric refers to the frequency and magnitude of changes in the operating status (ON/OFF) of the TCLs in response to the algorithm's instructions. It evaluates the algorithm's ability to manage appliance operation efficiently while maintaining user comfort and minimizing disruptions. Equation (29) is used to calculate the total status changes of TCL during the scheduling period.

$$\text{Total Status Changes} = \sum_{i=1}^{N} \left|S_{i,t}^{b} - S_{i,t}^{n}\right| \tag{29}$$

5. RESULTS AND DISCUSSIONS

This section presents discussions of the results obtained from implementing the proposed rule-based peak demand-shaving algorithm. The discussions focus on the impact of different scenarios of flexibility levels on the proposed algorithm’s effectiveness in peak shaving. The effectiveness is assessed based on peak demand reduction, total energy consumption reduction, refrigerator switching frequency, and the average mismatch between demand and supply. The results highlight the benefits and limitations of offering strict and dynamic flexibility into optimizing demand response programs.

5.1. Scenario 1: Strict Flexibility Threshold

The results of applying the proposed rule-based peak shaving algorithm with strict mismatch threshold is presented in Table 3. This scenario is simulated to assess the algorithm’s effectiveness for matching the demand exactly to the available generation at each timestep.

Table 3. Performance Metrics for Strict Flexibility Threshold Scenario

Performance Metric	**Value**
Peak Demand Before	30619.00 MW
Peak Demand After	25107.83 MW
Peak Demand Reduction	18.00%
Total Energy Consumption Before	1228351.00 MWh
Total Energy Consumption After	1088485.3778 MWh
Energy Consumption decrease	11.39%
Total Status Changes in Refrigerators	13000 times
Average Demand-Supply Mismatch	693.99 kW

Following the application of the proposed peak shaving algorithm, the peak demand was reduced from 30,619.00 MW to 25,107.83 MW, representing a significant reduction of 18.00%. This notable decrease demonstrates the algorithm's effectiveness in managing and lowering peak electricity demand, which is crucial for mitigating the need for costly peaking power plants, alleviating stress on the power grid, and potentially reducing electricity costs for consumers. Additionally, the total energy consumption decreased by 11.39%, from 1,228,351.00 MWh to 1,088,485.38 MWh. This substantial reduction in energy consumption, a key indicator of the algorithm's effectiveness, highlights its ability to manage peak demand and achieve significant overall energy savings, which can contribute to more sustainable energy use and lower operational costs. However, the algorithm's strict mismatch threshold led to a high switching quantified in terms of total status changes in the refrigerators, with 13,000 status changes recorded. Each status change reflects a switch between ON and OFF states. While this frequent switching indicates the algorithm's responsiveness to maintain a tight balance between supply and demand, it may also pose a risk of increased wear and tear on the appliances, potentially reducing their lifespan and increasing maintenance costs. The average demand-supply mismatch was 693.99 kW, reflecting the deviation between scheduled demand and available generation over the scheduling period. This mismatch arises due to the inherent difficulty in perfectly aligning demand with supply at every timestep, especially under the high variability of system conditions and the frequent switching triggered by the stringent mismatch threshold.

Fig. 6 provides a detailed comparison of the scheduled demand, unscheduled demand, actual generation, and the updated optimum generation over the scheduling period, illustrating the performance of the peak shaving algorithm under the strict flexibility threshold.

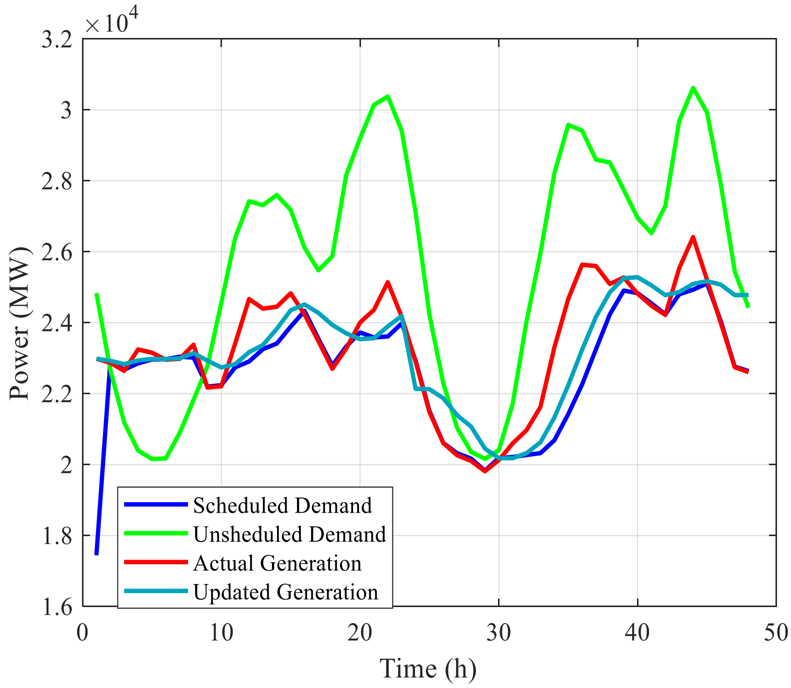

Fig. 6. Comparison of scheduled and unscheduled demand under strict flexibility threshold

5.2. Scenario 2: Base load as flexibility Threshold

The results of applying the proposed rule-based peak shaving algorithm with a flexibility threshold of 500 kW across the scheduling period is presented in Table 4. This scenario is simulated to assess the algorithm's effectiveness under some level of flexible threshold.

Table 4. Performance Metrics for Base Load Flexibility Threshold Scenario

Performance Metric	**Value**
Peak Demand Before	30619.00 MW
Peak Demand After	24852.08 MW
Peak Demand Reduction	18.83%
Total Energy Consumption Before	1228351.00 MWh
Total Energy Consumption After	1081227.60 MWh
Energy Consumption decrease	11.98%
Total Status Changes in Refrigerators	3006 times
Average Demand-Supply Mismatch	1118.64 kW

After applying the peak shaving algorithm with a base load flexibility threshold, the peak demand was reduced from 30,619.00 MW to 24,852.08 MW, achieving an 18.83% reduction. This result shows a slightly higher peak demand reduction compared to the strict flexibility threshold scenario, with an additional reduction of 0.83%. This suggests that incorporating a flexibility limit can enhance the algorithm's effectiveness in reducing peak demand, allowing for more adaptable management of power usage. The total energy consumption after scheduling decreased by 11.98%, from 1,228,351.00 MWh to 1,081,227.60 MWh. This is a marginal improvement over the strict flexibility threshold scenario, indicating that the use of a base load flexibility threshold not only maintains peak demand reduction but also results in greater overall energy savings. Moreover, the total number of status changes for refrigerators dropped significantly to 3,006. This is a substantial reduction compared to the strict flexibility scenario, indicating less frequent switching of TCLs. The decrease in switching events implies reduced wear and tear on appliances, potentially extending their lifespan and lowering maintenance costs, thereby highlighting the financial benefits of incorporating a flexibility threshold. However, the average demand-supply mismatch in this scenario increased to 1,118.64 kW. This higher mismatch suggests that while the flexibility allowance effectively reduces peak demand and energy consumption, it comes at the expense of a less precise alignment between demand and supply. This misalignment could lead to more frequent periods of surplus or deficit, impacting the overall efficiency of energy distribution.

Fig.7 compares the scheduled demand, unscheduled demand, actual generation, and updated optimum generation over the scheduling period, showcasing the impact of using a base load flexibility threshold on the peak shaving algorithm's performance.

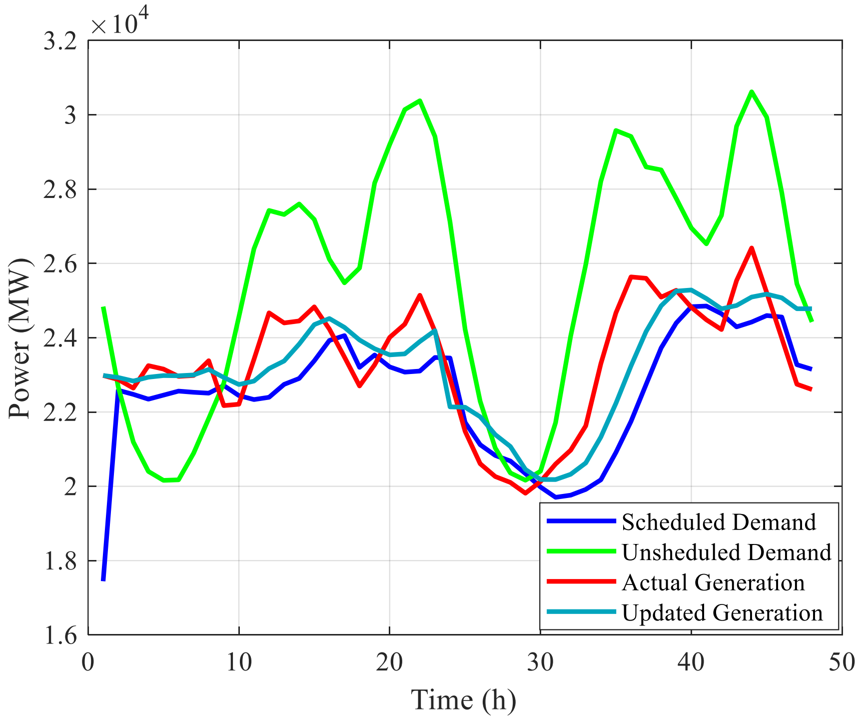

Fig. 7. Comparison of scheduled and unscheduled demand under base load flexibility threshold

5.3.Scenario 3: Proposed Dynamic Flexibility Threshold

The performance of the proposed rule-based peak shaving algorithm with dynamic flexibility thresholds is presented in Table 5. This scenario evaluates the effectiveness of the algorithm when the mismatch thresholds change dynamically based on system conditions.

Table 5. Performance Metrics for Dynamic Flexibility Threshold Scenario

Performance Metric	**Value**
Peak Demand Before	30619.00 MW
Peak Demand After	24845.19 MW
Peak Demand Reduction	18.89%
Total Energy Consumption Before	1228351.00 MWh
Total Energy Consumption After	1079489.82 MWh
Energy Consumption decrease	12.12%
Total Status Changes in Refrigerators	3006 times
Average Demand-Supply Mismatch	1012.41 kW

Applying dynamic flexibility thresholds led to a peak demand reduction of 18.89%, lowering the peak demand from 30,619.00 MW to 24,845.19 MW. This is the highest peak demand reduction observed across all scenarios, surpassing the strict mismatch threshold (18.00%) and the 500 kW flexibility threshold (18.83%). The results indicate that dynamic flexibility thresholds enhance the algorithm's ability to manage and reduce peak demand more effectively by adapting to real-time system conditions. Total energy consumption decreased by 12.12%, from 1,228,351.00 MWh to 1,079,489.82 MWh. This represents the most significant reduction in energy consumption among all scenarios, outperforming both the strict mismatch threshold (11.39%) and the 500 kW flexibility limit (11.98%). The greater decrease in energy consumption under the dynamic threshold scenario underscores the improved overall energy efficiency achieved by adjusting the thresholds dynamically. The total number of status changes for refrigerators was 3,006, consistent with the 500 kW flexibility threshold scenario and significantly lower than the 13,000 status changes observed in the strict mismatch threshold scenario. This consistency in status changes indicates that both the dynamic and base load flexibility thresholds can maintain refrigerator operations more reliably, reducing frequent switching and potentially lowering wear and tear and maintenance costs. The average demand-supply mismatch for the dynamic flexibility threshold scenario was 1,012.41 kW. While this is lower than the mismatch observed with the 500 kW flexibility limit (1,118.64 kW), it is higher than the mismatch in the strict mismatch threshold scenario (693.99 kW). This suggests that although the dynamic flexibility thresholds improve peak shaving and energy efficiency, it introduces a certain level of mismatch between demand and supply. However, the mismatches are within acceptable ranges.

Fig. 8 compares the scheduled demand, unscheduled demand, actual generation, and updated optimum generation over the scheduling period, illustrating the impact of dynamic flexibility thresholds on the performance of the peak shaving algorithm.

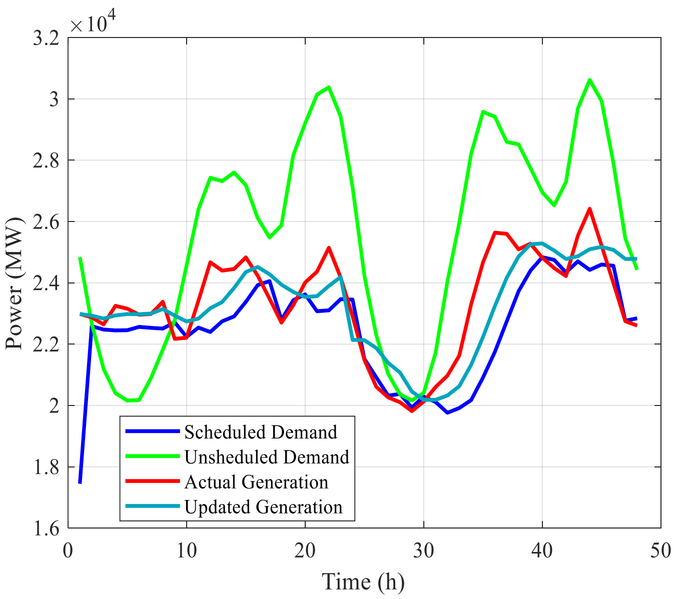

Fig. 8. Comparison of scheduled and unscheduled demand under dynamic flexibility threshold

Fig. 9 provides a comparison of scheduled demand across the three flexibility threshold scenarios: strict (0 kW), base load, and dynamic flexibility thresholds. The mismatches across the three flexibility threshold scenarios: strict (0 kW), base load, and dynamic flexibility thresholds are compared in *Fig 10*. This comparison helps to highlight how each approach impacts demand scheduling, particularly during peak periods.

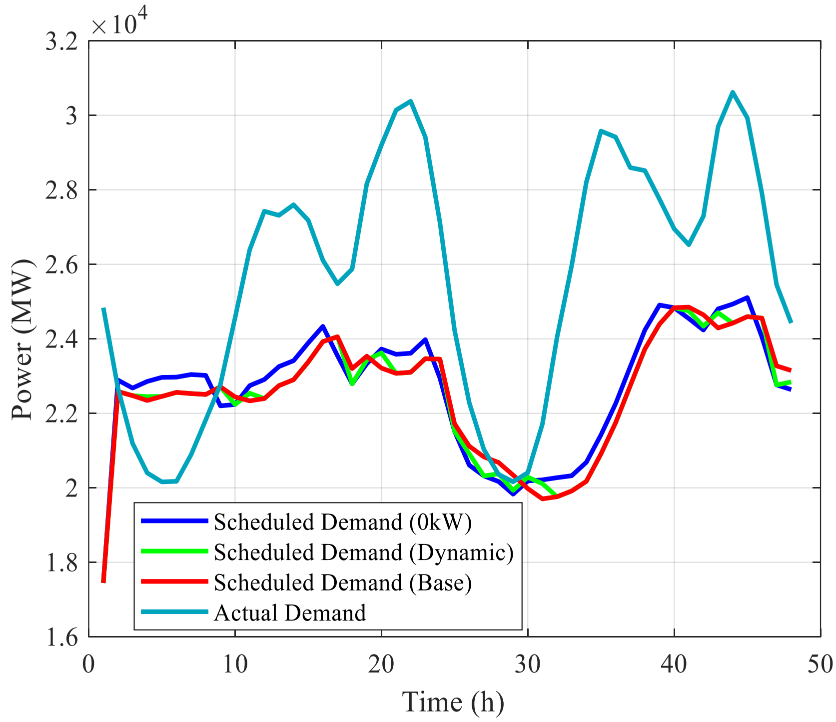

Fig. 9. Comparison of scheduled demand for different scenarios

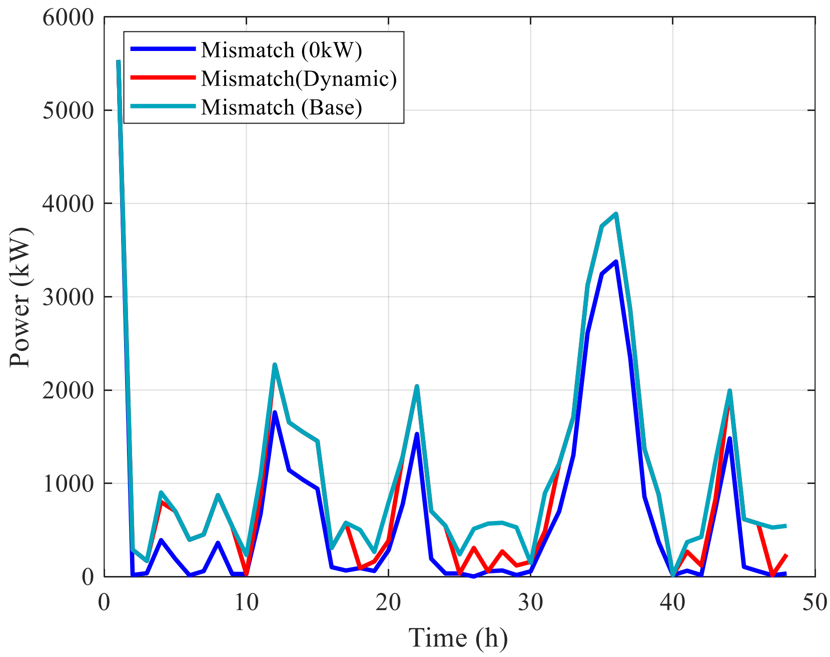

Fig. 70. Comparison of supply and demand mismatch after scheduling for different scenarios

Under the strict scenario (0 kW flexibility), demand must precisely match generation, resulting in higher scheduled and peak demand with a low average mismatch (693.99 kW) but many status changes (13,000). The base load scenario (500 kW static flexibility) smooths out demand, lowering peak demand (24,852.08 MW) and status changes (3,006) at the cost of a higher mismatch (1,118.64 kW). The dynamic scenario, which adjusts thresholds in real-time, achieves the lowest scheduled and peak demand (24,845.19 MW) and reduces energy consumption by 12.12%, striking a better balance with a moderate mismatch (1,012.41 kW).

6. CONCLUSION AND FUTURE WORK

This study introduced a novel rule-based peak shaving algorithm with a dynamic mismatch threshold designed to schedule refrigerators for peak demand management and maintain system stability in environments with limited generation capacity. The proposed algorithm operates within a framework that enables decision-making in both day-ahead and real-time scenarios to effectively schedule refrigerators. By utilizing historical data on demand and generation, the algorithm determines an optimal generation limit that system operators can aim to meet a day in advance. This generation limit is a key decision variable that informs the rules developed for the peak shaving algorithm, which adjusts the status of refrigerators in real time. Additionally, the algorithm uses day-ahead demand forecasts to anticipate peak and off-peak periods, allowing for dynamic adjustments that reduce peak demand during high-load periods and optimize excess generation usage during low-load times, thereby enhancing grid stability and balance. The effectiveness of the algorithm was evaluated using network data from the Spanish Transmission Service Operators (TSO) over four years, under various flexibility threshold scenarios. The analysis revealed significant insights into how different flexibility allowances impact demand response performance. The main findings are summarized as follows:

Strict No-Flexibility Threshold: In this scenario, where there is no flexibility allowance (0 kW mismatch threshold), the algorithm led to a notable increase in peak demand by 2.93% and a rise in total energy consumption by 6.73%. This outcome demonstrates the drawbacks of a strict mismatch threshold, which necessitates frequent switching of TCLs. This frequent switching increases operational stress and energy consumption, although it efficiently utilizes excess generation during off-peak periods. The results also indicate that while this approach minimizes the average demand-supply mismatch, it imposes challenges in precisely matching supply and demand, especially under stringent conditions.

Base Load Flexibility Threshold: With a higher mismatch allowance of 1000 kW, the peak demand showed a slight increase of 0.08%, and total energy consumption rose by 3.97%. While this scenario offers some improvement over the strict no-flexibility condition by reducing the total status changes and operational stress on appliances, it still results in higher energy use. The increased flexibility helps better manage demand-supply alignment and reduce the frequency of TCL switching, suggesting that some flexibility can alleviate operational inefficiencies while still making effective use of excess generation during off-peak times.

Dynamic Flexibility Threshold: The dynamic mismatch threshold scenario yielded the best results, with a substantial reduction in peak demand by 4.25% and a slight decrease in total energy consumption by 0.59%. This indicates that incorporating dynamic flexibility can significantly optimize demand response and enhance energy efficiency. The algorithm also reduced the total status changes in TCLs to 3,000, highlighting decreased switching frequency and less operational stress on appliances. The higher average demand-supply mismatch in this scenario suggests a well-balanced approach to managing demand and supply, effectively accommodating variations in grid conditions.

The comparative analysis across these scenarios demonstrates the benefits of integrating dynamic flexibility into demand response strategies. The dynamic approach not only reduces peak demand and total energy consumption but also minimizes the operational impact on appliances, as evidenced by fewer status changes. These findings underline the potential for dynamic flexibility to enhance the effectiveness of demand response programs.

Future research will focus on incorporating dynamic flexibility thresholds into demand response programs that integrate renewable energy sources. By dynamically adjusting flexibility thresholds based on real-time network conditions, such programs can significantly improve peak demand management and energy efficiency. Utilities and policymakers are encouraged to adopt flexible demand response strategies that adapt to changing conditions, leveraging the benefits of dynamic flexibility to ensure a more resilient and efficient power grid.

REFERENCES

[1] *How much electricity does a refrigerator, dishwasher, and an electric car use? n.d.* https://blog.se.com/sustainability/2023/01/24/how-much-electricity-does-a-refrigerator-dishwasher-and-an-electric-car-use-we-did-the-math/ (accessed June 15, 2024).

[2] *The Future of Cooling – Analysis - IEA n.d.* https://www.iea.org/reports/the-future-of-cooling (accessed June 15, 2024).

[3] United States Population 2024 (Live) n.d. https://worldpopulationreview.com/countries/united-states-population (accessed June 15, 2024).

[4] Ghana Population (2024) - Worldometer n.d. https://www.worldometers.info/world-population/ghana-population/ (accessed June 15, 2024).

[5] Akasiadis C, Chalkiadakis G, *Mechanism Design for Demand-Side Management*. IEEE Intell Syst 2017; 32: 24–31. https://doi.org/10.1109/MIS.2017.6.

[6] Machado B, Castro MF, Bragança L. *European Union legislation for demand-side management and public policies for demand response*. IOP Conf Ser Earth Environ Sci 2019; 225:012064. https://doi.org/10.1088/1755-1315/225/1/012064.

[7] Rana MM, Atef M, Sarkar MR, Uddin M, Shafiullah GM. *A Review on Peak Load Shaving in Microgrid—Potential Benefits, Challenges, and Future Trend*. Energies (Basel) 2022;15. https://doi.org/10.3390/en15062278.

[8] Kristian M. *Demand response of heating and ventilation within educational office buildings*. n.d.

[9] Li H, Wang SJ. *Load Management in District Heating Operation*. Energy Procedia 2015; 75:1202–7. https://doi.org/10.1016/j.egypro.2015.07.155.

[10] Sweetnam T, Spataru C, Barrett M, Carter E. *Domestic demand-side response on district heating networks*. Building Research & Information 2019 ;47:330–43. https://doi.org/10.1080/09613218.2018.1426314.

[11] Guelpa E, Barbero G, Sciacovelli A, Verda V. *Peak-shaving in district heating systems through optimal management of the thermal request of buildings*. Energy 2017 ;137:706–14. https://doi.org/10.1016/j.energy.2017.06.107.

[12] Brundu FG, Patti E, Osello A, Giudice M Del, Rapetti N, Krylovskiy A, et al. *IoT Software Infrastructure for Energy Management and Simulation in Smart Cities*. IEEE Trans Industr Inform 2017;13:832–40. https://doi.org/10.1109/TII.2016.2627479.

[13] Van Oevelen T, Vanhoudt D, Johansson C, Smulders E. *Testing and performance evaluation of the STORM controller in two demonstration sites*. Energy 2020; 197:117177. https://doi.org/10.1016/j.energy.2020.117177.

[14] Vanhoudt D, Claessens BJ, Salenbien R, Desmedt J. *An active control strategy for district heating networks and the effect of different thermal energy storage configurations*. Energy Build 2018; 158:1317–27. https://doi.org/10.1016/j.enbuild.2017.11.018.

[15] Claessens BJ, Vanhoudt D, Desmedt J, Ruelens F. *Model-free control of thermostatically controlled loads connected to a district heating network*. Energy Build 2018; 159:1–10. https://doi.org/10.1016/j.enbuild.2017.08.052.

[16] Li H, Wang SJ. *Load Management in District Heating Operation*. Energy Procedia 2015; 75:1202–7. https://doi.org/10.1016/j.egypro.2015.07.155.

[17] Wernstedt F, Davidsson P, Johansson C. *Demand side management in district heating systems*. Proceedings of the 6th international joint conference on Autonomous agents and multiagent systems, New York, NY, USA: ACM; 2007, p. 1–7. https://doi.org/10.1145/1329125.1329454.

[18] Hossain J, Saeed N, Manojkumar R, Marzband M, Sedraoui K, Al-Turki Y. *Optimal peak-shaving for dynamic demand response in smart Malaysian commercial buildings utilizing an efficient PV-BES system*. Sustain Cities Soc 2024;101. https://doi.org/10.1016/j.scs.2023.105107.

[19] Mohamed AAR, Best RJ, Liu X, Morrow DJ. *A Comprehensive Robust Techno-Economic Analysis and Sizing Tool for the Small-Scale PV and BESS*. IEEE Transactions on Energy Conversion 2022; 37:560–72. https://doi.org/10.1109/TEC.2021.3107103.

[20] Pimm AJ, Cockerill TT, Taylor PG. *The potential for peak shaving on low voltage distribution networks using electricity storage*. J Energy Storage 2018; 16:231–42. https://doi.org/10.1016/j.est.2018.02.002.

[21] Mahmud K, Hossain MJ, Town GE. *Peak-Load Reduction by Coordinated Response of Photovoltaics, Battery Storage, and Electric Vehicles*. IEEE Access 2018; 6:29353–65. https://doi.org/10.1109/ACCESS.2018.2837144.

[22] Greenwood DM, Wade NS, Taylor PC, Papadopoulos P, Heyward N. *A Probabilistic Method Combining Electrical Energy Storage and Real-Time Thermal Ratings to Defer Network Reinforcement*. IEEE Trans Sustain Energy 2017; 8:374–84. https://doi.org/10.1109/TSTE.2016.2600320.

[23] Manojkumar R, Kumar C, Ganguly S, Gooi HB, Mekhilef S, Catalão JPS. *Rule-Based Peak Shaving Using Master-Slave Level Optimization in a Diesel Generator Supplied Microgrid*. IEEE Transactions on Power Systems 2023; 38:2177–88. https://doi.org/10.1109/TPWRS.2022.3187069.

[24] Riffonneau Y, Bacha S, Barruel F, Ploix S. *Optimal Power Flow Management for Grid Connected PV Systems With Batteries*. IEEE Trans Sustain Energy 2011; 2:309–20. https://doi.org/10.1109/TSTE.2011.2114901.

[25] Brundu FG, Patti E, Osello A, Giudice M Del, Rapetti N, Krylovskiy A, et al. *IoT Software Infrastructure for Energy Management and Simulation in Smart Cities*. IEEE Trans Industr Inform 2017; 13:832–40. https://doi.org/10.1109/TII.2016.2627479.

[26] THE 17 GOALS | Sustainable Development n.d. https://sdgs.un.org/goals (accessed September 4, 2024).

[27] Abbasimehr H, Shabani M, Yousefi M. *An optimized model using LSTM network for demand forecasting*. Comput Ind Eng 2020; 143:106435. https://doi.org/10.1016/j.cie.2020.106435.

[28] Mirjalili S, Mirjalili SM, Lewis A. *Grey Wolf Optimizer*. *Advances in Engineering Software* 2014; 69:46–61. https://doi.org/10.1016/j.advengsoft.2013.12.007.

[29] Violeau D, Fonty T. *Calculating the smoothing error in SPH*. Comput Fluids 2019; 191:104240. https://doi.org/10.1016/j.compfluid.2019.104240.

[30] *Hourly energy demand generation and weather* n.d. https://www.kaggle.com/datasets/nicholasjhana/energy-consumption-generation-prices-and-weather/data (accessed June 15, 2024).

Received: November 2024, Accepted: December 2024, Published: December 2024
Digital Object Identifier: https://doi.org/10.34302/CJEE/JAYJ9255

ASPECTS REGARDING THE CORRELATION OF THE NUMBER OF SERIES/PARALLEL-CONNECTED PHOTOVOLTAIC MODULES WITH THE INVERTER INPUTS

Alina Tatiana **NEAMȚ**[1], Liviu **NEAMȚ**[2]**,** Olivian **CHIVER**[2]**,** Eleonora **POP**[2]**,** Mirela **ILIA**[3]**,** Ciprian **BUD**[4]
[1] *"Anghel Saligny" Technical College Baia Mare, Romania,* [2] *Technical University of Cluj-Napoca, Romania,* [3] *Distribuție Energie Electrică Romania,* [4] *Transelectrica Romania*
alina23_tatiana@yahoo.com

Keywords: Photovoltaic cells, temperature, irradiance, efficiency, safety

Abstract: *Because the photovoltaic system performance is significantly influenced by the environmental factors, particularly temperature and irradiance, a right correlation between the number of series/parallel-connected photovoltaic modules with the inverter inputs must be achieved to guarantee the safety of all components and the system in its entirety, and a high efficiency in electrical energy production. This paper addresses these issues and presents the results in a very simple and illustrative manner very easily to be implemented in the design procedure of a photovoltaic system,*

1. INTRODUCTION

According to the data published by the National Energy Regulatory Authority; Transelectrica - the transmission and system operator in Romania and the Romanian distribution companies, the number of prosumers at the end of October 2024 exceeded 175,000, and the installed power of the photovoltaic systems (PVS) among them was over 2 GW [1]. This explosion, from practically zero, occurred in 4 years and the pace continues to accelerate. This results in the need for increased attention to detail on the part of PVS designers and installers.

In this paper we point out the management of the correlation between the number of series/parallel-connected photovoltaic modules with the inverter inputs in terms of voltage and current.

2. METHODOLOGY

The main parameters of the PV modules used for the above analysis are:

- *Electrical data* under standard test conditions (STC), irradiance G_{STC} = 1000 W/m^2, spectrum AM 1.5 and cell temperature T_{STC} = 25°C: Nominal max. power (P_{max}), Opt. operating voltage ($V_{mp\text{-}STC}$), Opt. operating current ($I_{mp\text{-}STC}$), Open circuit voltage ($V_{OC\text{-}STC}$), Short circuit current ($I_{sc\text{-}STC}$)
- *Temperature characteristics* under nominal module operating temperature (NMOT), irradiance of 800 W/m^2, spectrum AM 1.5, ambient temperature 20°C, wind speed 1 m/s: Temperature coefficient of *Voc* (λ_V) expressed in %/°C, Temperature coefficient of I_{sc} (λ_I) expressed in %/°C, Nominal module operating temperature (NMOT).

The main parameters of the Inverter used for the above analysis are:

- Max. input voltage ($V_{max\ Inv}$), MPPT operating voltage range ($V_{min\ MPPT}$, $V_{max\ MPPT}$), Rated input voltage ($V_{r\ MPPT}$), Max. input current per MPPT ($I_{max\ MPPT}$), Max. short-circuit current ($I_{sc\ MPPT}$).

Due to the major impact of the environmental parameter (irradiance and ambient temperature T_a) on the PV modules output parameters, the simplified approach consisting of comparing the STC parameter with the inverter input ones is not an option.

The relations that express the above variabilities are presented in detail in [2-10] and are applied for the "worst case scenarios" that affect the PV module parameters, based on the actual slope, β and azimuth, γ, namely:

- for current and for operating voltage: that moment of a summer day with the greatest irradiance incident on the PV modules and the higher temperature of the modules which lead to the maximum values: $I_{sc\ max}$ and $I_{mp\ max}$ and to the minimum one: $V_{mp\ min}$:

$$I_{\mathrm{sc\,max}} = I_{\mathrm{sc}}\,(G_{max}, T_{max}) \; = \; I_{\mathrm{sc-STC}}\,\left[1 \,+\, \frac{\lambda_I}{100}\cdot(T_{max} - 25)\right] G_{max}/G_{STC} \tag{1}$$

$$I_{\mathrm{mp\,max}} = I_{\mathrm{mp}}\,(G_{max}, T_{max}) \; = \; I_{\mathrm{mp-STC}}\,\left[1 \,+\, \frac{\lambda_I}{100}\cdot(T_{max} - 25)\right] G_{max}/G_{STC} \tag{2}$$

$$V_{mp\,\mathrm{min}} = \; V_{mp}\,(T_{max}) = V_{mp-STC}\left[1 + \frac{\lambda_V}{100}(T_{max} - 25)\right] \tag{3}$$

$$T_{max} = T_{a\,max} + (NMOT - 20)G_{max}\,/800 \tag{4}$$

- for voltage: that moment of a winter day with the lowest irradiance incident on the PV modules and the lowest temperature which goes to the maximum value for $V_{OC\,max}$.

$$T_{min} = T_{a\,min} + (NMOT - 20)G_{min}\,/800 \tag{5}$$

$$V_{OC\,\max} = V_{OC}\,(T_{min}) = V_{OC-STC}\left[1 + \frac{\lambda_V}{100}(T_{min} - 25)\right] \tag{6}$$

The relations that must be fulfilled for a proper correlation between the number of series/parallel-connected photovoltaic modules with the inverter inputs are:

- maximum number of series connected PV modules, Ns_{max}:

$$Ns_{max} \leq V_{max-Inv}/V_{OC\,max} \tag{7}$$

- minimum number of series connected PV modules, Ns_{min}:

$$Ns_{min} \geq V_{min\,MPPT}/V_{mp\,min} \tag{8}$$

- maximum number of parallel connected PV arrays, Np_{max}:

$$Np_{max} \leq I_{max\,MPPT}/I_{mp\,max} \tag{9}$$

$$Np_{max} \leq I_{sc\,MPPT}/I_{sc\,max} \tag{10}$$

Inequalities (7-10) must be satisfied in all circumstances, but verifying them for the above mentioned “worst case scenarios” is sufficient for a good coordination between the PV module and inverter.

Another relation that ensures the optimum input d.c. voltage in the inverter, in terms of its efficiency, is very useful when the designer must select from multiple PV modules connection available. It should be noted that this condition is not mandatory to comply with.

$$N_{opt} \cong V_{r\,MPPT}/V_{mp\,STC} \tag{11}$$

3. CASE STUDY FOR ROMANIA

The minimum and maximum values for G and T_a result from Photovoltaic Geographical System (PVGIS) [11]. As a case study, see *fig. 1* and *2* for Romania.

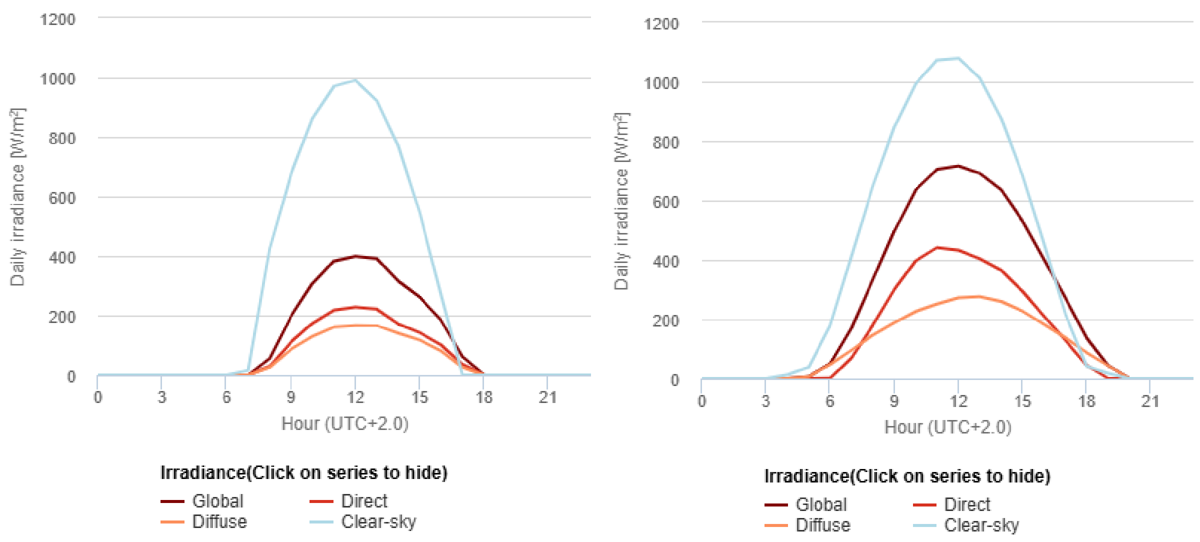

a. December *b. June*

Fig. 1. Daily average irradiance for the North of Romania

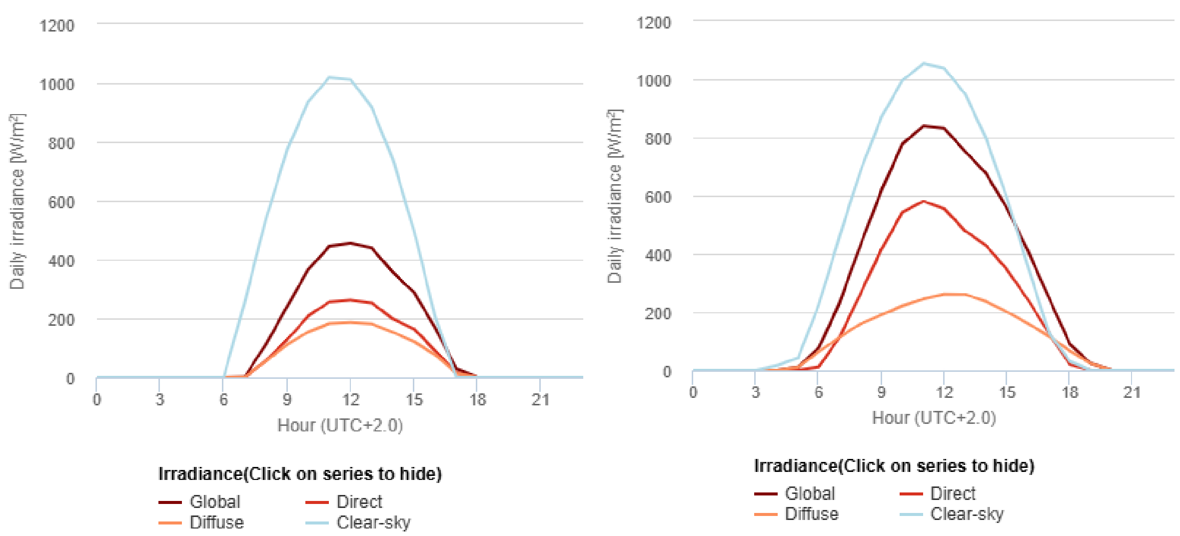

a. December *b. Jne*

Fig. 2. Daily average irradiance for the South of Romania

In Romania, the maximum values of clear-sky irradiance (considered for the G_{max} evaluation) and diffuse irradiance (considered for the G_{min} evaluation), have a variation of aprox. 100 W/m^2 between north and south and between winter and summer.

The values for environmental parameters for Romania taken into calculation are: G_{max} = 1100 W/m^2, $T_{a\ max}$ = 40°C, G_{min} = 100 W/m^2, $T_{a\ min}$ = -25°C.

Considering the usual ranges for the thermal parameters of the PV modules: $NOMT \in$ (40, 50) °C, $\lambda_V \in$ (-0.5, -0.25) %/°C and $\lambda_I \in$ (0.04, 0.08) %/°C, the graphical interpretation of $I_{sc\ max} / I_{sc\ STC} = I_{mp\ max} / I_{mp\ STC}$, $V_{mp\ min} / V_{mp\ STC}$ and $V_{OC\ max} / V_{OC\ STC}$ are depicted in *fig. 3* and *fig. 4*.

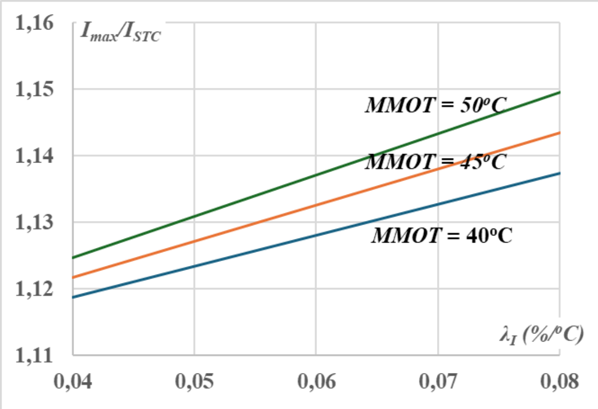

Fig. 3. $I_{sc\ max} / I_{sc\ STC} = I_{mp\ max} / I_{mp\ STC}$ *variations for different thermal parameters of PV modules*

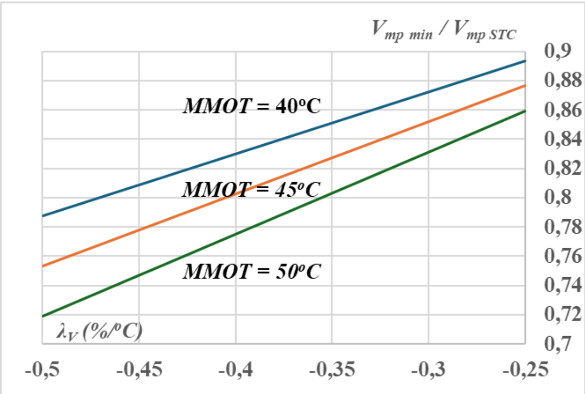

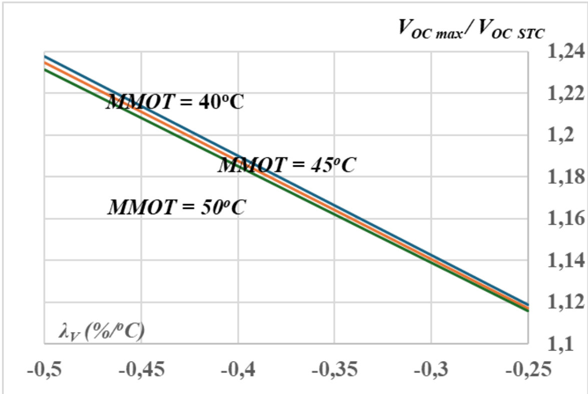

a. $V_{mp\ min} / V_{mp\ STC}$ *b.* $V_{OC\ max} / V_{OC\ STC}$

Fig. 4. Voltages variations for different thermal parameters of PV modules

To avoid the calculation of the actual parameters of the PV modules according to (1) – (6), for a fast dimensioning of a PV system located in Romania, we recommend verifying the next inequations, derived from (7) – (10) and based on the results from *fig. 3* and *4*:

- maximum number of series connected PV modules, Ns_{max}:

$$Ns_{max} \leq V_{max-Inv}/(1.25 \cdot V_{OC\ STC}) \tag{12}$$

- minimum number of series connected PV modules, Ns_{min}:

$$Ns_{min} \geq V_{min\ MPPT}/\left(0.7 \cdot V_{mp\ STC}\right) \tag{13}$$

- maximum number of parallel connected PV arrays, Np_{max}:

$$Np_{max} \leq I_{max\ MPPT}/\left(1.15 \cdot I_{mp\ STC}\right) \tag{14}$$

$$Np_{max} \leq I_{sc\ MPPT}/(1.15 \cdot I_{sc\ STC}) \tag{15}$$

Of course, relations (12) – (15) should be used only in the pre-dimensioning stage, when the designer is dealing with the choice of the PV system components, e.g. has the module and is looking for the inverter or vice versa, and are not intended to be a shortcut in the design process, i.e. to replace the computation of the PV module parameters in the “worst case scenarios” (1) – (6) followed by the fulfillment of (7) – (10).

REFERENCES

[1] https://anre.ro/despre/rapoarte/, accessed October 2024.

[2] Villalva MG, Gazoli JR, Filho ER. *Comprehensive approach to modeling and simulation of photovoltaic arrays*. IEEE Trans.Power Electron, 94(5): 1198-1208, 2009.

[3] Brano V L, Orioli A, Ciulla G, Gangi A D. *An improved five-parameter model for photovoltaic modules*. Solar Energy Materials and Solar Cells, 94(8): 1358-1370, 2010.

[4] Mahmoud Y, Xiao W, Zeineldin H H. *A Simple Approach to Modeling and Simulation of Photovoltaic Modules*. IEEE Transactions on Sustainable Energy; 3(1): 185-186, 2011.

[5] Chatterjee A, Keyhani A, Kapoor D. *Identification of Photovoltaic Source Models*. IEEE Transactions on Energy Conversion; 26(3): 883-889, 2011.

[6] Siddique H, Xu P, De Doncker R. *Parameter extraction algorithm for one-diode model of PV panels based on datasheet values*. International Conference on Clean Electrical Power (ICCEP). 2013.

[7] Haider I, Nader A, *Variations of PV module parameters with irradiance and temperature*, Energy Procedia, Volume 134, Pages 276-285, 2017.

[8] L. D. Jathar, S. Ganesan, U. Awasarmol, K. Nikam, K. Shahapurkar, M. E. M. Soudagar, H. Fayaz, A.S. El-Shafay, M.A. Kalam, S. Bouadila, S. Baddadi, V. Tirth, A. S. Nizami, S. S. Lam, M. Rehan, *Comprehensive review of environmental factors influencing the performance of photovoltaic panels: Concern over emissions at various phases throughout the lifecycle*, Environmental Pollution, Volume 326, 2023.

[9] R. Bhol, R. Dash, A. Pradhan and S. M. Ali, *Environmental effect assessment on performance of solar PV panel, International Conference on Circuits, Power and Computing Technologies*, Nagercoil, India, pp. 1-5, 2015.

[10] A. A. Teyabeen, A. Algareu and F. Mohamed, *Assessment of Solar Photovoltaic System Performance,* 14th International Renewable Energy Congress (IREC), Sousse, Tunisia, pp. 1-5, 2023.

[11] European Commission, Joint Research Center, Photovoltaic Geographical Information System (PVGIS), https://ec.europa.eu/jrc/en/pvgis.

Received: November 2024, Accepted: December 2024, Published: December 2024
Digital Object Identifier: https://doi.org/10.34302/CJEE/TJLG4115

COST-BENEFIT ANALYSIS OF TRANSITION TO ELECTRIC VEHICLES IN A LOGISTICS COMPANY

Mihaela **ȘTEȚ**
Technical University of Cluj-Napoca
mihaela.stet@ieec.utcluj.ro,

Keywords: logistics, electric vehicles, cost-benefit analysis, charging

Abstract: *This research investigates the economic feasibility of transitioning a logistics company's fleet to electric vehicles (EVs). The study evaluates the economic viability of this transition by comparing the total cost of ownership (TCO) of EVs to that of traditional internal combustion engine (ICE) vehicles. Key factors considered in the analysis include vehicle purchase costs, operational expenses, energy consumption and costs, maintenance expenses, and government incentives. The study aims to quantify the potential financial benefits and drawbacks associated with EV adoption and to assess the overall economic viability of such a transition. The findings of this CBA provide valuable insights for logistics companies seeking to make informed decisions about their fleet electrification strategies.*

1. INTRODUCTION

The transition to electric vehicles (EVs) is one of the most important transformations in the transportation sector globally. In recent years, this trend has extended beyond the passenger car segment, including the road freight transport sector. This process is being accelerated by a number of factors, including environmental concerns, diminishing fossil fuel reserves and their price volatility, evolving technologies, and governmental and international policies.

Vehicles with internal combustion engines are a major source of air pollutants affecting public health, especially in urban areas. Since emissions from road transport are a major cause of air pollution and climate change, along with industry and energy, replacing vehicles with internal combustion engines with vehicles powered by electricity can significantly contribute to reducing these emissions. At the present time the electrification of road transport is considered a key solution for reducing these emissions and achieving international climate goals.

The transition to electric vehicles reduces dependence on fossil fuels, contributing to price stability and energy security. Fluctuations in oil and natural gas prices make the operating costs of internal combustion engine (ICE) vehicles less predictable.

Electric motors provide more torque at low revolutions, which can improve vehicle performance, especially when starting and climbing.

Lower electricity costs compared to fossil fuels and lower maintenance costs can lead to significant savings in the long run.

Recent technological advances which have led to battery improvements, increased autonomy and the development of charging infrastructure make EVs increasingly attractive to users.

Many countries and regions around the globe have implemented policies, regulations and financial incentives to promote the adoption of EVs, such as subsidies, tax and duty reductions, including in the freight sector.

By electrifying their fleets, organizations not only demonstrate environmental leadership and dedication to sustainability, but also encourage wider adoption of EVs by other fleets and consumers, thus fostering significant societal change.

A significant barrier to widespread fleet electrification is the absence of sufficient electric vehicle options in the pick-up truck, medium-duty, and heavy-duty classes, thereby constraining fleet managers' ability to fulfill operational needs.

Concerns about the operational range and a lack of familiarity with the new technology are causing initial employee resistance to the electrification of the fleets. To address this initial employee resistance, awareness and education programs are required. For both fleet managers and employees, increasing their understanding of EV benefits can be achieved by emphasizing cost savings and environmental advantages via advertisements and workshops.

Electrifying vehicles is challenging due to charging times and range limitations. Furthermore, public disapproval of EVs as potentially wasteful government expenditures can deter their integration into fleets.

2. COST-BENEFIT ANALYSIS MODELS APPLICABLE IN THE TRANSPORT SECTOR

Cost-benefit analysis (CBA) is an essential tool in the decision-making process, especially when significant investments are involved. This allows for systematic assessment of all aspects of a project, from a financial, social and environmental point of view, with the aim of determining whether the anticipated benefits outweigh the associated costs (*fig. 1*). CBA helps to clearly define a project's objectives and determine whether they are economically feasible. A sound cost-benefit analysis provides an objective justification for investment decisions, both for those involved in the decision-making process and for external stakeholders.

CBA helps to identify projects that offer the best cost-benefit ratio, thus ensuring an optimal use of financial resources. This allows the comparison of different project alternatives, thus facilitating the choice of the best option. Through the detailed assessment of all relevant factors, CBA enables the identification of potential risks and mitigation measures, thus reducing the chances of project failure. Through its transparency, CBA contributes to a better understanding of the impact of projects on the environment, society and economy.

Cost-benefit analysis has multiple uses in the transport sector, from evaluating infrastructure projects, analyzing the operating costs of different modes of transport, comparing different propulsion technologies to assessing the impact of transport policies.

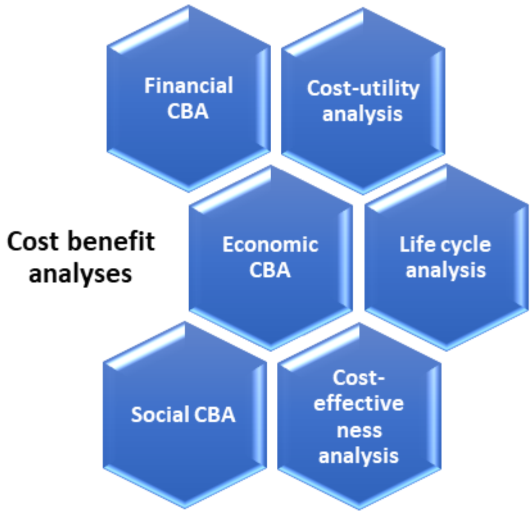

Figure 1. Types of analyses for the transportation sector

In their paper de Rus et al. [1] discussed the theoretical framework and practical rules for conducting CBA of transportation projects, focusing on economic evaluation methods and their implications for social welfare.

Eremina and Sohn [2] realized a CBA evaluating four major alternative routes based on selected cost and benefit factors. The cost considered factors are transportation time, gauge difference, custom procedures and cross-border factors, costs being expressed in terms of days and hours and benefits in monetary units. They take into consideration as benefit factors the volume of cargo, industrial production of adjacent regions, access to natural resources, market size and investment climate. A transformation coefficient is used to translate physical time into monetary value, based on empirical findings that a 10% increase in transportation time reduces bilateral trade volume by 5%.

Noel and McCormark [3] present a cost-benefit analysis comparing V2G-capable electric school buses to traditional diesel school buses, highlighting economic and environmental advantages. Although battery costs are often considered a barrier, sensitivity analysis shows that varying battery replacement costs have a relatively minor effect on the overall cost-benefit analysis. The analysis shows that the electric bus becomes cost-effective primarily due to the V2G revenues.

On the other hand, in their comparative cost-benefit analysis, Shirazi et al. [4] of alternatively fueled buses, compressed natural gas (CNG) and vehicle-to-grid (V2G) electric buses, concluded that diesel buses are the most cost-effective option, while CNG and eBuses have potential under specific conditions, such as infrastructure availability or future cost reductions. They considered the economic viability of eBuses to be affected by high upfront costs, infrastructure requirements, battery-related challenges, temperature impacts, V2G revenue limitations, and regulatory hurdles.

Park et al. [5] present a cost-benefit analysis of public service electric vehicles (EVs) with V2G capability, focusing on their operational savings and environmental impacts in sectors like school buses, waste collection trucks, and city buses. The analysis highlights that EVs are more cost-effective due to lower operational costs, environmental benefits, and additional revenue from V2G services.

Pagliara et al. [6] propose a methodology to estimate the benefits and costs of stakeholder engagement (SE) in the transport decision-making process, including CBA for efficient resource allocation and Multi-Criterion Analysis (MCA) to evaluate the social utility of public projects. The methodology involves a detailed breakdown of all potential costs associated with SE activities, both direct and indirect. They highlight the significant positive impact of SE on the project's success and the importance of incorporating SE into the decision-making process for transport projects.

CBA can be used both before (ex-ante) and after (ex-post) the implementation of a project to assess its feasibility and effectiveness. Ex ante analysis helps in planning and decision-making, while ex post analysis evaluates the actual outcomes and lessons learned.

Kelly et al. [7] studied the ex-ante and ex-post cost-benefit analyses of ten EU-funded transport projects across eight countries, revealing the deficiencies in ex-ante methodologies, while also highlighting the benefits and challenges of ex-post cost-benefit analysis.

Filippi et al. [8] in their ex-ante assessment focuses on estimating the environmental, social, and economic impacts, such as pollutant emissions, traffic congestion, and costs, to ensure that the measures will effectively reduce negative externalities and improve urban mobility sustainability.

In a study focused on the accuracy of ex-ante benefit-cost analyses (BCAs) in transportation realized by Odecka and Kjerkreitc [9], they concluded that ex-ante BCAs tend to underestimate benefits and overestimate costs and ex-post evaluations are essential for assessing whether projects deliver promised benefits and for identifying areas to improve ex-ante BCAs. They enhance the credibility of BCAs as a decision-making tool and ensure informed investment decisions.

Hajinasab et al. [10] studies various types of policy instruments aimed at changing the behavior of travelers categorized into three main types: economic, administrative, and informative.

In their paper de Bok et al. [11] analyze the potential transport impacts of a proposed distance-based heavy goods vehicle charge, using strategic transport models to assess various implementation scenarios and their effects on freight transport demand and logistics.

Financial cost-benefit analysis evaluates the profitability of a project from the perspective of a private economic agent, considering only direct financial costs and benefits. Initial investments, operation and maintenance costs, generated income, and residual value of assets are considered.

Economic cost-benefit analysis assesses the impact of a project on the entire economy, including both direct and indirect and external costs and benefits, considering effects on production, consumption, employment, tax revenues, as well as positive externalities (reduction of pollution, improvement road safety) and negative (noise, congestion). It is a method suitable for major infrastructure projects, such as building highways or high-speed railways.

Cost-effectiveness analysis compares different alternatives to achieve a predetermined objective, identifying the most cost-effective option, based on the costs associated with each alternative and the level of achievement of the objective. It focuses on minimizing transportation costs to achieve a certain level of benefit and is useful when the budget is limited. This is a model that can be used for projects with well-defined objectives, such as reducing congestion or improving road safety.

Whitmore et al. [12] treated the integration of shared autonomous vehicles into public transportation systems to enhance transit equity and cost-efficiency, particularly for transit-dependent populations.

Social cost-benefit analysis involves evaluating the impact of a project on social welfare, being suitable for projects with a significant impact on the quality of life, such as the development of public transport.

Cost-utility analysis evaluates costs against benefits measured in units of utility (e.g., life years gained, travel time reduced). It is frequently used in infrastructure projects that affect public health or quality of life.

Target costing analysis is a strategic cost management approach used to ensure that services meet customer expectations while maintaining profitability. It involves setting a target cost, which is the maximum allowable cost for a service, and then designing the service to meet this cost while delivering desired functionalities and customer value.

But CBA needs to evaluate the welfare impacts of a transport project by considering both the positive and negative effects on society. This includes environmental impacts, social inclusion, and economic development.

Life-cycle assessment (LCA), which assesses the environmental impact of a product or service throughout its life cycle, from raw material extraction to waste disposal, is based on data such as energy consumption, greenhouse gas emissions greenhouse, waste production, water use. Based on this, the carbon footprint, respectively the ecological footprint, can be highlighted. The model finds its applicability in the case of the evaluation of vehicle procurement projects or the development of intelligent transport systems.

Manzo and Bang Selling [13] demonstrated the importance of the integration of LCA into traditional transport cost-benefit analysis (CBA) to better evaluate the environmental impacts of transport infrastructure projects, to better assess long-term sustainability and provide more comprehensive information for decision-making

In the LCA realized by Rial and Pérez [14], climate change impacts are central to evaluating the environmental performance of heavy-duty propulsion technologies, as reducing greenhouse gas emissions is a key goal for sustainable transportation. The study highlights the importance of addressing emissions not only during the use phase but also in fuel production and vehicle manufacturing.

CBA has diverse applications within the transport sector, ranging from evaluating infrastructure projects and operating costs to comparing technologies and assessing the impact of transport policies. Different cost-benefit analysis methods are tailored to specific perspectives and objectives.

The accuracy and effectiveness of CBA can vary depending on the stage of analysis. Ex-ante analyses are prone to underestimating benefits and overestimating costs, highlighting the importance of ex-post evaluations for learning and improving future analyses.

The transport sector presents unique challenges and opportunities for CBA. Factors such as network effects, externalities (like pollution and congestion), and the long-term nature of infrastructure investments require careful consideration in CBA. For this reason, integrating other analytical tools with CBA enhances its comprehensiveness, like LCA to provide a more thorough evaluation of environmental impacts, leading to more sustainable decision-making. Multi-Criterion Analysis (MCA) can complement CBA by evaluating also the social utility of projects.

The selection of the most appropriate evaluation method is project-specific and depends on the goals of the analysis. A thorough and well-executed analysis is essential for making optimal investment decisions in the transport sector, contributing to sustainable and efficient development.

3. LIMITATIONS OF COST-BENEFIT ANALYSIS

Cost-benefit analysis has several important limitations. First of all, assessing benefits such as improved quality of life can be difficult and subjective. The future is unpredictable and estimates of costs and benefits may be affected by external factors that are difficult to anticipate or estimate. Many times, CBA models involve simplifications of reality.

Park et al. [5] highlight as limitations of CBA the sensitivity to assumptions such as diesel costs, electricity prices, battery lifespan, and maintenance costs. environmental cost estimation, uncertainty in V2G revenue, dependent on time-varying frequency regulation prices and the ability to optimize charging and discharging schedules, the upfront cost of EVs, battery replacement costs, the limited scope, external factors and simplified models, which may not capture real-world complexities.

Even though their paper only refers to the evaluation of transport infrastructure projects, Jones et al. [15] capture very precisely the weaknesses of the Cost-Benefit Analysis, which can be extended to other transport investments. They highlight inaccuracy in traffic forecasts, cost estimation errors, environmental impact assessment, regional and local impact, and sensitivity to assumptions. Underlining the significant impact of discount rates on CBA, affecting the Net Present Value (NPV) of a project, they highlight that higher discount rates reduce the present value of long-term benefits, favoring projects with immediate returns over those with long-term impacts and this can lead to the neglect of projects with substantial future benefits, such as environmental sustainability initiatives.

Multi-criteria analysis evaluates projects, as the name suggests, based on several criteria, both quantitative and qualitative, namely economic, social, environmental, political criteria, which can be difficult to quantify in monetary terms.

Annema et al. [16] discuss the perspectives of Dutch transport politicians on the use of CBA and multi-criteria decision-making (MCDM) as appraisal tools in transport policymaking. While CBA provides a clear efficiency criterion through monetary valuation, MCDM offers flexibility in incorporating qualitative criteria and stakeholder opinions. Both methods have their strengths and limitations, and a combination or new approach focusing on clear trade-offs and transparency might better support transport policy decision-making.

Used for evaluating projects under conflicting criteria, MCA is particularly useful when non-monetary factors need to be considered alongside economic impacts [1].

Fekpe et al. [17] describes the development of a multi-criteria systems-based benefits assessment framework for evaluating transport research projects, based on systems theory, which views benefits assessment as an open system composed of interacting and interdependent subsystems. This approach allows for the assessment of benefits across multiple dimensions, including economic, social, environmental, and user satisfaction.

Mann and Levinson [18] present an alternative approach to cost-benefit analysis for transport investments, focusing on access-based valuation through hedonic pricing models to better quantify project benefits compared to traditional travel time savings methods. This approach aims to provide a more accurate and comprehensive evaluation of transport projects by considering land use and economic impacts, avoiding the common issue of forecast inaccuracy associated with traditional travel-time savings methods.

Computable General Equilibrium Models (CGE) are recommended for mega-projects where some requirements for CBA are not satisfied. CGE models analyze the broader economic impacts, such as changes in gross value added or employment, and adapt these to produce monetary measures of welfare changes.

The choice of a suitable CBA model depends on the specifics of each project and the objectives pursued. A rigorous and comprehensive analysis can contribute to an optimal investment decision in the transport sector, ensuring a sustainable and efficient development of transport infrastructure and services.

CBA models often simplify complex realities, and this can lead to an incomplete picture and may not capture all relevant real-world dynamics.

The outcomes of cost-benefit analyses are heavily dependent on the initial assumptions made. Variables such as discount rates, fuel expenses, maintenance costs can substantially alter the results of a CBA, in real conditions, in a very dynamic business environment.

4. COST-BENEFIT ANALYSIS IN THE ELECTRIFICATION OF THE FLEET OF DELIVERY VEHICLES

A large amount of data is needed to assess the feasibility and profitability of switching to a fleet of electric delivery vehicles.

First, data on the current fleet of vehicles, the existing infrastructure, as well as data on electric vehicles and the infrastructure required for them are needed. In connection with these, financial and operational data are required, as well as environmental and social impact data. And finally, data on uncertainties and risks are needed.

Rodríguez-Molina et al. [19] based on their model for the cost-benefit analysis of privately owned Vehicle-to-Grid (V2G) relieved that V2G technology is more economically efficient in the long term compared to Internal Combustion Engine (ICE) vehicles, due to lower operational costs, including maintenance and fuel (electricity) costs. For professional drivers, V2G solutions become economically advantageous almost immediately, while for frequent drivers, V2G solutions become more cost-effective after the first year and for occasional drivers, after 3 to 4 years. They considered in their analysis the impact of battery degradation, energy trading, battery leasing vs. ownership and externalities, such as health impact costs, carbon emissions, and the social cost of carbon.

Christensen and Christensen [20] compare electric and diesel vehicles across several key cost components, including investment, operation, maintenance, environmental impact, noise, refueling/switching time, and marginal excess tax burden (METB). The methodology used in the analysis involves conducting a CBA to evaluate the socio-economic impacts of purchasing and operating an EV compared to a diesel vehicle. They considered as indirect benefits the improved air quality and reduced greenhouse gas emissions. The Social Discount Rate (SDR) is determined through a combination of empirical data and theoretical models. Empirically derived discount rates are based on market data and include Marginal Rate of Return on Private-Sector Investments (r), Social Marginal Rate of Time Preference (p) and

Government's Real Borrowing Rate (i). The theoretically derived discount rates are based on Optimal Growth Rate Model (Ramsey Model).

Lavee and Parsha [21] evaluate three levels of government support: basic, medium, and high, considering the costs and benefits associated with purchase subsidies, investment in public charging infrastructure, and taxation of private use of company cars. The analysis shows that only the basic level of government support passes the cost-benefit test, yielding a positive net benefit, while medium and high support levels result in net negative benefits, indicating that the costs exceed the benefits.

The methodology used in a study realized in 2018 [22] involved evaluating the costs and benefits of two different levels of plug-in electric vehicle (PEV) penetration in Arizona between 2030 and 2050. The study compared a "Moderate PEV" scenario, which aligns with the transportation electrification goals in Arizona Corporation Commissioner Andy Tobin's 2018 Draft Energy Modernization Plan, and a "High PEV" scenario, which includes more aggressive PEV penetration levels. Cost calculations include costs for electricity generation, transmission, incremental peak generation capacity, and infrastructure upgrades. They also calculated the NPV of total societal benefits, including cost savings to drivers, utility customer savings, public charger owner benefits, and the monetized value of reduced emissions.

In a similar study realized in Florida [23], PEV adoption in Florida offers substantial economic, environmental, and societal benefits. But achieving high penetration levels requires coordinated policy efforts and infrastructure investments. Managed charging strategies can maximize benefits for both drivers and utility customers.

In a TNO report, Tol et al. [24] provides a cost-benefit analysis of adopting zero-emission vehicles, ZEVs, for medium trucks (7.5-16 tons) and tractor-trailer trucks (>32 tons) across various EU+UK countries, focusing on road tolls, energy consumption, vehicle prices, and maintenance costs.

A wide range of scenarios can be considered for a cost-benefit analysis in electrification of the fleet for a logistics company.

First, the results may differ substantially depending on the type of vehicle and the type of electric drive. This includes hybrid electric vehicles (HEV), plug-in hybrid electric vehicles (PHEV), battery electric vehicles (BEV) and vehicles equipped with vehicle-to-grid technology (V2G).

By feeding energy back into the grid during peak demand and high electricity prices, V2G could generate revenue. This capability could significantly enhance their cost-benefit profile, counteracting charging costs and potentially yielding profits. At the same time, V2G-enabled charging strategies offer a pathway to higher NPV by generating additional cash flows from grid electricity sales.

In their paper Bagheri Tookanlou et al. [25] based on a cost-benefit analysis, propose a strategy reduces the cost of electric vehicles (EVs) by 18% and increases the revenues of EV charging stations (EVCSs) and electricity suppliers (ESs) by 21% and 23%, respectively, compared to the scenario where EVs do not use the strategy for vehicle-to-grid (V2G) and grid-to-vehicle (G2V) operations.

But it is very important, however, to incorporate battery degradation costs into the financial model, as these could offset long-term profitability. Therefore, it's necessary to analyze how the frequency of discharging power to the grid affects battery lifespan and the total number of batteries required throughout the truck's operational life.

In order to prepare a cost-benefit analysis it has to identify the types of costs associated with the introduction or replacement of the existent fleet with a fleet of electric vehicles (*fig. 2*). The costs could be classified as regards investment costs, maintenance and operational costs.

Investment costs referred to prices of vehicles and the additional related to purchase, costs of battery replacement and the costs related to charging infrastructure.

So, the total investment expenditure (I_{EV}) to support of the transition to electric vehicles is the sum of several distinct capital outlays: the purchase price of the vehicles ($P_{vehicle}$), additional taxes, registration fees, and initial insurance premiums ($F_{regulatory}$), the present value of future battery replacement costs ($PV_{battery\_replacement}$), and the costs associated with the acquisition and installation of charging infrastructure ($C_{charging\_infrastructure}$).

$$I_{EV} = P_{vehicle} + F_{regulatory} + PV_{battery\_replacement} + C_{charging\_infrastructure} \tag{1}$$

Purchase price of fleet ($P_{vehicle}$) represents the initial capital outlay for acquiring the electric vehicles. For a fleet of n vehicles, each with a price p_i, the total purchase price is:

$$P_{vehicle} = \sum_{i=1}^{n} p_i \tag{2}$$

The additional taxes, registration fees, and initial insurance premiums ($F_{regulatory}$) encompass all mandatory initial costs associated with registering and insuring the vehicles of the fleet for operation, including sales taxes, registration fees, and the first insurance premium.

$$F_{regulatory} = \sum_{i=1}^{n} \left(T_{tax,i} + F_{registration,i} + P_{insurance,i}^{initial} \right) \tag{3}$$

Present value of future battery replacement costs ($PV_{battery\_replacement}$) represent the future expense of replacing the vehicle batteries over their operational lifespan, discounted to its present value. This requires estimating the battery replacement cost ($C_{battery\_replace}$), the time until replacement ($t_{replace}$), and the discount rate (r), taking into considerations that batteries may need replacement at different times for different vehicles based on usage and degradation.

$$PV_{battery\_replacement} = \sum_{i=1}^{n} \frac{C_{battery\_replace,i}}{(1+r)^{t_{replace,i}}} \tag{4}$$

Costs associated with the purchase and installation of charging infrastructure ($C_{charging\_infrastructure}$) include all expenses related to acquiring and setting up the necessary charging infrastructure: the cost of the charging units ($C_{charger}$), installation costs ($C_{installation}$), any required electrical upgrades ($C_{electrical\_upgrade}$), and potential land or permitting costs ($C_{permitting}$).

$$C_{charging\_infrastructure} = \sum_{j=1}^{m} C_{charger,i} + \sum_{j=1}^{m} C_{installation,j} + C_{electrical\_upgrade} + C_{permitting} \tag{5}$$

The general repair and maintenance expenditure (M_{EV}) for a fleet of n electric trucks over a specific operational period (Δt) can be determined as the sum of costs associated with scheduled maintenance ($C_{scheduled}$), unscheduled repairs ($C_{unscheduled}$), tire replacements (C_{tires}), and other miscellaneous maintenance activities (C_{misc}).

$$M_{EV}(\Delta t) = \sum_{i=1}^{n} \sum_{\Delta t} (C_{scheduled,i} + C_{unscheduled,i} + C_{tires,i} + C_{misc,i}) \tag{6}$$

Scheduled maintenance costs ($C_{scheduled,i}$) are the costs associated with routine maintenance tasks performed at predetermined intervals (based on time or mileage) as recommended by the manufacturer. These tasks typically include inspections, lubrication of specific components (if any), brake system checks, cooling system maintenance for the battery and electronics, and software updates. The cost can be modeled as a function of the frequency of these services ($f_{scheduled,i}$) and the average cost per service event ($\bar{c}_{scheduled,i}$)

$$C_{scheduled,i} = f_{scheduled,i} \cdot \bar{c}_{scheduled,i} \tag{7}$$

Unscheduled repair costs ($C_{unscheduled,i}$) are the costs incurred due to unexpected breakdowns or failures of vehicle components requiring repair or replacement outside the regular maintenance schedule. These can include issues with the electric powertrain (motor, inverter, power electronics), battery system faults (excluding full replacement, which is typically treated as a separate investment cost), braking system malfunctions, suspension issues, and other electrical or mechanical failures. The occurrence of these repairs is often stochastic and can be modeled using failure rates ($\lambda_{component}$) for various components and their respective repair costs ($c_{repair,component}$). Over a period Δt, the expected cost can be complex to model precisely, but can be estimated based on historical data or reliability predictions

$$E[C_{unscheduled,i}] = \sum_{components} (\lambda_{component,i} \cdot \Delta t) \cdot c_{repair,component,i} \tag{8}$$

Tire replacement costs ($C_{tires,i}$) represent the costs of replacing tires due to wear and tear or damage. The frequency of replacement depends on factors such as mileage, load, driving conditions, and tire quality. The cost can be modeled based on the number of tire sets replaced ($n_{tires,i}$) during the period and the cost per set ($\bar{c}_{tires,i}$). The number of replacements can be estimated based on the average tire lifespan and the total mileage of the truck.

$$C_{tires,i} = n_{tires,i} \cdot \bar{c}_{tires,i} \tag{9}$$

Miscellaneous maintenance costs ($C_{misc,i}$) includes other periodic or occasional maintenance expenses not covered in the above categories, such as wiper blade replacements, fluid top-ups (e.g., coolant, brake fluid), light bulb replacements, and minor bodywork repairs. These costs are often relatively small but contribute to the overall maintenance expenditure, being tracked as a total sum over the period.

$$C_{misc,i} = \sum_{events} c_{misc\_event,i} \tag{10}$$

Regarding the maintenance electric vehicles generally have fewer moving parts than diesel trucks, resulting in less wear and tear and reduced maintenance requirements. While generally lower, maintenance of the electric motor, power electronics, and battery management system requires specialized knowledge and tools.

The operational expenditure (O_{EV}) of electric vehicles comprises distinct cost components incurred over a defined operational period (Δt): electricity consumption ($C_{electricity}$), insurance premiums and related taxes ($C_{insurance\_taxes}$), charging infrastructure use (Ccharging), drivers costs ($C_{salaries}$), and fleet management expenses ($C_{fleet\_management}$).

$$O_{EV}(\Delta t) = \sum\nolimits_{\Delta t}(C_{electricity} + C_{insurance_{taxes}} + C_{charging} + C_{salaries} + C_{fleet_{management}} \tag{11}$$

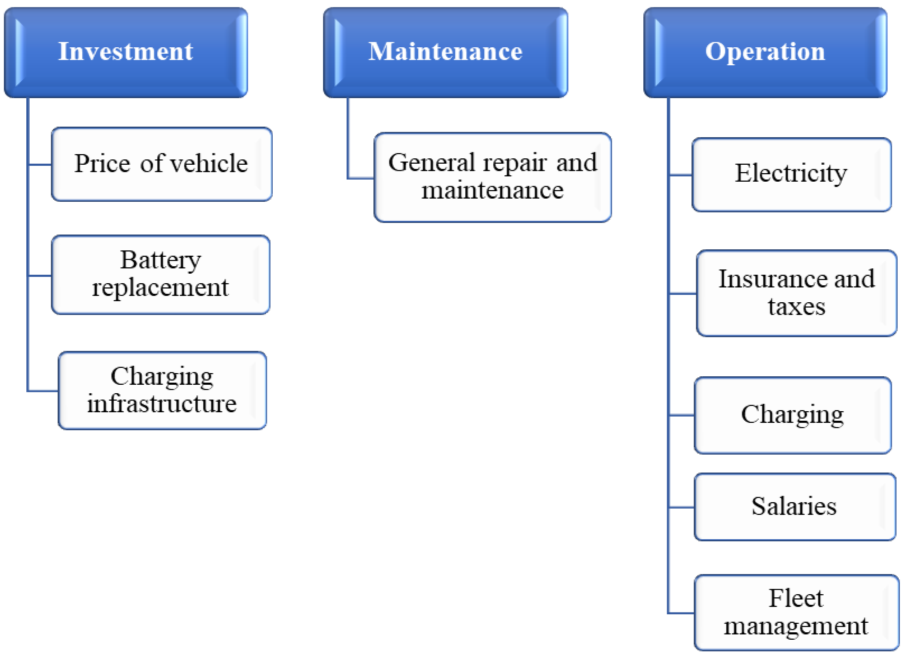

Figure 2. Cosst associated with the fleet electrification in a logistics company

Electricity consumption cost ($C_{electricity}$) is determined by the total energy consumed (E) by the vehicle during operation and the unit cost of electricity ($p_{electricity}$)

$$C_{electricity} = E \cdot p_{electricity} \tag{12}$$

The energy consumption (E) is a function of factors such as distance traveled (d), vehicle energy efficiency ($\eta_{vehicle}$ in kWh/km), and auxiliary power demands.

Insurance and related taxes ($C_{insurance\_taxes}$) encompasses the periodic insurance premiums ($P_{insurance}$) and any applicable taxes or fees directly associated with vehicle ownership and operation ($T_{vehicle}$). These costs are typically assessed over a specific time interval (e.g., annually) and must be prorated for the operational period Δt.

$$C_{insurance\_taxes} = P_{insurance} + T_{vehicle} \tag{13}$$

Charging infrastructure utilization cost ($C_{charging}$) is associated with the energy sourced for recharging the vehicle. For private charging, it is typically included within $C_{electricity}$. For public charging infrastructure, it includes the energy consumed during charging (E_{charge}), the unit cost of electricity at the charging point ($p_{charging}$), and any additional fees associated with the charging service (e.g., per-session fees, subscription costs, $F_{charging}$):

$$C_{charging} = E_{charge} \cdot p_{charging} + F_{charging} \tag{14}$$

Charging strategies and infrastructure are critical factors influencing the economics of EV fleets. If it is necessary to charge the vehicle during working hours, reducing the duration of vehicle travel corresponding to the periods for charging results in an increase in payroll expenses in relation to the distance traveled. The need for multiple charging stops in long-haul e-truck delivery routes diminishes productivity and drives up driver costs.

Opportunity charging can help integrate renewable energy into the grid by charging during periods of excess solar or wind energy availability. By charging trucks during idle periods between trips, opportunity charging avoids creating high peaks in electricity demand. The avoidance of high electricity demand peaks, achieved through charging trucks during inter-trip idle periods, serves to mitigate network costs. Thus, operators can optimize costs and maintain uninterrupted service.

Low-capacity charging offers the flexibility to charge trucks at lower power levels (e.g., 22 kW), which can translate to better cost efficiency than relying solely on faster, high-capacity charging.

Smaller fleets can more easily manage charging to align with their depot's general electricity consumption. However, for larger fleets, charging needs become the primary concern, overshadowing the impact of other depot consumption on overall costs. They need load management solutions to optimize electricity consumption by avoiding peak demand and aligning with lower electricity prices.

Strategically placing depots in areas with well-developed power infrastructure is another way to mitigate network connection costs and fees.

Human resource cost ($C_{salaries}$) represents the wages and benefits paid to drivers, the personnel directly involved in the operation of the vehicle. It is a function of the labor hours (h) dedicated to vehicle operation and the applicable wage rate (w).

$$C_{salaries} = h \times w \tag{15}$$

For commercial operations, this may also needs to include considerations for charging time that impacts driver availability and efficiency.

Fleet management expenses ($C_{fleet\_management}$) include costs associated with the overall management and administration of a fleet of electric vehicles, encompassing software subscriptions for tracking and optimization ($C_{software}$), maintenance of charging infrastructure ($C_{infrastructure\_maintenance}$), personnel costs for fleet management ($C_{management\_personnel}$), and other administrative overheads ($O_{administrative}$).

$$C_{fleet\_management} = C_{software} + C_{infrastructure\_maintenance} + C_{management\_personnel} + O_{administrative} \tag{16}$$

In what it concerns the benefits, they are mainly generated by the fuel cost savings, maintenance cost reduction and avoided emission costs comparing with ICE vehicles. Comparing to diesel trucks, they generate lower maintenance costs per kilometer, due to a reduced frequency of repairs and significantly lower costs with consumables. Electric trucks will have zero for pollutants like NOx, particulate matter, CO and greenhouse gas emissions.

These savings can make EVs more economically efficient in the long term compared to internal combustion engine vehicles.

In this study there had been analyzed the comparative cost-benefit of integrating different truck technologies—ICE, HEV, PHEV, and BEV—into the fleet of a logistics company. The analysis considers the acquisition of 200 trucks over an 8-year operational lifespan, employing a discount rate of 7%. The simulation of various scenarios was conducted using MATLAB.

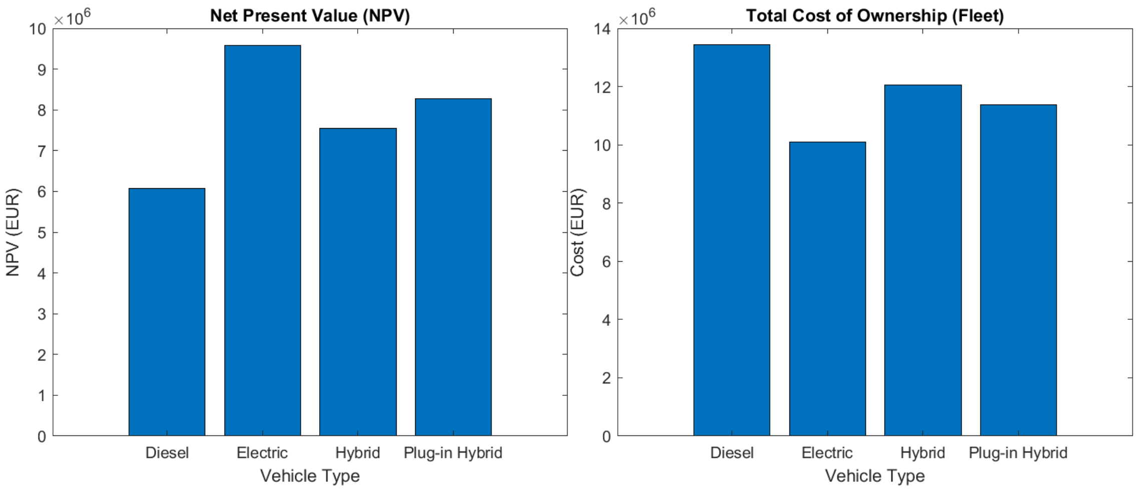

Figure 3. NPV and TCO for different types of freight vehicles

Key findings from the financial analysis, encompassing NPV, TCO and Cost-Benefit Ratio (CBR), reveal as the most economically advantageous being BEV (*fig. 3*, table 1). The input data is specific to the Romanian freight vehicle market and electricity prices in Romania.

Table 1. Financial results of the simulation

Type of vehicle	Total Cost of Ownership (TCO)	Net Present Value (NPV)	Cost-Benefit Ratio (CBR)
ICE	13,428,385.62 EUR	6,069,731.95 EUR	0,69
BEV	10,107,219.62 EUR	9,585,879.13 EUR	0,51
HEV	12,051,173.93 EUR	7,544,434.23 EUR	0,62
PHEV	11,362,568.08 EUR	8,281,785.38 EUR	0,58

The study also summarizes the impact of sensitivity analyses conducted on electricity prices and various charging scenarios for BEV and PHEV trucks, highlighting the factors that significantly influence their profitability.

In the case of the sensitivity analysis of NPV depending on the price of electricity, its increase influences BEVs the most, which was expected, given that electricity is the only source of energy for them (*fig. 4*).

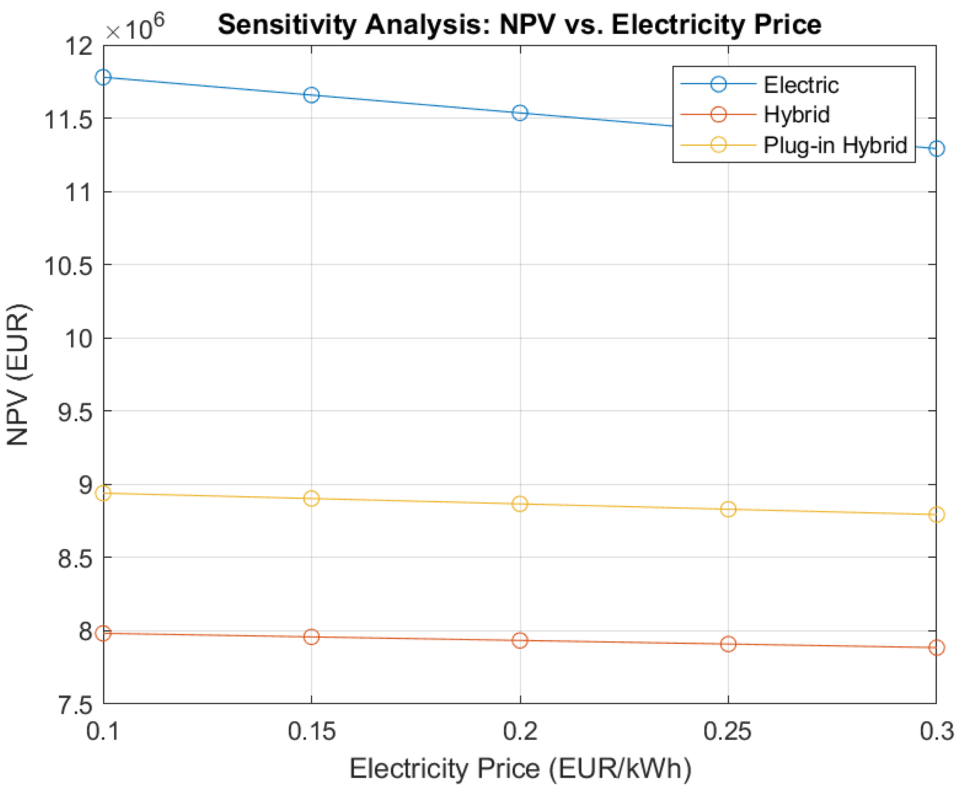

Figure 4. Sensitivity analysis NPV vs. electricity price

The sensitivity analysis of NPV considering annual revenue reveals an increasing with about 40% with an increase of only 20% in transport revenues (*fig. 5*).

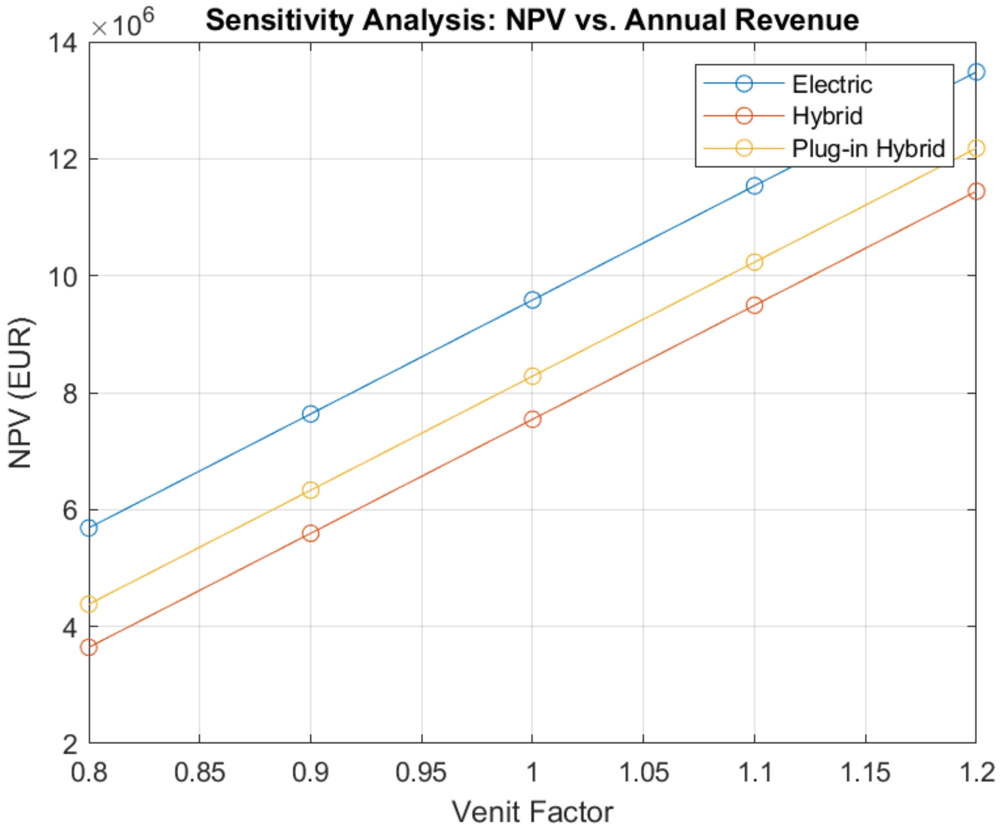

Figure 5. Sensitivity analysis NPV vs. annual revenue

Taking into account the economic context, it is also important to conduct a sensitivity analysis of the discount rate to see how it influences the level of discounted net income. This reveals for all types of vehicles a halving of the NPV at an increase in the discount rate from 0.05 to 0.15 (table 2).

Table 2. Sensitivity analysis NPV vs. discount rate

Discount Rate	Diesel NPV (EUR)	Electric NPV (EUR)	Hybrid NPV (EUR)	Plug-in Hybrid NPV (EUR)
0.05	6,973,247.93	10,947,176.53	8,636,684.66	9,468,403.02
0.07	6,069,731.95	9,585,879.13	7,544,434.23	8,281,785.38
0.1	4,900,884.85	7,824,816.17	6,131,427.96	6,746,699.52
0.12	4,226,277.12	6,808,407.19	5,315,902.18	5,860,714.70
0.15	3,344,059.91	5,479,199.93	4,249,399.59	4,702,069.43

Several charging scenarios were considered: fast charging at a public charging station, slow and fast charging at the depot, and charging using electricity supplied by photovoltaic panels during the day. The optimal option is the latter, followed by slow overnight charging at the depot.

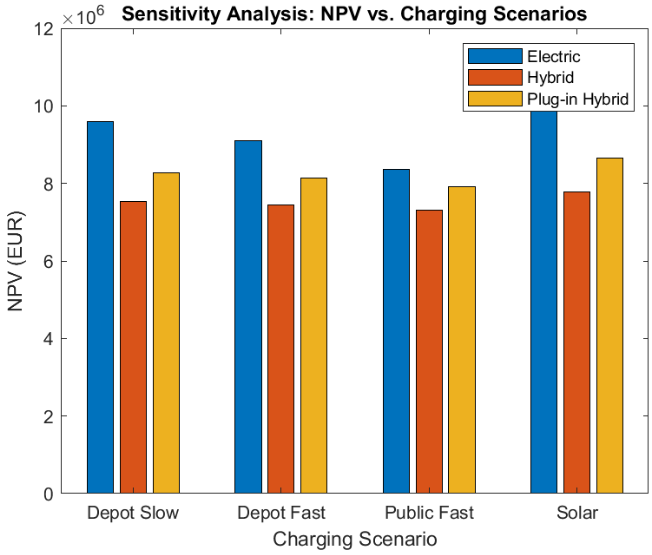

Figure 6. Sensitivity analysis NPV vs. charging scenarios

The consideration of various charging scenarios reveals that strategically optimized charging practices can significantly influence the economic benefits of electric vehicle fleets. Utilizing on-site photovoltaic power during the day and implementing slow overnight charging at the depot appear to be economically advantageous strategies. Furthermore, concepts like opportunity charging and load management for large fleets are crucial for minimizing electricity costs and network connection fees.

5. CONCLUSIONS

The process of preparing a cost-benefit analysis for fleet electrification requires a systematic identification and classification of associated costs. These costs can be broadly categorized into investment costs (vehicle purchase, regulatory fees, battery replacement, charging infrastructure) and maintenance and operational costs (general repair, scheduled maintenance, unscheduled repairs, tires, electricity consumption, insurance, charging infrastructure utilization, driver salaries, fleet management). For a thorough economic evaluation, a detailed comprehension of these individual cost elements and the variables that affect them is indispensable.

Cost-benefit analyses for fleet electrification need to consider various factors. These include the type of electric vehicle (HEV, PHEV, BEV, V2G), the specific costs associated with investment, maintenance, and operation (including charging infrastructure and battery replacement), and the potential for additional revenue generation through V2G. The V2G technology offers an opportunity to enhance the cost-benefit profile of electric vehicle fleets. By enabling vehicles to feed energy back into the grid during periods of high demand and elevated electricity prices, V2G can generate revenue streams that offset charging costs and potentially yield profits. This capability could contribute to higher NPV) by creating additional cash flows from grid electricity sales. This study did not incorporate this technology into the simulation model because it is not yet common in Romanian companies of this type.

The need for en-route charging can increase labor costs and reduce productivity, especially for long-haul deliveries. However, opportunity charging during idle periods can offer benefits by integrating renewable energy, mitigating peak demand, and reducing costs. Also, low-capacity charging can be more cost-effective than relying solely on high-capacity fast charging. Smaller fleets can more easily align charging with existing depot electricity consumption, while larger fleets require sophisticated load management solutions to optimize electricity use and avoid peak demand charges. Strategic depot placement can also help reduce network connection costs.

The sensitivity analyses conducted on electricity prices, annual revenue, and the discount rate demonstrate the significant impact of these economic parameters on the NPV of an electric vehicle fleet adoption. Notably, BEVs are most sensitive to electricity price fluctuations, while NPV across all vehicle types is inversely related to the discount rate. Furthermore, a positive correlation between annual revenue and NPV highlights the importance of operational efficiency and revenue generation in the financial viability of fleet electrification.

REFERENCES

[1] G. de Rus, M. Pilar Socorro, J. Valido, J. Campos, *Cost-benefit analysis of transport projects: Theoretical framework and practical rules*, Transport Policy 123 (2022) 25–39, https://doi.org/10.1016/j.tranpol.2022.04.008

[2] A. Eremina, and C.-H. Sohn, *A cost-benefit analysis of routes between the Trans-Korean and Trans-Siberian railways*, Journal of International Logistics and Trade, Volume: 8, Number: 2, December 2010, Pages: 33-62

[3] L. Noel, and R. McCormack, *A cost benefit analysis of a V2G-capable electric school bus compared to a traditional diesel school bus*, Applied Energy 126 (2014) 246–255, http://dx.doi.org/10.1016/j.apenergy.2014.04.009

[4] Y. Shirazi, E. Carr, L. Knapp, *A cost-benefit analysis of alternatively fueled buses with special considerations for V2G technology*, Energy Policy 87 (2015) 591–603, http://dx.doi.org/10.1016/j.enpol.2015.09.038

[5] D. Park, S. Yoon, E. Hwang, *Cost Benefit Analysis of Public Service Electric Vehicles with Vehicle-to-grid (V2G) Capability*, 2016 IEEE Transportation Electrification Conference and Expo, Asia-Pacific (ITEC) June 1 -4, 2016, Busan, Korea

[6] F. Pagliara, W. El-Ansari, I. Henke, (2023), *A methodology to estimate the benefits and costs of stakeholder engagement in a transport decision-making process*, Smart and Sustainable Built Environment Emerald Publishing Limited 2046-6099, DOI 10.1108/SASBE-03-2023-0049

[7] C. Kelly, J. Laird, S. Costantini, P. Richards, J. Carbajo, J. Nellthorp, *Ex post appraisal: What lessons can be learnt from EU cohesion funded transport projects?* Transport Policy, Volume 37, 2015, Pages 83-91, ISSN 0967-070X, https://doi.org/10.1016/j.tranpol.2014.09.011.

[8] F. Filippi, A. Nuzzolo, A. Comi, P. Delle Site, *Ex-ante assessment of urban freight transport policies*, Procedia Social and Behavioral Sciences 2 (2010) 6332–6342, doi:10.1016/j.sbspro.2010.04.042

[9] J. Odecka, and A. Kjerkreitc, *The accuracy of benefit-cost analyses (BCAs) in transportation: An ex-post evaluation of road projects*, Transportation Research Part A 120 (2019) 277–294, https://doi.org/10.1016/j.tra.2018.12.023

[10] B. Hajinasab, P. Davidsson, J.A. Persson, *A survey on the use of computational models for ex ante analysis of urban transport policy instruments*, Procedia Computer Science 32 (2014) 348 – 355, doi: 10.1016/j.procs.2014.05.434

[11] M. de Bok, G. de Jong, B. Wesseling, H. Meurs, P. van Bekkum, P. Mijjer, D. Bakker, T. Veger, *An ex-ante analysis of transport impacts of a distance-based heavy goods vehicle charge in the Netherlands*, Research in Transportation Economics 95 (2022) 10109, https://doi.org/10.1016/j.retrec.2021.101091

[12] A. Whitmore, C. Samaras, C.T. Hendrickson, H.S. Matthews, G. Wong-Parodi, *Integrating public transportation and shared autonomous mobility for equitable transit coverage: A cost-efficiency analysis*, Transportation Research Interdisciplinary Perspectives 14 (2022) 100571, https://doi.org/10.1016/j.trip.2022.100571

[13] S. Manzo, and K. Bang Salling, *Integrating life-cycle assessment into transport cost-benefit analysis*, Transportation Research Procedia 14 (2016) 273 – 282, doi: 10.1016/j.trpro.2016.05.064

[14] M. Rial and J. Pérez, *Environmental performance of four different heavy-duty propulsion technologies using Life Cycle Assessment*, Transportation Research Interdisciplinary Perspectives 11 (2021) 100428, https://doi.org/10.1016/j.trip.2021.100428

[15] H. Jones, F. Moura, T. Domingos, *Transport infrastructure project evaluation using cost-benefit analysis*, Procedia - Social and Behavioral Sciences 111 (2014) 400 – 409, doi: 10.1016/j.sbspro.2014.01.073

[16] J.A. Annema, N. Mouter, and J. Razaei, *Cost-benefit analysis (CBA), or multi-criteria decision-making (MCDM) or both: politicians' perspective in transport policy appraisal*, Transportation Research Procedia 10 (2015) 788 – 797, doi: 10.1016/j.trpro.2015.09.032

[17] E.S. Fekpe, M. Amuzu, W. Ackaah, F. Afukaar, J. Acquah, A. Addai-Yeboah, *Multi-criteria systems-based benefits assessment framework for transport research projects*, Transportation Research Interdisciplinary Perspectives 8 (2020) 100262, https://doi.org/10.1016/j.trip.2020.100262

[18] I. Mann, and D.M. Levinson, *Access-based cost-benefit analysis*, Journal of Transport Geography 119 (2024) 103952, https://doi.org/10.1016/j.jtrangeo.2024.103952

[19] J. Rodríguez-Molina, P. Pedro Castillejo, V. Beltran, and M. Martínez-Núñez, *A Model for Cost–Benefit Analysis of Privately Owned Vehicle-to-Grid Solutions*, Energies 2020, 13, 5814; doi:10.3390/en13215814, www.mdpi.com/journal/energies

[20] A.S. Christensen, and E.E. Christensen, *A Social Cost-Benefit Analysis of an Electric Vehicle*, Aarhus School of Business, August 2011, MSc. In International Economic Consulting, Academic Supervisor Jan Børsen Bentzen

[21] D. Lavee, and A. Parsha, *Cost-benefit analyses of policy tools to encourage the use of Plug-in electric vehicles*, Transportation Research Interdisciplinary Perspectives 11 (2021) 100404, https://doi.org/10.1016/j.trip.2021.100404

[22] M.J. Bradley & Associates, LLC (MJB&A), *Electric Vehicle Cost-Benefit Analysis, Plug-in Electric Vehicle Cost-Benefit Analysis: Arizona*, December 2018

[23] M.J. Bradley & Associates, LLC (MJB&A), *Electric Vehicle Cost-Benefit Analysis, Plug-in Electric Vehicle Cost-Benefit Analysis: Florida*, January 2019

[24] D. Tol, T. Frateur, M. Verbeek, I. Riemersma, H. Mulder, TNO 2022 R11862, *Techno-economic uptake potential of zero-emission trucks in Europe*, 2022, www.tno.nl

[25] M. Bagheri Tookanlou, M. Marzband, A. Al Sumaiti, A. Mazza, *Cost-benefit analysis for multiple agents considering an electric vehicle charging/discharging strategy and grid integration*, 978-1-7281-5200-4/20, 2020 IEEE

INSTRUCTIONS FOR AUTHORS

Name **SURNAME**[1], Name **SURNAME**[2]**, ...**
[1] *Affiliation of 1st author,* [2] *Affiliation of 2nd author, ...*
Email of 1st author, Email of 2nd author, ...(it is compulsory only for the first author)

Keywords: List 3-4 keywords *(aligned to the left, 10 pt. bold, separated by commas; please choose keywords from [IEEE Approved Indexing Keyword List])*

Abstract: *Abstract of max. 200 words, justify, 10 pt. italic.*

1. INTRODUCTION

The paper must be written in English. It shall contain at least the following chapters: introduction, research course (mathematical algorithm); method used; results and conclusions, references.

1.1. Fonts

Use DIN A4 Format (297 x 210 mm) MSWord format. Margins: top, bottom, left and right 2.5 mm each. The text should be written on one side of the page only. Use Times New Roman fonts, line spacing 1.3. The font formats are: paper title: 14 pt, bold, italic, capital letters, author's name(s): 12 pt, regular for name and 12 pt., bold, for surname; Affiliation: 11 pt., italic; key words: 10 pt., bold; Abstract: 10 pt., italic, word Abstract in 10 pt., bold; chapter titles (do not use automatic numbering): 12 pt., bold, capital letters; subtitles: 12 pt., bold, lower case letters; subsubtitles: 12 pt., italic, lower case letters; body text: 12 pt., regular; tables and figures caption: 11 pt.; italic; references: author 11 pt.; regular, title 11 pt. italic, year, pages, ... in regular.

1.1.1. Number of pages

The number of pages is not restricted.

2. FIGURES AND TABLES

Figures have to be made in high quality, which is suitable for reproduction and printing. Don't include photos or color prints if there are not clearly intelligible in gray scale option. Place figures and tables at the top or bottom of a page wherever possible, as close as possible to the first reference to them in the paper. In text, use either *fig. 1* or *figure 1* when necessarily.

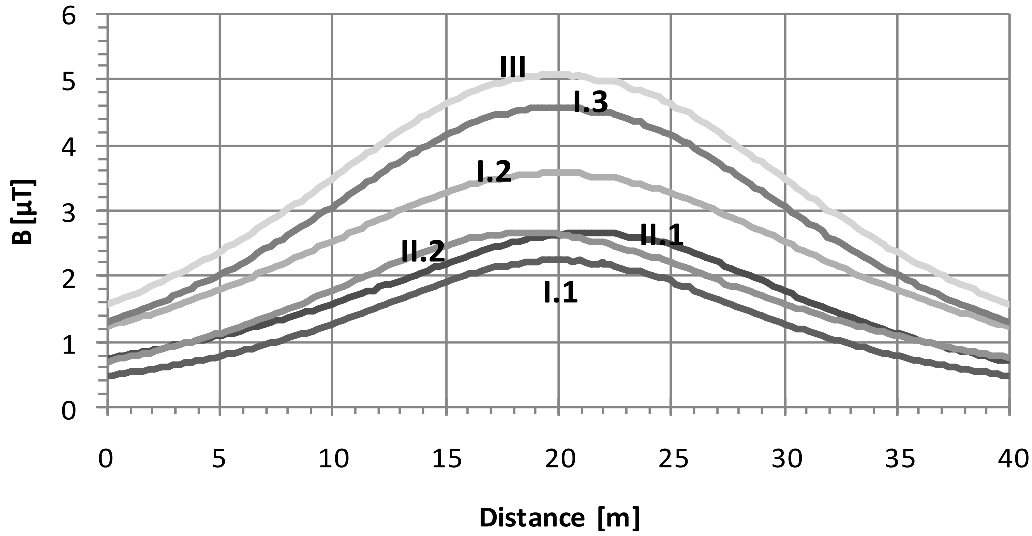

Fig. 1. Magnetic flux density at 1 m above the ground

Table 1. Transposing principle

	Circuit											
	1	*2*	*1*	*2*	*1*	*2*	*1*	*2*	*1*	*2*	***1***	***2***
1/3	*R*	*T*	***R***	***R***	*R*	*S*	*R*	*T*	*R*	*S*	***R***	***R***
line	***S***	***S***	*S*	*T*	*S*	*R*	*S*	*R*	*S*	*T*	***S***	***S***
length	*T*	*R*	*T*	*S*	***T***	***T***	*T*	*S*	*T*	*R*	***T***	***T***
1/3	*T*	*S*	***T***	***T***	*T*	*R*	*T*	*S*	*T*	*R*	***T***	***T***
line	***R***	***R***	*R*	*S*	*R*	*T*	*R*	*T*	*R*	*S*	***R***	***R***
length	*S*	*T*	*S*	*R*	***S***	***S***	*S*	*R*	*S*	*T*	***S***	***S***
1/3	*S*	*R*	***S***	***S***	*S*	*T*	*S*	*R*	*S*	*T*	***S***	***S***
line	***T***	***T***	*T*	*S*	*T*	*S*	*T*	*S*	*T*	*R*	***T***	***T***
length	*R*	*S*	*R*	*T*	***R***	***R***	*R*	*T*	*R*	*S*	***R***	***R***
Name	***I.1***		***I.2***		***I.3***		***II.1***		***II.2***		***III***	

3. EQUATIONS

Equations are centered on page and are numbered in round parentheses, flush to right margin.

$$a = b + c \tag{1}$$

Between equations, not interfered by text, there is only one empty line:

$$a = b + c \tag{2}$$

$$a = b + c \tag{3}$$

In text respect the following rules: all variables are italic, constants are regular; the references are cited in the text between right parentheses [1], the list of references has to be arranged in order of citation.

REFERENCES

[1] International Commission on Non-ionizing Radiation Protection, *Guidelines for limiting exposure to time-varying electric, magnetic and electromagnetic fields (Up to 300 GHz)*, Health Physics, vol. 74, no. 1, pp. 494-522, 1998.

[2] A. Marincu, M. Greconici, *The electromagnetic field around a high voltage 110 KV electrical overhead lines and the influence on the biological systems*, Proceedings of the 5th International Power Systems Conference, pp. 357-362, Timisoara, Romania, 2003.

[3] J. He, R. Zeng, B. Zhang, Methodology and Technology for Power System Grounding, Wiley-IEEE Press, Singapore, 2012.